DESIGN, FABRICATION, AND CHARACTERIZATION OF MICROELECTRODES FOR BRAIN-MACHINE INTERFACES

By

ERIN PATRICK

A DISSERTATION PRESENTED TO THE GRADUATE SCHOOL
OF THE UNIVERSITY OF FLORIDA IN PARTIAL FULFILLMENT
OF THE REQUIREMENTS FOR THE DEGREE OF
DOCTOR OF PHILOSOPHY

UNIVERSITY OF FLORIDA

2010

ACKNOWLEDGMENTS

This work was funded by a grant form the National Institute of Health, NS053561.

I would like to thank my chair advisor, Dr. Toshi Nishida, for his guidance and supportive advice throughout my undergraduate and graduate degrees at the University of Florida. I would also like to acknowledge my co-chair advisor, Dr. Mark Orazem, for the use of his lab equipment and thank him for his guidance and continued support throughout this project. My other committee members, Dr. Justin Sanchez, Dr. John Harris, and Dr. Jose Principe deserve thanks for their advice and technical assistance on this project.

I would like to acknowledge the Neuroprosthetics Research Group, headed by Dr. Justin Sanchez, at the University of Florida for the animal care and *in vivo* experimentation. Babak Mahmoudi and Jack DiGiovanna deserve thanks and credit for performing the implantation surgeries. I am also thankful for the discussions and sample microelectrodes from Dr. Vincent Vivier. Other technical assistance was provided at the University of Florida by Dr. Andrew Rinzler for the use of parylene-C vapor deposition tools and Al Ogden with packaging and numerous fabrication processing suggestions. I would also like to acknowledge the staff at the Major Analytical Instrumentation Center (MAIC) at the University of Florida for the scanning-electron micrograph (SEM) images and energy dispersive x-ray (EDS) analysis of the electrode samples. The Electrical and Computer Engineering staff also deserves thanks for their help and guidance.

My colleagues, Viswanath Sankar and William Rowe, deserve thanks for their assistance throughout this project. I would also like to thank all the students of the Interdisciplinary Microsystems Group and Professor Orazem's group for their technical advice during numerous discussions. Jie Xu and Sheng-fen Yen from the Computational Neuroengineering Group at the University of Florida deserve acknowledgement for the design of the cmos amplifier used in this work.

I thank my family for their love and encouragement. My mom, Jan Patrick, and sisters, Keri and Anna Patrick, have given me great support. Above all, I thank my loving husband for his continued support and encouragement and my newest inspiration, baby Bryson.

TABLE OF CONTENTS

LIST OF TABLES

LIST OF FIGURES

Abstract of Dissertation Presented to the Graduate School
of the University of Florida in Partial Fulfillment of the
Requirements for the Degree of Doctor of Philosophy

DESIGN, FABRICATION, AND CHARACTERIZATION OF MICROELECTRODES FOR BRAIN-MACHINE INTERFACES

By

Erin Patrick

August 2010

Chair: Toshikazu Nishida
Cochair: Mark Orazem
Major: Electrical and Computer Engineering

The long-term goal in the design of brain-machine interfaces (BMIs) is to restore communication and control of prosthetic devices to individuals with loss of motor function due to spinal cord injuries, amyotrophic lateral sclerosis, or muscular dystrophy, for example. One of the great challenges in this effort is to develop implantable systems that are capable of processing the activity of large ensembles of cortical neurons. This work presents the design, fabrication, characterization, and *in vivo* testing of a neural recording platform for a pre-clinical application. The recording platform is a flexible, polyimide-based microelectrode array that can be hybrid-packaged with custom electronics in a fully-implantable form factor. Results from the microelectrode array integrated with an amplifier integrated circuit include data from *in vivo* neural recordings showing consistent single-unit discrimination over 42 days. Moreover, results from the electrochemical assessment of the corrosion properties of the tungsten microwire electrodes used on the microelectrode array admonish the use of tungsten in long-term implants.

CHAPTER 1
INTRODUCTION

1.1 Overview and Motivation

Neurological disorders result in irreversible damage to the peripheral or central nervous system and greatly reduce the quality of life of the afflicted individual. While great strides have been made in understanding neurological disorders and mitigating deleterious effects, cures for these disorders via effective regeneration of a severely impaired central nervous system is not a near-term solution. Amytrophic Lateral Sclerosis (ALS) and spinal cord injuries, which make-up a large portion of all paralysis cases, contribute together 15,000 new cases each year [2]. Epilepsy is estimated to cost $15.5 billion annually and approximately 200,000 new cases are diagnosed each year [3]. These examples are just a few of many neurological disorders affecting people today. Fortunately, engineering can provide hope to some by providing alternate methods for regaining lost function due to neurological disorders.

Neural prosthetic technologies, or neuroprostheses, are designed to replace, repair, or augment function for individuals with vision, hearing, or motor impairments. Neuroprostheses interface with the nervous system and either transmit or receive neural information in order to perform a task. Examples of sensory prosthetics are retinal and cochlear implants for the blind and deaf. These prosthetics code images or sound taken from wearable cameras and microphones into electrical impulses which are used to stimulate retinal or auditory nerves, respectively. The cochlear implant is best known and is commercially available [4, 5]. Another neuroprosthesis uses functional electrical stimulation (FES) to therapeutically modulate neural activity in the brain of people with Parkinson's disease, epilepsy, and depression [6–8]. Electrical signals are sent via the prosthetic into a targeted portion of the patient's brain mitigating the debilitating effects of their condition.

Motor neuroprostheses aim to provide control of external devices such as prosthetic limbs, computer programs, and motorized wheel chairs with signals from the central or peripheral nervous systems. An example of a peripheral nervous system motor prosthetic is a prosthetic robotic arm that electrically interfaces with a peripheral nerve in an amputee's shoulder [9]. Signals from peripheral nerves in the shoulder of the amputated arm provide the commands for the robotic arm. Alternatively, motor neuroprostheses that interface with the central nervous system are commonly called brain-machine interfaces, (BMIs) or brain-computer interfaces (BCIs). They ideally provide the means for thought control of external devices by recording central nervous system (CNS) neural activity and decoding motor intention [10]. These systems may potentially be used as therapy for individuals with paralysis of the extremities caused by injury or neurodegenerative diseases such as amyotrophic lateral sclerosis (ALS), muscular dystrophy, or other diseases that cause a "locked-in" condition.

1.1.1 Brain-Machine Interfaces

BMI systems comprise of four processes: recording neural activity, interpreting the activity as an intended action, controlling a device that performs the intended action, and providing feedback to the subject [4]. An example of possible BMI function for a quadriplegic is directional control of a motorized wheel chair via brain signals. The type of neural activity used to provide such commands varies with application and researcher. However, preclinical studies primarily use neural activity in the motor cortex [11, 12]. Therefore, in the proposed scenario, directional control of a mechanical wheel chair could be administered by the neural activity that occurs when thinking about moving an arm.

Progress on BMI systems has been made in preclinical and clinical studies. Chapin et al. showed real-time control of a robotic arm via cortical signals elicited by a fore-limb lever pressing action done by a rat [11]. Others have shown effective 1D and 3D control of robotic arms [12] and cursors on screens [13, 14] in BMIs in primates. Carmena et

al. presented first time results of real-time control of two movements (reaching and grasping) in a visual feedback closed loop BMI system in a primate [15]. Velliste et al's experiments show the potential of BMIs for multidimensional control of a robotic arm in an interactive closed loop system, where monkeys were able to feed themselves [16]. Recent clinical trials using BMIs allowed a tetrapalegic patient to control a cursor on a computer screen, play a video game, adjust the volume and channel of a television, and control a simple robotic hand [17]. Electrodes were implanted into the arm area of the patient's motor cortex. By imagining hand movements, the patient was able to provide signals to control the BMI devices.

1.1.2 Neural Recording Mechanisms for BMIs

Neural activity for BMIs can be measured with electroencephalographic (EEG) electrodes, electrocorticographic (ECoG) electrodes, or intracortical microelectrode arrays. Figure 1-1 shows a representation of each recording electrode. Each electrode measures neuronal electrical activity with different spatial and temporal resolution. EEG electrodes reside on the scalp, measure neural activity across a spatial diameter of 3 cm, and provide signals with frequency content up to 70 Hz only [10]. ECoG electrodes reside on the surface of the brain, average neural activity over 0.5 cm and can record signals with much higher frequency content [10]. Typically, the bandwidth of ECoG recordings is 10 Hz to 200 Hz [10]. However, this bandwidth is normally limited by the amplification hardware. New research shows that ECoG electrodes can provide signals with meaningful frequency content up to 6 kHz [18]. Intracortical microelectrodes penetrate into the cortex and have recording sites with areas similar to a neural cell body (50 μm - 200 μm) . Microelectrodes provide the least spatial averaging and can accurately record the action potential waveform from single neurons, often called single unit recording. The frequency content of signals recorded from microelectrodes is also limited by the amplification hardware; normally, frequencies up to 6 kHz are measured.

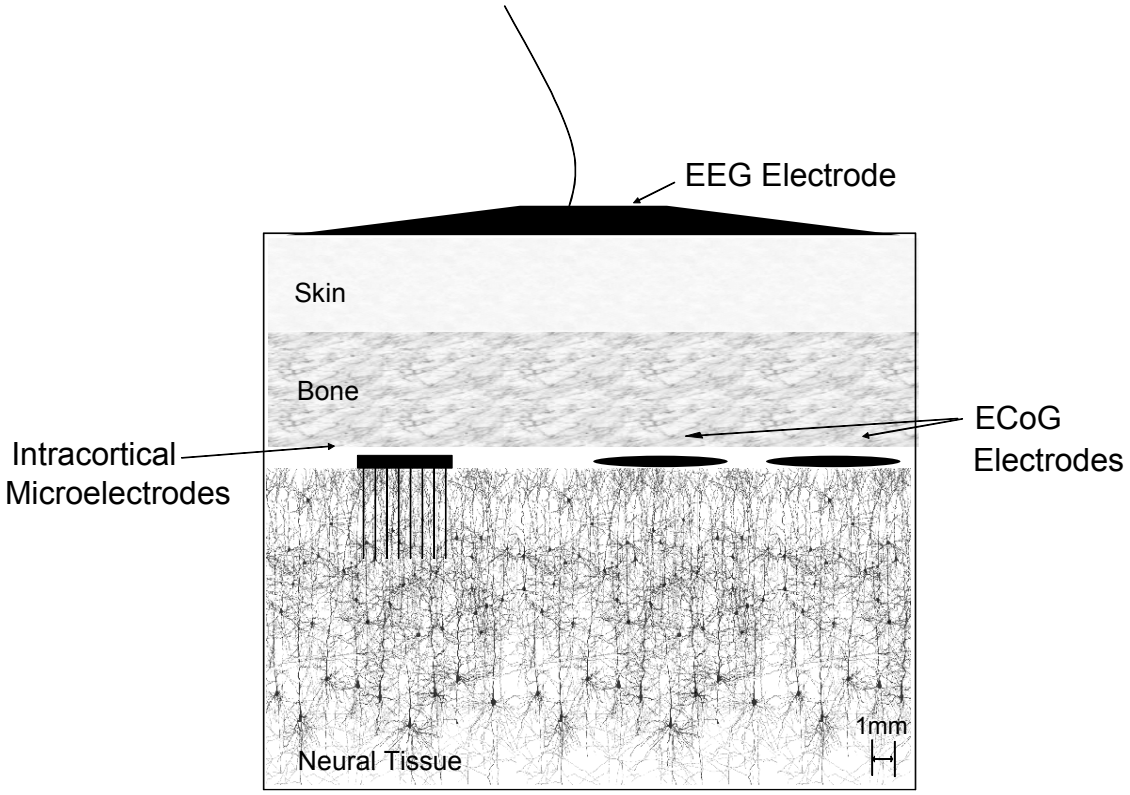

Figure 1-1. Physical representation of recording electrodes.

All papers mentioned in Section 1.1.1, which show BMI control of external devices, use intracortical microelectrode arrays for measurement of the neural signals [11–15, 17]. Their research suggests that single unit recording is useful for the analysis of complex motor function. Therefore, this work focuses on the design of a recording system that incorporates intracortical microelectrode arrays.

1.1.3 Microelectrode Array Goals, Requirements, and Challenges

The ultimate role of the intracortical microelectrode array is to provide accurate measurement of neuronal activity when chronically implanted. Long-term efficacy requires recording characteristics such as high signal-to-noise ratio, the ability to measure consistent signals from the same neurons over time, and high yield within an array. For eventual clinical use, the microelectrode array must retain a nonrestrictive interface with the patient. This requirement points toward a wireless system that measures and transmits necessary information in a minimal package. Thus, integration

with electronic circuitry and power systems is necessary for intracortical-recording microelectrode arrays used in chronic applications.

The recording characteristics are controlled by many factors; only some of which can be controlled by design. The designer can assure that the microelectrode will not catastrophically fail by mechanical or electrical means and has low noise. Thus, microelectrode arrays should be made out of robust materials that will not break nor corrode and all electronic wiring or circuitry must be hermetically sealed. Also, the microelectrodes and interface electronics must be designed to have low intrinsic noise and measures should be provided to minimize electromagnetic interference such that the signal-to-noise ratio can be as high as possible. One factor that is not controlled by the microelectrode array design is surgical placement in the cortex. The strength of the recorded signal, and hence the signal-to-noise ratio, depends on how close the electrode resides to the neuronal cell body. Also, high yield within an array requires that all electrodes in the array be placed close enough to a neuron or multiple neurons to measure their signal. Even though the designer has no control of precise electrode placement for each electrode in a static array, there is high probability that the electrode will be positioned near enough to a neuron to measure its action potential because of high neuronal density [19]. Biocompatibility is another factor determining stable recording characteristics. The relationship between material choice and biocompatibility is not straightforward and will be discussed in more detail in Chapter 2.

A current issue with commercial and noncommercial microelectrodes for neural recording is loss of signal over time. Table 1-1 shows the three most common electrode technologies used for BMIs and their efficacy over time. They include micromachined arrays from the University of Michigan and the University of Utah and non-micromachined microwire arrays. The general trend is a decrease in the number of electrodes able to record single units (i.e. active electrodes), over time. This loss of recording function over time is the result of many biological factors described in more detail in Chapter 2 that

plague all microelectrode designs listed in Table 1-1 [20]. Methods to mitigate this effect are a topic of current research in the field, though are not a part of this work.

Table 1-1. Comparison of electrode lifetimes

Technology	Electrode Material	Percentage of active electrodes over time	Reference
Micromachined silicon shank electrode with flexible cable	Pt	92%/12 weeks 92%/18 weeks	Vetter, Kipke, et al., 2004 [21]
Micromachined Silicon bed of nails electrode	Pt	45%/12 weeks 18%/52 weeks	Rousche, Normann, 1998 [22]
Micro-wire electrode	W	80%/12 weeks 45%/25 weeks	Williams, Kipke, 1999 [23]
Micro-wire electrode	Ir	62%/1 week 25%/151 weeks	Liu, McCreery, 2006 [24]

1.2 Contributions to the Field

The work presented in this document is the first step in building a fully-implantable, wireless microelectrode array for cortical recording. The project, Florida Wireless Integrated Recording Electrode (FWIRE), capitalizes on a data processing scheme that provides advantages over existing recording microelectrode system designs [25]. This work establishes a flexible platform for an implantable neural recording system integrated with microwire electrodes and an application specific integrated circuit (ASIC) amplifier. This design results in a compact device capable of being positioned subcutaneously while only the microelectrodes penetrate the cortex. A process flow using non-silicon MEMS techniques and flip-chip bonding is achieved. Two generations testing the efficacy of a micromachined, flexible, ploymide substrate with nickel [26] and tungsten [27] microwire electrodes have been realized. The latest generation with

tungsten microwire electrodes and an integrated amplifier shows adequate *in vivo* recording results over a 42 day period [28, 29]. An average noise floor of 4.5 μV_{rms} and average signal to noise ratios of 3.5 (11 dB) are consistently seen over the implant duration.

Furthermore, this work exemplifies a method for thorough electrochemical characterization of electrode recording-site materials and provides undocumented results for tungsten microelectrodes [30]. Corrosion rates for tungsten microelectrodes with and without a gold-tungsten galvanic couple are quantified in electrolytes modeling *in vivo* chemistry. Corrosion rates on the order of 100 μm/yr are seen for tungsten electrodes immersed in 0.9% phosphate buffered saline, while corrosion rates on the order of 10,000 μm/yr are seen for tungsten electrodes immersed in a solution containing 0.9 % phosphate buffered saline and 30 mM of hydrogen peroxide. The hydrogen peroxide is added to model the extracellular chemistry during a foreign-body inflammatory response. These results provide insight into the long-term longevity of tungsten microwire electrode arrays used in *in vivo* recording applications.

Moreover, a method to assess the quality of the seal between the insulation and the microelectrode surface is introduced [31]. This method uses graphical analysis of the impedance data and thus is relatively simple. This method may be used for quality control of microelectrodes used in the fields of electrophysiology or electroanalytical chemistry.

1.3 Dissertation Organization

The remaining text is organized as follows. Chapter 2 discusses the electrophysiology of a neuron, describes the physics of signal transduction at the electrode surface via electrochemical theory, and presents existing microelectrode technologies and their issues. Chapter 3 presents the physics behind the electrode-electrolyte interface and the need for electrochemical assessment of electrode recording-site materials. Chapter 4 presents sequential progress of the polymer-based UF microelectrode

array. Details of the fabrication steps of microelectrode arrays as well as bench-top characterization and acute *in vivo* results for two generations of microelectrode arrays are given. Chapter 5 explains in detail the design and characterization of a UF microelectrode array hybrid-packaged with an amplifier integrated circuit. Details of the system noise, the grounding scheme, and the requirements for interfacing with commercial data-processing and recording hardware are given. *In vivo* results show the performance of the microelectrode system for chronic applications. Chapter 7 presents the theory, experimental methods, and results of electrochemical assessment of platinum and tungsten for recording electrode materials. The corrosion of the electrode or production of unwanted chemical species is assessed. Chapter 8 summarizes the results of this work and advises a plan for future microelectrode designs.

CHAPTER 2
BACKGROUND ON MICROELECTRODES FOR NEURAL RECORDING

This chapter conveys the necessary background for the design of the UF microelectrode array. Understanding of the measurement target is presented through an overview of the neuron, followed by a discussion of the neuronal signal known as the action potential. Then, the transduction mechanism at the metal recording site and tissue interface is discussed and mathematically portrayed via electrochemical theory. The next section provides details of the structures and fabrication methods of existing microelectrodes and microelectrode arrays for neural recording applications including microwire, silicon-micromachined, and polyimide-micromachined microelectrode arrays. The strengths and weaknesses of the reviewed designs are discussed at the close of this section. Next, histological reports that portray the biocompatibility of implanted microelectrodes are reviewed. The biological immune response is identified for intracortical microelectrodes. Finally, from the background information are presented.

2.1 The Neuron

Neurons provide the means for cognitive function and as such are targeted by BMI systems. Pyramidal cells in the motor cortex, which are most commonly targeted by BMIs, provide the necessary information for motor muscle control. Their action potentials, which are electrical signals generated by the neurons, are recorded and their firing pattern is decoded in BMI systems. Figure 2-1 shows a schematic of an intracortical microwire microelectrode interfacing with neurons in the brain. If placed in close proximity to a cell, the microelectrode can record the neuron's ionic signals as it communicates with other neurons.

To understand how an action potential is generated, the physiology of a neuron is explained. The soma is the cell body; dendrites and the axon make-up the neural extensions, or neurites, as shown in Figure 2-1 [32]. The dendrites receive signals from other neurons, while the axon transmits signals to other neurons. The axon may be

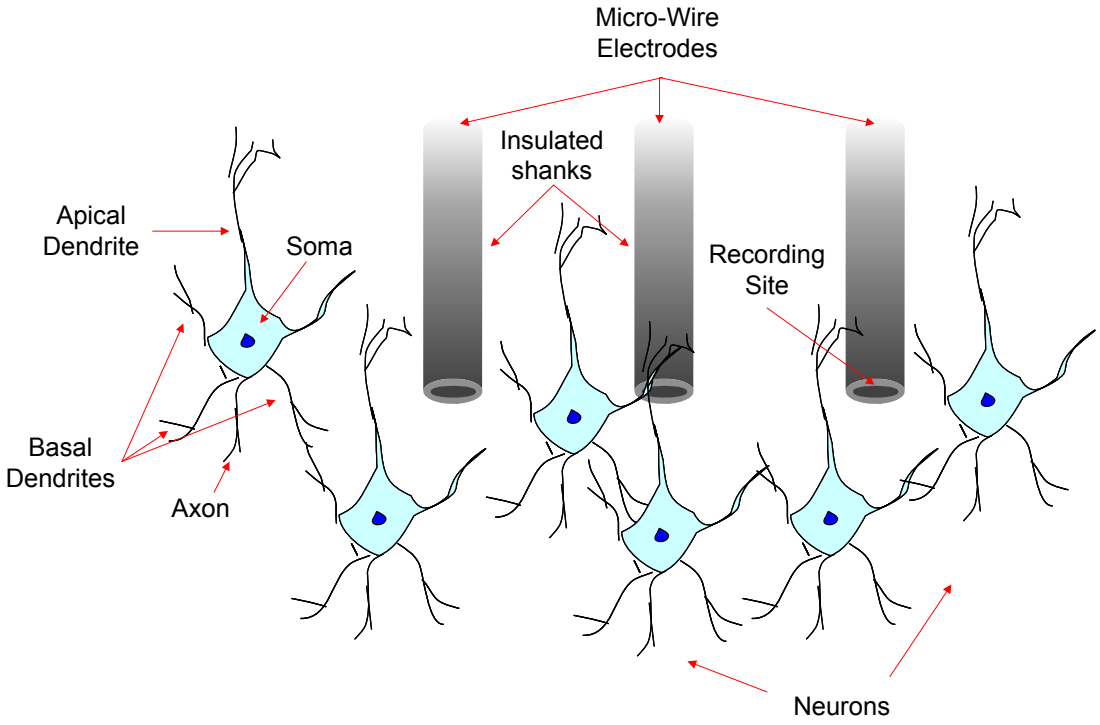

Figure 2-1. Schematic of micro-wire electrode array interface with neurons in the cortex.

insulated along its length and periodically have uninsulated nodes (Nodes of Ranvier) that act to reestablish an action potential as it propagates. Neurons are connected in a weblike fashion with the axon of one neuron attaching to the dendrites of others via a synapse. One neuron may have on the order of 10,000 dendritic connections [32]. The neuron is insulated by a thin membrane on which ion channels reside. The ion channels are gated by proteins that only allow the passage of specific ions. Ion channels may be neurotransmitter-gated or voltage-gated meaning that either neurotransmitters or voltage may modulate the proteins allowing ions to pass. Ionic current occurring at dendritic synapses has the ability to trigger an action potential in the receiving neuron by depolarizing the resting potential of the soma to a certain value. The resting potential inside a neural cell body is close to -65 mV with respect to the surrounding fluid [32]. When the afferent, or incoming, current from dendritic synapses increases the cell potential above a certain threshold voltage, an action potential proceeds as follows. Voltage-gated ion channels residing on the cell membrane open and allow the entry of

sodium ions, Na^+. This influx of sodium marks the start of an action potential. About one millisecond after the sodium channel opens, voltage-gated potassium channels open allowing the exit of potassium ions, K^+. The efflux of K^+ brings the cell potential down past its resting potential, then both channels turn off. After some time, the cell potential achieves its resting potential due to the continuous activity of ion pumps that transport ions across the cellular membrane against their concentration gradient. A representation of the intracellular waveform is given in Figure 2-2.

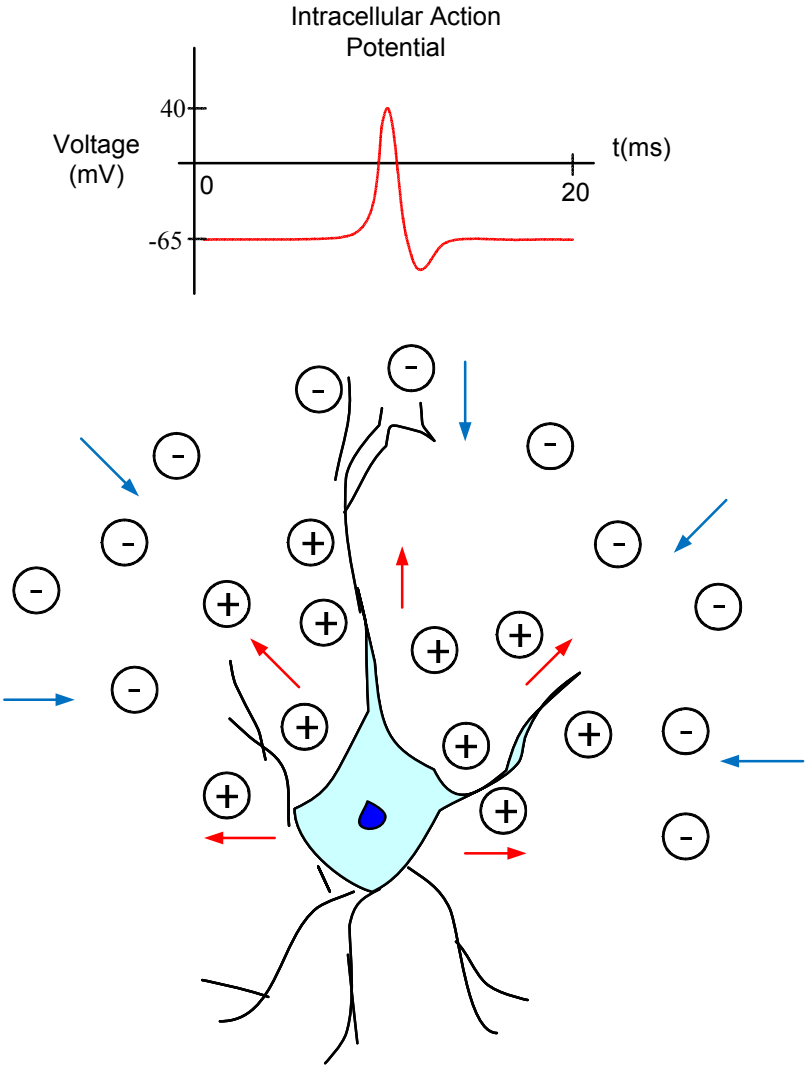

Figure 2-2. Schematic of a neuron and action potential.

Microelectrodes placed in the vicinity of a neuron measure the extracellular potential associated with an action potential. The next section will explain the underlying physics of this recording.

2.2 Extracellular Neural Recording

In viewing the recording microelectrode array as a sensor, it is important to identify the signal and how it is measured. As stated previously, intracortical microelectrodes for BMIs need to measure action potentials generated by neurons, which are physically represented by the influx and efflux of ions through a neuron's cellular membrane. Figure 2-2, presented earlier, showed the action potential waveform measured via the potential difference from the inside of the cell to the outside of the cell. An intracortical microelectrode measures the extracellular potential of a nearby neuron with respect to a distant electrode. This potential difference is then fed into a differential amplifier as shown in Figure 2-3. The waveforms shown in Figure 2-3 are characteristic of recorded and amplified signals. Henze et al. showed that the measured waveform will be close to the the first derivative of the intracellular waveform [19].

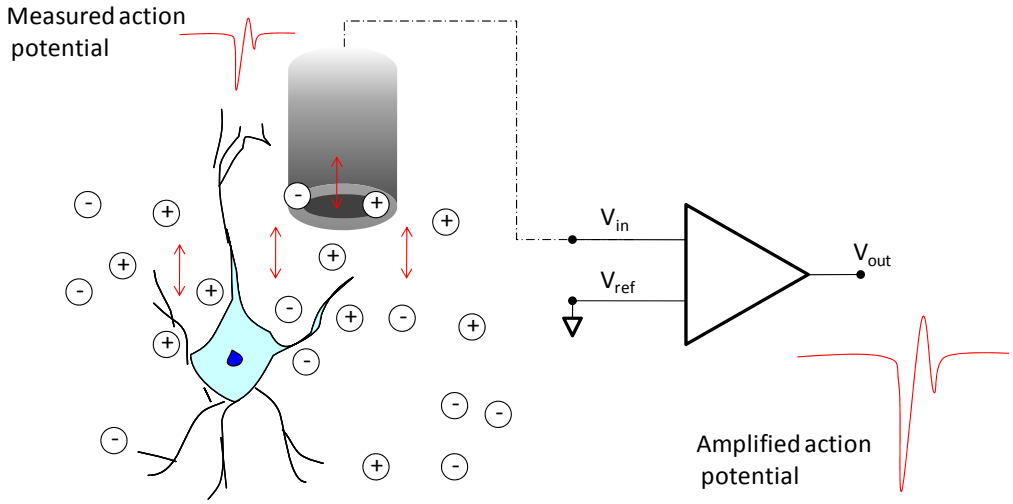

Figure 2-3. Extracellular recording of an action potential with respect to a distant electrode.

Moreover, the shape and amplitude of the recorded extracellular voltage depends on the placement of the electrode with respect to the neuron. Figure 2-4 shows

simulated results for the extracellular potential of a layer V cortical pyramidal cell during an action potential [33]. The circle in the center of the figure represents the soma, while

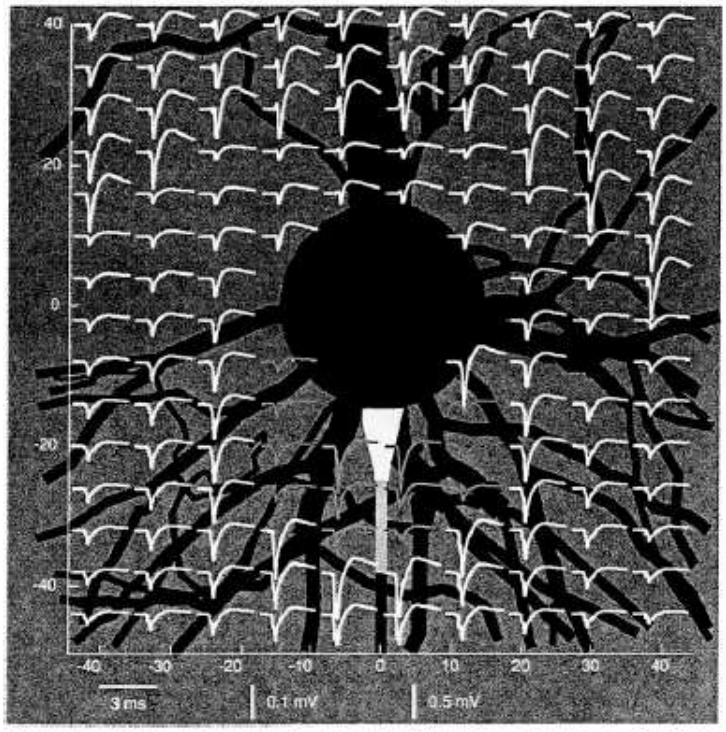

Figure 2-4. Simulated extracellular voltage from a typical layer 5 cortical pyramidal cell [reprinted from Journal of Computational Neuroscience, vol. 6, no. 2, G. R. Holt and C. Koch, Electrical interactions via the extracellular potential near cell bodies, p. 174, Figure 4, 1999, with permission from Springer Science+Business Media].

the axon hillock, shown in white, is protruding from the bottom. The apical dentritic tree protrudes from the top of the soma. Other branches are dendrites. Their results suggest that the largest potentials are near the axon hillock and that all potentials are reduced as distance away from the cell increases. Experimental results from Henze et al. showed that extracellular voltages from CA1 hipocampal rat pyramidal neurons are measurable from microelectrodes as far as 140 μm from the cell body, but that amplitudes greater than 60 μV must be measured within 50 μm [19]. Drake et al. reported that the farthest distance they could experimentally record from a neuron cell body in the rat cortex is 180 μm [34]. Thus it is clear that the relative placement of the microelectrode with

respect to the neuron determines the magnitude and shape of the measured action potential.

Physics of extracellular Recording: Quantitative physical insight can be obtained from the phenomenological discussion above through the use of electrochemical theory, named electrodiffusion in the literature [35]. The transient voltage measured with respect to a distant reference electrode is determined by the changing concentration of ionic species near the recording electrode. The mathematical relationship between electrostatic potential and ionic concentration are discussed next.

The governing equation for the ionic flux in dilute solutions for one species, N_i, is given as

$$\mathbf{N}_i = -z\mu_i F c_i \nabla\Phi - D_i \nabla\, c_i + c_i \mathbf{v}, \tag{2–1}$$

where $\mathbf{N}_i$ is expressed in mol·cm^{-2}·s^{-1}, z_i is the number of proton charges carried by the ion, u_i is the mobility of the species, F is Faraday's constant, c_i is concentration, Φ is electrostatic potential, D_i is the diffusion coefficient of the species,and $\mathbf{v}$ is the velocity of the bulk fluid [36]. The three terms on the right side of the equation correspond to mass transport due to electric-field-induced drift, diffusion, and convection, respectively. In this case, the convection term is zero.

Next, mass balance for a volume element requires that the accumulation, or time rate of positive change of the concentration, must equal the negative of the divergence of the flux.

$$\frac{\partial\, c_i}{\partial\, t} = -\nabla \cdot\ N_i. \tag{2–2}$$

Combining (2–1) and (2–2) gives a time dependent differential equation relating potential and concentration.

$$\frac{\partial\, c_i}{\partial\, t} = z\mu_i F c_i \nabla\Phi + D_i \nabla\, c_i \tag{2–3}$$

Using Poisson's equation allows one to solve for the potential for given initial and boundary conditions. Poisson's equation is given as

$$\nabla^2\Phi = \frac{\rho}{\varepsilon} = \frac{-\sum z_i c_i F}{\varepsilon}, \tag{2–4}$$

where ρ is charge density and ε is the permittivity of the medium. The voltage measured by the differential amplifier is

$$\triangle\ V = \Phi_e - \Phi_{ref}, \tag{2–5}$$

where Φ_e is the electrostatic potential at the intracortical microelectrode and Φ_{ref} is the electrostatic potential at a distant reference electrode. In many recording systems, the reference electrode is a large area metal screw that is driven through the skull and rests in the cerebrospinal fluid above the cortex. Therefore, only single unit action potentials from neurons near the implanted microelectrode are recorded. This derivation provides the mathematical framework for numerical modeling of the potential measured by microelectrodes. Future modeling studies could investigate the effects of electrode size and scar tissue encapsulation on the measured potential waveform.

The next section reviews the design, structure, and fabrication of existing intracortical microelectrodes and microelectrode arrays.

2.3 Microelectrode Arrays for Neural Recording

The UF microelectrode array incorporates strengths from many of the existing microelectrode array designs. This section highlights the designs and fabrication steps of microelectrodes and microelectrode arrays used for neuronal recoding from the 1970's to the present.

2.3.1 Single Microwire Electrodes

Salcman pioneered the way for single unit recordings with glass or polyimide insulated Pt/Ir microwires that were individually implanted into the cortex [37, 38]. The purpose of his design was to allow for the implanted electrodes to be connected to a very thin and flexible wire that would provide strain relief for brain motion with respect to

the skull. However, their design was not practical for recording from a large number of neurons. Hence, following designs incorporated arrays of recording sites.

2.3.2 Microwire Arrays

Microwire arrays have a simple form. They use commercially available wires with diameters ranging from 20 to 50 μm and materials that are strong enough to be manipulated without bending and inserted into the neural tissue without buckling (typically tungsten, iridium, or a platinum/iridium alloy). The wires are typically coated with a few micrometers of an insulating polymer and held in an array by some connecting structure. A detailed description of microelectrode arrays made from discrete wires was given by Williams [23]. A jig was used to separate and secure 35 μm diameter tungsten microwires insulated in polyimide while they were assembled into a row of 11 parallel wires and attached to a connector. The final array consisted of two rows of eleven microwires, cut to the same length by tungsten-carbide surgical scissors, and electrically connected to a back-end connector. Lui et al. constructed microwire arrays from Pt/Ir wires insulated in parylene-C that were 35 or 50 μm in diameter and electrochemically polished to a conical tip. Sixteen wires were perpendicularly attached to a backplate in a 4 by 4 grid [24]. Two companies have commercial microwire arrays that resemble these published designs: Tucker Davis Technologies and Microprobe, Inc. Tucker Davis Technologies uses polyimide coated tungsten microwires and printed circuit board technologies to make arrays of 16 electrode sites (2 rows of 8 wires) [39]. The microwires are bonded to a printed circuit board that attaches to a connector. Many other configurations without the printed circuit board are also made by the company. Microprobe Inc. makes arrays out of Pt/Ir or tungsten microwires that are sharpened to a point and have parylene-C as the insulating material. They also have a design in which the microwires are attached perpendicular to a back-plate with a flexible cable of wires extending to a connector (not shown in Figure 2-5) [40].

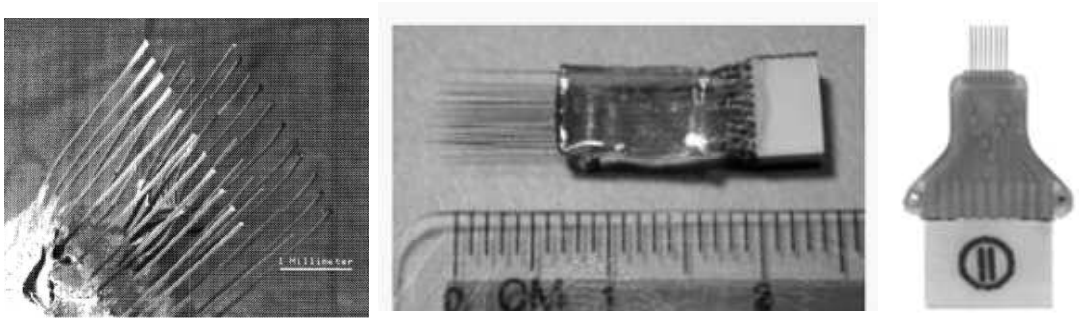

a. b. c.

Figure 2-5. Microwire electrode arrays. a) Williams array [reprinted from Brain Research Protocols, vol. 4, no. 3, J. C. Williams et al., Long-term neural recording characteristics of wire microelectrode arrays implanted in cerebral cortex," p. 305, Figure 2, 1999, with permission from Elsevier. b) MicroProbe Inc. array. [http://www.microprobes.com/] c) Tucker Davis Technologies array. [http://www.tdt.com/]

2.3.3 Silicon Micromachined Microelectrode Arrays

Though microwire arrays have been proven to be effective, micromachined electrodes introduce many advantages that are attractive to researchers in the field. Advantages include precise control of electrode geometry and spacing, the elimination or reduction of time consuming hand-assembly steps, and most importantly, the ability for integration with interface electronics necessary for wireless implantable systems. The sequential progress of two leading designs of silicon microelectrode arrays will be discussed next, followed by other less common designs.

2.3.3.1 The Michigan array

The University of Michigan has a current Si microelectrode array based on 38 years of research. Kensall Wise in 1970 (then at Stanford) published a micromachining process to build a planar array of one to three 10 mm $\times$ 100 μm $\times$ 100 μm Si beams that tapered to a point. Gold lines were deposited on the beams and all but a 1000 μm^2 recording area at the tip was insulated with SiO_2 [41]. Microelectromechanical System (MEMS) technology was just beginning at that time and process techniques such as photolithography, wet chemical etching of bulk Si, and vapor deposition and

electroplating of metals were used. In 1985, Wise and Najafi published a refined version of the aforementioned microelectrode [42]. Design changes included a single Si shank, or beam, with multiple electrode sites along the top surface. Changes in the fabrication process included diffusion of boron that effectively defined the probe geometry when used as etch stop in the wet chemical etch. Tantalum or polysilicon lines were deposited between either silicon oxide or silicon nitride dielectric layers as the electrode leads. Then gold was deposited and patterned to form the recording sites. The resulting probe dimensions were 3 mm length, 50 μm width at the base and 25 μm at the tapered end, and 15 μm thickness. Their process flow was compatible with the integration of complimentary metal-oxide-transistor (CMOS) electronics. In 1986 and 1992, the Michigan group published results incorporating amplification, multiplexing, and buffering electronics on their previous design [43, 44].

The next addition to the Michigan microelectrode design was a Si ribbon cable made to provide a flexible interface between the Si microelectrode and back-end connections [45]. Discrete insulated wires used for interconnections in previous designs would often fail over time rendering the implanted probe useless and proved to be a manufacturing burden [45]. The Si cable was fabricated using a process flow similar to the microelectrodes discussed before. Cables 2.5 cm long, 100 μm wide, and 5 μm thick were made. They were then ultrasonically wire-bonded to a microelectrode and the connection point was reinforced with a bead of silicone rubber. Figure 2-6 shows a diagram of a Michigan microelectrode array and a picture of a completed one with multiple shanks making a 2-D depth array. Neural Nexus is a spin-off company from the University of Michigan that sells numerous variations of the 2-D Michigan microelectrode arrays.

The next advancement of the technology was to make a 3-D array. Hoogerwerf et al. reported a design that bonds 2-D Si microelectrode arrays perpendicularly to a Si platform with an integrated Si cable [46]. The 2-D arrays were fit through slots in the

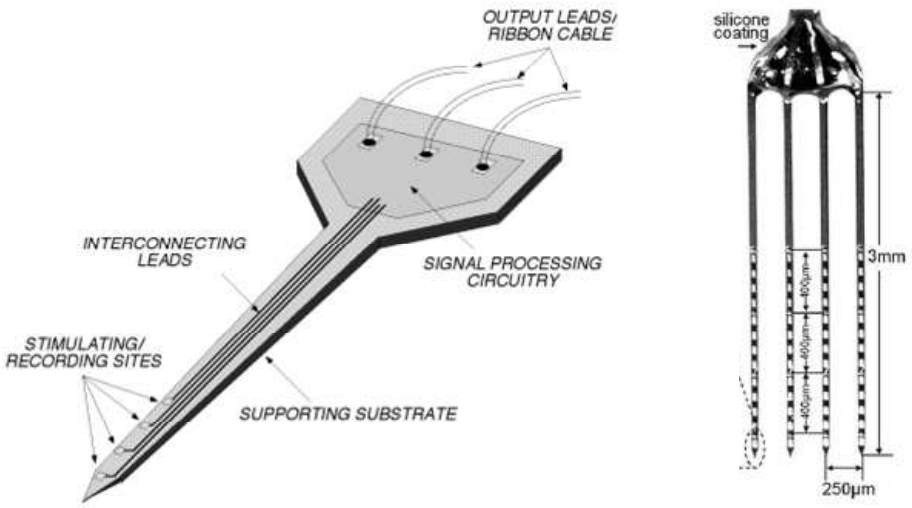

a. b.

Figure 2-6. Examples of the 2-D Michigan microelectrode array. a)[Reprinted from Proceedings of the IEEE, vol. 96, K. Wise et al., "Microelectrodes, microelectronics, and implantable neural microsystems," p. 1185, Figure 1, 2008, with permission from IEEE.] b)[Reprinted from Annual International Conference of the IEEE Engineering in Medicine and Biology Society, R.J. Vetter et al., "Development of a Microscale Implantable Neural Interface (MINI) Probe System," p. 7342, Figure 2, 2005 with permission from IEEE.]

platform, held in place by spacer bars, and then were electrically connected by selective electroplating nickel to bridge the gap between platform and array. The interconnect structure was then hermetically sealed by reflowed glass and epoxy. A figure of the 3-D array is shown in Figure 2-7. A summary of more modifications to the Michigan design are described here. Later designs changed the recording-site metal from gold to platinum or iridium [21, 47], incorporated parylene rather than Si cables [48] and added wireless capability [47, 49]. The general approach suggested by Michigan for future microelectrode arrays is to have all amplification, signal processing, telemetry, and power electronics resting subcutaneously on the skull. Flexible parylene cables were used to connect two or three dimensional Si microelectrode array implanted in the cortex, distancing the electronics and reducing the susceptibility of tissue heating [49].

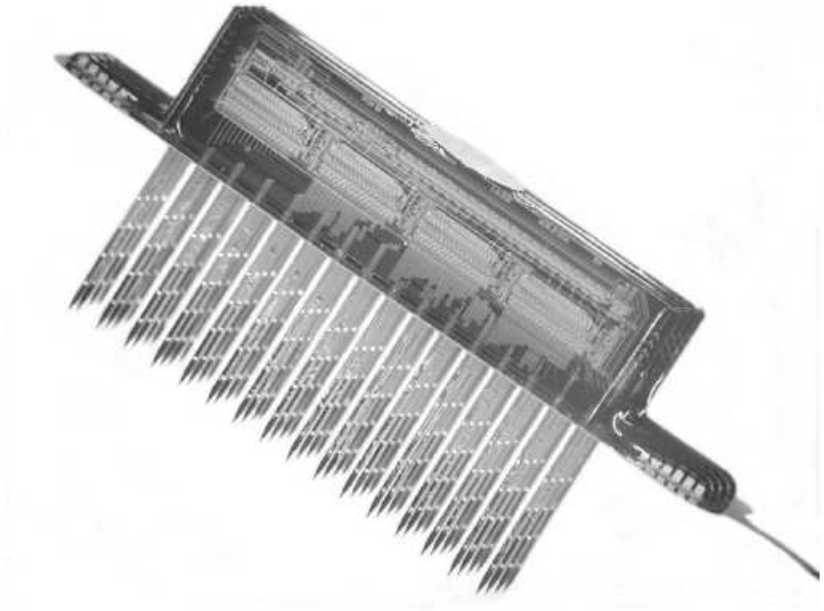

Figure 2-7. 3-D Michigan microelectrode array [reprinted from Proceedings of the IEEE, vol. 96, K. Wise et al., ”Microelectrodes, microelectronics, and implantable neural microsystems,” p. 1188, Figure 5, 2008, with permission from IEEE].

2.3.3.2 The Utah array

The Utah array is the other popular micromachined microelectrode array. Richard Normann, the founder of the Utah array, first designed the Utah array for a visual stimulating prosthesis, where local stimulation was applied in the visual cortex [50]. It has since been widely used as a CNS recording prosthesis as well. Cyberkinetics licensed the technology and has marketed the Utah microelectrode array with their ”Brain Gate” system for recording in the central nervous system. A clinical trial was performed with the Brain Gate system as a BMI for the severely motor impaired [17].

The Utah array was first fabricated as follows. Starting from a 1.7 mm thick silicon wafer, thermomigration was performed to make trails of p^{+}Si from one side of the wafer to the other in a 10 by 10 array. A dicing saw was used to cut in the spaces between the doped Si trials leaving a three dimensional structure of 1.5 mm columns that are electrically isolated at the base by pn junctions. The columns were 150 μm square and 1.5 mm tall, with center to center spacing of 400 μm. The structure was then put through

two isotropic wet etches to first decrease the column area and then to taper the tips. The resulting geometry of one probe is a cone shape while the group resembles a ”bed of nails”. Gold and platinum thin film layers were deposited consecutively on the first 50 μm to 100 μm of each tip and thin gold wires were bonded to the backside of the wafer making the interconnect.

The next generation of Utah arrays shown in Figure 2-8 included the following changes. A different layering of tip electrode metals (Pt/Ti/W/Pt) was used and an insulation layer of polyimide was placed on the remaining part of the the probe shanks [22, 51]. Also, the electrical isolation of electrodes was improved by using a glass dielectric as the insulation between the probe sites on the back of the wafer [51]. Later changes in the fabrication process allowed the length of the probes to vary in one direction, effectively giving a three dimensional array of the recording sites in space [52]. In a more recent publication, batch fabrication is shown for the Utah array in

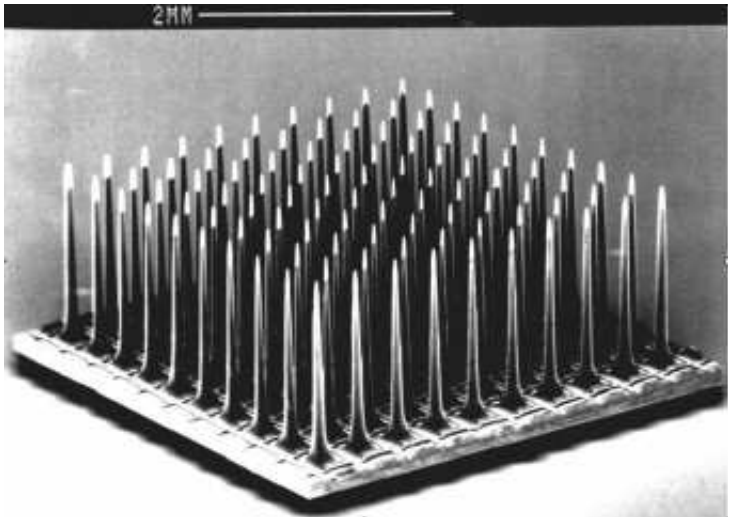

Figure 2-8. Utah microelectrode array [reprinted from Proceedings of SPIE - The International Society for Optical Engineering, R. Bhandari et al., ”System integration of the Utah electrode array using a biocompatible flip chip under bump metallization scheme, p. 1567, Figure 1, 2007 with permission from IEEE].

which they tout a maskless process. Here parylene-c is used instead of polyimide as an insulation for the Si probe shanks, and the etching scheme has been changed to

increase geometrical uniformity by incorporating a customized wafer holder which spins the wafer in the etching solution [53].

Most recent publications show the design of a fully implantable, wireless system. Utah's approach is to flip-chip bond all electronics and power and telemetry hardware onto the the back of the Si platform on which the electrodes are fabricated [53]. The electrodes are implanted into the cortex while the electronics rest on the top of the cortex. The design is constrained by tissue heating because of the close proximity to neural tissue [54].

2.3.3.3 Other Si microelectrode arrays

Two other Si micromachined microelectrode arrays to note are discussed here. One design is by a group in Sweden affiliated with the company Acreo and the other is by a group at Arizona State University. Both have, novel design concepts; however, neither have received as much reference in literature as the Utah or Michigan arrays.

The group from Sweden fabricated arrays (named VSAMUEL) similar in shape to the Michigan array in that electrode sites were placed along the shank of Si micromachined probes [55]. The difference in their process flow was the use of a silicon on insulator (SOI) wafer and the use of deep reactive ion etch (DRIE) for the removal of the bulk silicon. In a later publication, they discussed the ability to use a direct write system that will customize electrode site layout in a practical manner [56]. Instead of using masks to etch the silicon nitride insulation layer on top of the recording sites, they use a direct write laser beam to open the Pt or Ir recording sites. This reduces cost in producing custom designs that need, for example, a variation of electrode spacing [56].

A collaboration between Arizona State University and Sandia National Laboratories resulted in a Si-based actuated microelectrode array [57]. To circumvent loss of signal over time, this group designed and fabricated a system that allowed repositioning of the implanted microelectrode array. They used the SUMMiT-V microfabrication technology to build thermal actuators into a probe structure. Two recording electrodes could be moved

up or down in steps via a MEMS structure that used a ratchet scheme. Preliminary *in vivo* results were given, but no publications on its efficacy have been found.

2.3.4 Polymer Micromachined Microelectrode Arrays

In order to better mechanically match the softer and more flexible neural tissue, polymer-based-intracortical-microelectrode arrays were introduced to the field [58, 59]. In 2001, two groups published independent papers on polyimide-based microelectrodes. Only a handful of other designs have emerged since then. Most will be discussed in this section. The Arizona State design is described first.

A research effort starting at Arizona State University by Daryl Kipke's group used micromachining techniques to process a microelectrode structure that consisted of a layer of thin-film metal sandwiched between 10 μm thick layers of polyimide [58]. Using a Si wafer to handle the processing steps, a sacrificial layer of SiO_2 was deposited, then polyimide was spin deposited and cured, followed by gold deposition and patterning. Then a top layer of polyimide was spun as the top insulation layer. Reactive ion etching removed polyimide from the 30 μm by 30 μm recording sites and larger bond pads. Platinum was deposited and patterned as the final electrode material. Then the polyimide structure was removed via chemical etch from the handle wafer. Their devices had two recording sites on one polyimide shank and a variety of designs with three or more shanks. One example is depicted in Figure 2-9. The devices were highly flexible and would buckle under the force needed for insertion through the cortex, so incisions had to be done in order for the microelectrode array to be implanted [58]. Acute studies showed promising results in their first publication.

Later publications by Kipke, who had since moved to the University of Michigan, introduced a parylene-based microelectrode array with microfluidics for drug delivery [60] and an open architecture microelectrode with subcellular dimensions seen in Figure 2-10 [61]. The second parylene design was not yet a functional microelectrode in

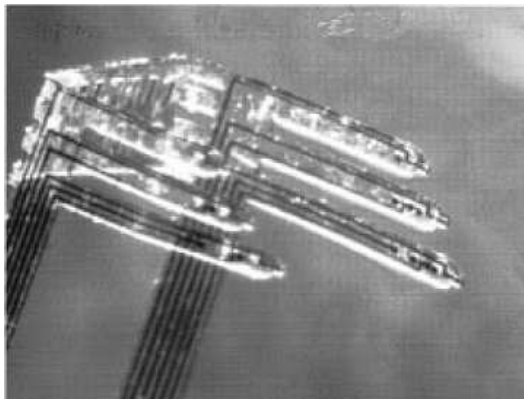

Figure 2-9. Polyimide-based microelectrode array (Arizona State, Gen 1) [reprinted from IEEE Trans. Biomed. Eng., P. Rousche et al., Flexible polyimide-based intracortical electrode arrays with bioactive capability, vol. 48, no. 3, p. 363, Figure 1(g), 2001, with permission from IEEE].

that no recording sites were made on the structure. Their goal was rather to assess the tissue reaction to the polymer implant for subsequent versions.

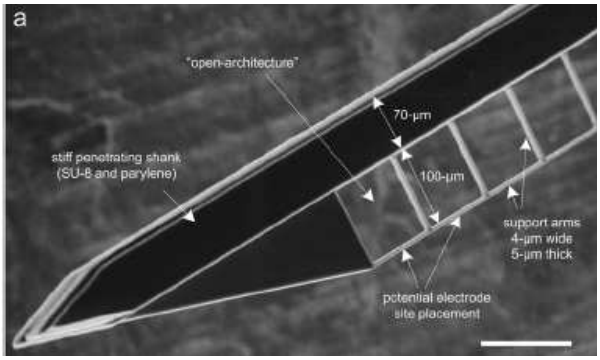

Figure 2-10. Parylene-based microelectrode array (U. of Michigan) [reprinted from Biomaterials, J. Seymour and D. Kipke, Neural probe design for reduced tissue encapsulation in cns, vol. 28, pp. 3596, Figure 1(a), 2007, with permission from Elsevier].

A new group at Arizona State published a next generation of the Kipke microelectrode in reference [58]. They designed for increased stiffness that allowed implantation into the cortex without buckling [62]. Using an SOI wafer, a similar polyimide-metal structure was fabricated. The structure was then removed from the bulk Si resulting in a 20 μm thick polyimide structure with 5 μm of Si beneath. Si was then selectively etched

away from sections requiring flexibility such as the back-end cable. A photograph is the devices is shown in Figure 2-11.

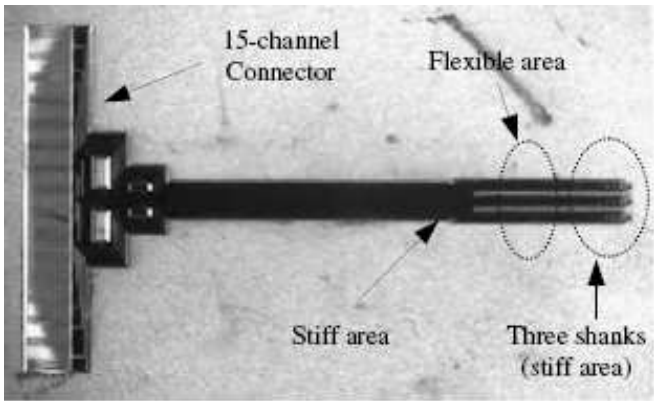

Figure 2-11. Polyimide-based microelectrode array (Arizona State, Gen 2) [reprinted from Journal of Micromechanics and Microengineering, K. Lee et al., "Polyimide-based intracortical neural implant with improved structural stiffness. vol 14, issue 1, p.35, Figure 4(a), 2004, with permission from IOP].

Stieglitz and Gross, of Germany, published a similar polyimide microelectrode design as the Kipke group in 2002, except their fabrication process allowed for front and back side electrode arrangements as depicted in Figure 2-12 [63]. They also plated platinum black on the electrode sites to decrease their impedance. This group has numerous papers on sieve, cuff, and planar polymer electrode arrays that are mainly geared for PNS stimulating and or recording prostheses [64]. The publication mentioned first [63] was the only polymer-based microelectrode targeting intracortical recording and no *in vivo* results were given.

Another research group that has experience in fabricating polymer microelectrode arrays is at the University of Tokyo [65]. They have published a series of designs using polyimide and parylene-C. Their first device was a planar polyimide array fabricated much like the ones already mentioned; however, they incorporated a magnetic layer (nickel) on the shanks that allowed the electrode shanks to be tilted out of plane in a magnetic field as shown in Figure 2-13 [65]. The microelectrodes, perpendicular to the

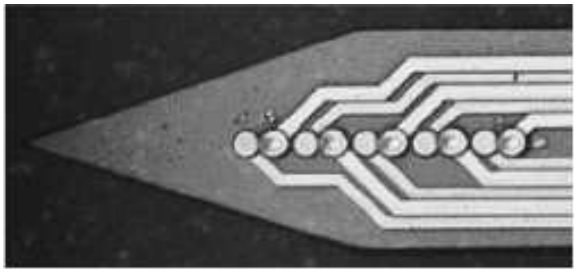

Figure 2-12. Polyimide-based microelectrode array (Fraunhofer Institute) [reprinted from Sensors and Actuators B: Chemical, T. Stieglitz, "Flexible BIOMEMS with electrode arrangements on front and back side as key component in neural prostheses and biohybrid systems." vol. 83, p. 12, figure 5, 2002, with permission from Elsevier].

cable and back-end connection, were then inserted without buckling into the brain for acute results.

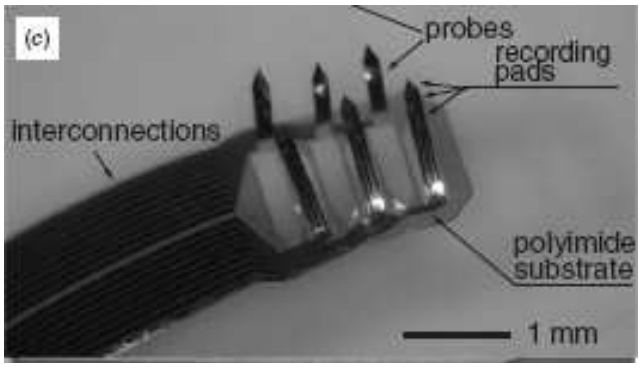

Figure 2-13. Polyimide-based microelectrode array (U. of Tokyo) [reprinted from Journal of Micromechanics and Microengineering, S. Takeuchi et al., 3d Flexible multichannel neural probe array, , vol. 14, p. 106, Figure 4(c), 2004. with permission from IOP].

This group's next series of publications changed gears and started with a design that used parylene-C and microfluidic channels. Again, metal for the electrode sites and lead wiring was sandwiched between layers of parylene-C [66]. Microfluidic channels were structured in the parylene layers by patterning photoresist between the layers and subsequently removing it, leaving a void [66]. Photographs of this device are shown in Figure 2-14. In this paper, insertion into the cortex was achieved by inserting heated polyethylene glycol (PEG), a biodegradable polymer, into the microfluidic channel. After

cooling, the PEG made the structure stiff enough to be inserted in to the tissue without buckling. Over time, the biodegradable polymer would dissolve leaving the flexible parylene structure in the brain. Subsequent papers, used this same design and added biodegradable microspheres with bioactive agents to the PEG [67, 68]. Neural growth factor (NRG) was encapsulated in microspheres which were seeded in PEG and set in the microchannel. Acute results were given showing potential for future use [68].

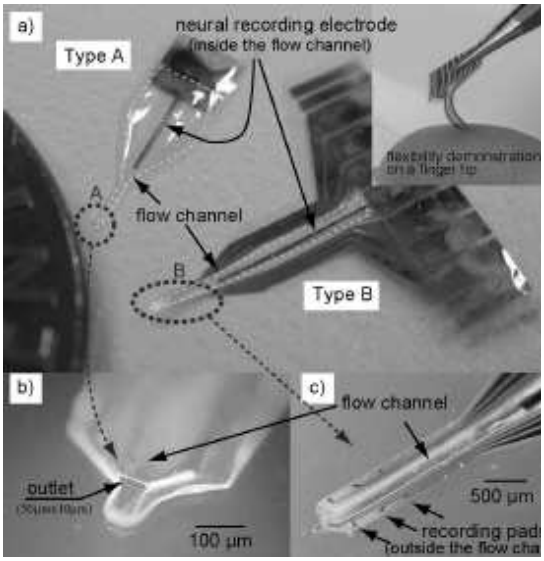

Figure 2-14. Parylene-based microelectrode array (U. Of Tokyo) [reprinted from 26th Annual Internationals Conference of the IEEE EMBS, T. Suzuki et al., Flexible neural probes with micro-fluidic channels for stable interface with the nervous system, p. 4058, figure 3, 2004, with permission from IEEE].

The final design discussed in this section refers to a publication from Karen Cheung at the University of British Columbia. , A flexible microelectrode array is made using polyimide (shown in Figure 2-15), which geometrically resembles a single shank Michigan microelectrode array [69]. The metal for the electrode sites as well as lead wiring is platinum. There were 16 electrode sites, 25 μm in diameter, patterned in a row on a 15 μ m thick, 2 mm long, and 195 μm wide shank, which tapered to 35 μ m. A longer, monolithicly-fabricated cable attached to a back-end connector. They claimed their flexible device was implanted without bulking and caused minimal immune response after 8 weeks *in vivo*.

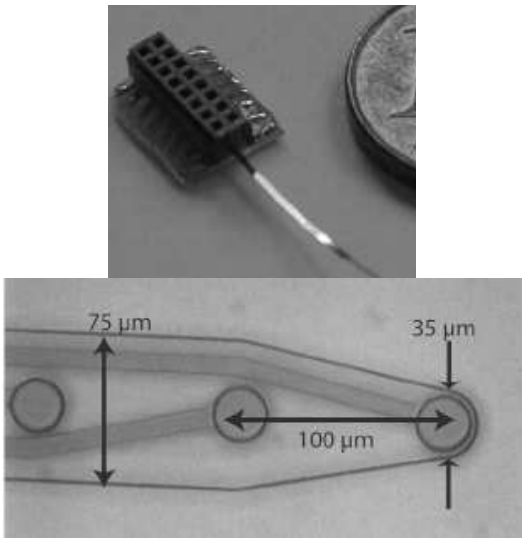

Figure 2-15. Polyimide-based microelectrode array (U. of British Columbia) [reprinted from Biosensors and Bioelectronics, K. C. Cheung et al., Flexible polyimide microelectrode array for in vivo recordings and current source density analysis, vol. 22, no. 8, p. 1786, Figures 2(a), 3(a), 2007, with permission from Elsevier].

2.3.5 Comprehensive Microelectrode Array Summary

Micro-wire arrays have been the workhorse microelectrode design for research labs using BMIs for neural prostheses [11, 12]. They possess the necessary small size needed for implantation and are well established in the field [70]. However, it is difficult to scale-up microwire arrays due to assembly and size constraints. The increase in the number of total recording sites, consistency of recording-site geometry and surface structure, and integrated electronics, are some advantages of micromachined microelectrodes over discretely assembled micro-wire arrays. Si-micromachined electrodes such as the Michigan and Utah probe have been gaining popularity. Clinical trials with the Utah electrode have occurred [17].

The reviewed micromachined microelectrode designs also have distinct disadvantages. The Michigan and VSAMUEL array have recording sites that are positioned along the shank of the probe. Thus, the majority of the recording sites will be recording from neural tissue that has been damaged during the implantation process. It may be argued

that the quality of the recorded signals from those sites will be decreased compared to a recording site placed at the tip of a probe. Furthermore, one documented issue with the Michigan electrodes is that they are prone to breaking during implantation because of their fragile nature [71]. The Utah array design also has some issues. First, the length of the implanted probes are limited to the thickness of the bulk silicon wafer (1.5 mm) [72]. Severe tissue encapsulation due to the dense array has been documented for the Utah array that directly led to inhibited recording performance and eventual migration out of the cortex [22]. Also, in designs that incorporate electronics onto the backside of the Utah electrode, power constraints due to tissue heating are a concern [54].

Polymer-based micromachined microelectrode arrays have the same advantages as Si-micromachined electrodes plus the possible benefit of a better mechanical match to the soft neural tissue and increased strain relief from external forces. However, all of the polymer-based designs have electrode sites placed on the side of the probe shank rather than the tip and the majority of the designs must require an incision into the neural tissue before implantation. Moreover, whether polymer-based microelectrode arrays really do increase the longevity of neural recording is yet to be unequivocally determined. What has been documented is both the acute and chronic response of brain tissue to intracortical microelectrodes. This immune response is discussed next.

2.4 Tissue Response to Intracortical Microelectrodes

The reason for the decrease in active electrodes over time as shown in Table 1-1 is investigated in this section. Based on histological studies of brain tissue after prolonged implantation, researchers have a detailed understanding of the immune response to microelectrodes [20, 73, 74]. Their results suggest the foreign body (i.e. microelectrode array), elicits a chronic immune response that has detrimental effects to surrounding healthy neurons.

Before the histological results are discussed, a review of the cellular make-up of the brain is given. The cells that constitute brain tissue are neurons and glial cells,

which consist of oligodendrocytes, astrocytes, and microglia [20]. Neurons, account for less than 25% of the total number of cells. The glial cells make up the remaining. Oligodendrocytes create myelin found on neurons. Astrocytes and microglia respond to injury in the brain. When an injury occurs, the astrocytes and microglia become activated and move to the injury site [75]. Microglia secret reactive oxygen intermediates (ROIs) in what is called the ”respiratory burst” [75] as well as cytotoxic enzymes. Their goal is to break down cellular debris and consume damaged cells. The production rate of the ROIs in microglia increases greatly when activated. ROIs include O_2^-, H_2O_2, and OH^-.

Researchers have given histological reports on the immune response of the brain to silicon [74, 76] and polymer [61] based microelectrodes. All reported two immune responses: one due to the injury imposed by the implantation of the electrodes and another due to the persistent presence of the microelectrodes. The injury of the neural tissue caused by insertion signaled activated astrocytes and microglia to migrate to the area of implant. A cluster of these cells, called a glial scar, could be seen as far as a few hundred micrometers around the implant [76]. This response was dependent on probe size as a larger probe would do more damage to the surrounding tissue during insertion. Over time the initial wound response would diminish and all papers reported a more compact sheath of cells containing reactive astrocytes and activated microglia around the implanted microelectrode. This sheath of cells would remain constant after four weeks of implantation [73] and did not correlate to the size of the implanted probe (except for subcellular sizes [61]). Thus, the authors surmised that this response was due to the chronic presence of the probe.

Three theories exist on the effect of immune response on the recording properties of the microelectrode. The glial scar that forms around the microelectrode either 1) electrically isolates the electrode from endogenous electrical signals, 2) physically moves nearby neurons away from the electrode or, 3) releases cytotoxic chemicals

that result in neuronal death. An *in vitro* study showed that layers of cells mimicking an inflammatory, or immune reaction, placed on a microelectrode only increased the impedance seen by the electrode by 2-3 times, which is not enough to be the cause of signal loss [77]. Biran et al. surmised that if neurons were being displaced from the electrode they would see a higher density of neurons outside of the glial scar [74]. Their results were not consistent with that theory and instead showed that chronic immune response, as well as creating a thick sheath of cells around the implant, actually results in the death of nearby neurons. Biran et al. showed that within a 100 μm radius of the implant there was a 40% loss of neurons. They suggested that neuronal death due to the presence of active microglia is the major contributor to diminishing recording performance over time. Corroborating this statement, researchers linked the damage of neurons in neurodegenerative diseases such as Alzheimer's Disease, amytrophic lateral sclerosis (ALS), and Parkinson's disease to ROIs produced by reactive microglia [78].

In summary, it was surmised that the chronically implanted microelectrode array will elicit a continual immune response, which allows microglia to be continually activated and release cytotoxic chemicals [73]. It was shown that due to the release of such chemicals, the neurons near the implant die, and it was proposed that this mechanism rather than electrical isolation or the distancing of neurons due to a glial scarring was the most significant contributor to decreased recording capability over time[79]. Thus, the next logical progression of research was to assess why the microelectrodes were producing a chronic immune response.

Strain Induced Immune Response: Recent studies showed a difference in microglial activity in implants that are rigidly tethered to the skull to ones that are floating in the brain [79, 80]. The histological studies reviewed in Section 2.4 conventionally tethered the implanted array to the skull of the subject. The tethering consisted of securing the implanted shank at the craniotomy site to the surrounding skull with a rigid medical adhesive [73, 74, 76]. Figure 2-16 shows how a typical rigid microelectrode

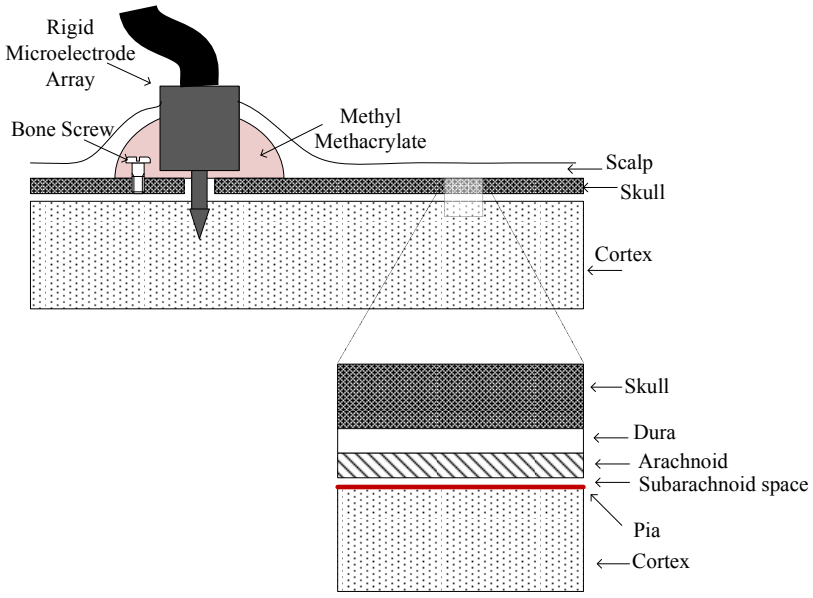

Figure 2-16. Typical tethering scheme of a rigid microelectrode array. Inset shows the meningial layers.

array is implanted in the brain and secured to the skull via a bone screw and methyl methacrylate – a bonding cement. The inset shows the meningial layers between the skull and the surface of the cortex. The dura is the first membrane below the skull to which the arachnoid layer is attached [81]. The pia is a membrane attached to the surface of the cortex. In between the pia and the arachnoid layer exists a space filled with cerebral spinal fluid that cushions the brain [81]. The absence of mechanical attachment in the subarachnoid space also allows the brain to move with respect to the skull when the head undergoes large rotational accelerations [37].

If a force is applied to the back-end of the rigid microelectrode in Figure 2-16 (the part protruding from the skull), strain may be transferred along the probe. This may act to loosen the skull connection over time as well as displace the electrode tip within the brain tissue. Moreover, if the brain moves with respect to the skull under head rotation, the tip of the implanted electrode will move with respect to the brain if it is rigidly connected to the skull.

Front-end strain relief is not a new concept. Salcman et al. discussed in their 1973 paper the need for strain relief of a single microwire electrode for chronic neurophysiologic recordings [37]. They recognized that an implanted electrode can be displaced relative to its secured connection point at the skull due to rotation of the head and subsequent movement of the brain with respect to the skull. Their electrode design, which implemented a thin, flexible, gold wire between the electrode in the cortex and the external connection, limited motion of the electrode tip to 10 μm for a 1 mm displacement of the brain with respect to the skull.

However, as microelectrode arrays rather than single electrodes became necessary for BMI systems, front-end strain relief was omitted in many Si-based designs in order to incorporate many electrode channels. Two exceptions, the Utah and Microprobe "bed of nails" designs claim to have front end strain relief by having thin and flexible gold wires connecting the implanted electrodes to the back-end connector. No modeling has been done to quantify how well their wire bundle provides strain relief, however. A "back of the envelope calculation" suggests that if they use 25 μm diameter wire-bonding wire as the single connection to the electrode channels, then the resulting effective thickness of the 100 wire cable is 100$\times$25 μm or 250 μm, which would have significantly reduced flexibility. Moreover, the hybrid nature of the back-end wire connection is prone to failure.

Mechanical modeling of tethering induced strain has been performed for Si and polymer microelectrodes resembling the Michigan electrode geometry [82]. This paper first showed that Si shank microelectrodes, rigidly tethered to the skull, transfer significant strain to the surrounding brain tissue from a radial or tangential force applied at the top of the cortex and result in tip displacement. They also showed that tissue adhesion will act to decrease the resulting tip displacement for a given force.

Sabbaroyan et al. performed similar modeling of a Si Michigan microelectrode array in comparison with a polyimide array of the same dimensions [83]. Their results showed a 65%-94% decrease in strain at the electrode tip due to force in the tangential direction

with a polyimide electrode. No change was seen in the resulting stress between a Si and polyimide microelectrode for a tethering force in the radial direction–along the long axis of the probe.

Therefore, using conventional tethering techniques, the resulting strain seen by the neural tissue is dependent on the flexibility of the implanted shank. Most histological studies described in Section 2.4 use Si shank microelectrode arrays and found persistent microglial activation. Biran et al. used Si shank microelectrode arrays as well and noted a pronounced difference between ones that were conventionally secured to the skull or broken off and left free floating in the brain tissue; the floating one produced significantly less microglial response [79]. Kim et al. showed similar results with flexible, polymer hollow fibers that were either fixated to the skull or left to float in the brain tissue [80]. Their results showed an even greater decrease in microglial response in the free-floating cases than [79]. Thus, a flexible substrate design that minimizes tethering forces on the implanted microelectrode array is supported.

2.5 Implications

Designing an intracortical microelectrode array capable of long-term *in vivo* recording requires an interdisciplinary view. The necessary biology and electrophysiology must be known in order to determine the relative size and shape of the electrode array as well as the best measurement procedure. In order to have sufficient spatial resolution, the electrode sites must be comparable to the size of the neural cell body. Hughes et al. and Lempka et al. suggest that recording site areas should be around 400 μm^2 for optimal signal-to-noise ratio [84, 85]. Measuring and amplifying the extracellular voltage with respect to a reference electrode located within the cerebral spinal fluid, but not in the cortex, insures that action potentials from neurons within 200 μm of the implanted microelectrode will be measured.

By reviewing the numerous microelectrode array designs, advantages and disadvantages are apparent for the different design schemes. Out of the pros and

cons listed in Section 2.3.5, some of the most important points used in the design of the UF microelectrode array are as follows. Microwire arrays that do not use microfabrication techniques and are discretely assembled are not easily compatible with the integration of electronics for a fully-implantable system. Platforms for electronics that reside on the cortex, as in the Utah array, have power constraints because of tissue heating. Moreover, catastrophic failure may be induced by the fracture of brittle materials used in the the implanted microelectrode. This work presents a microelectrode design that incorporates robust materials that will not break and can be integrated with application-specific-integrated circuits (ASICs) in a way that minimizes the amount of space needed for integration and places the electronics away from the cortex on top of the skull.

Knowledge of the immune response and how it is affected by material composition, size, mechanical properties, and implant construct is most important for long-term efficacy of the device. Based on the papers reviewed in Section 2.4, the size and shape of the microelectrode array has most impact on the initial wound response rather than the chronic foreign body response. Thus, the size of the microelectrode array should be minimized to reduce the magnitude of the initial wound. However, the factors controlling the severity of the chronic immune response and the resulting decrease in recording performance are not yet fully known and thus, are difficult to design around. A microelectrode with minimal tethering to the skull made out of softer, more flexible materials is suggested to lessen the chronic would healing response by the research in the field so far. However, the goal of this work is to exemplify the functionality of the Florida Wireless Integrated Recording Electrode (FWIRE) design, which uses well-established, tungsten microwire electrodes that are integrated with a micromachined polymer-based substrate. The UF microelectrode array capitalizes on a design that maximizes the functionality with integrated electronics while allowing future changes to the implanted microelectrodes to be made.

Furthermore, this work fully characterizes the electrochemical interaction at the interface of the tungsten electrode and extracellular fluid. Corrosion of the tungsten electrodes has been overlooked by researchers in the field thus far. This work provides information on the corrosion of tungsten in biological solutions that has not been reported and suggests that tungsten should not be used for long-term recording applications. The next chapter presents the background necessary to understand the electrochemical nature of the electrode interface.

CHAPTER 3
ELECTRODE-ELECTROLYTE INTERFACE PHYSICS AND CONCERNS

The use of metal as an implant material is most widely known for dental and orthopedic applications. In these cases, metal is primarily used for structural purposes. Corrosion of the metal implants for orthopedic applications is an ongoing issue [86]. Cardiac pace makers are one example of a medical device that use metal electrodes for electrical signal conduction into the cardiac muscle. A large body of literature is available on the corrosion analysis of metals and metal oxides for stimulation purposes [87–90]. Neural interface prosthetics also use metal for the electrical conduction of signals at the tissue interface. Less information on the corrosion properties of metals is available for neural recording applications. To understand how corrosion may occur, the physics explaining the nature of charge transfer at a metal-tissue, or electrode-electrolyte, interface are presented in this chapter. Also, the current understanding of the corrosion properties of tungsten (the metal of numerous intracortical microelectrodes) is discussed, showing gaps in the knowledge base for biological applications.

3.1 Electrode-Electrolyte Interface

Consider the electrochemical nature of the electrode-electrolyte interface. The interface has a distinct physical structure that governs ionic current flow. Two cases are explored that have the absence or presence of electrochemical reactions at the electrode interface, namely, nonfaradaic and faradaic.

3.1.1 The Nonfaradaic Interface

No electrochemical reactions occur at the nonfaradaic interface. An electrode exhibiting this feature is often called a blocking electrode when no current flows at DC conditions [36]. It is shown next that passage of current is effectively capacitively coupled at the interface. This phenomenon is described by the double layer theory.

When an unbiased metal electrode is immersed in an electrolytic solution, a space charge region will form at the interface [91]. Physically, this is a redistribution of charge

at the interface that arises from anisotropic forces acting on ions in solution due to a change in boundary conditions [91]. Thermodynamically, the space charge region can be explained by the difference in electrochemical potential, μ, of the metal and electrolyte. The equation for the electrochemical potential for one species is

$$\mu = \mu_0 + zF\phi, \tag{3–1}$$

where μ_0 is the chemical work and $zF\phi$ is the electrical work required to bring one mole with charge z form infinity to the material phase, where F is Faraday's constant and ϕ is potentail [91].

The space charge region in metal and solution interfaces was first described by Helmholtz and is known generically as the double layer [91]. He postulated that a fixed layer of ionic charge would be attracted to the interface due to the difference in electrochemical potential at equilibrium. His theory however, could not explain all experimental results [91]. Thus, subsequent interface models have arisen giving a more complete picture.

The following presents the Stern model of the double layer, which is a combination of the Helmholtz-Perrin and Gouy-Chapman models. As Figure 3-1 shows, the interface has an inner and outer Helmholtz plane (IHP and OHP, respectively). The inner plane consists of adsorbed ions or molecules such as polarized water molecules; the outer plane consists of solvated ions (normally cations) that are the opposite sign of the excess charge on the metal [91]. There is a finite distance d between the centers of the ions or molecules at the IHP and the solvated ions in the OHP. This layer constitutes a fixed layer of charge, and therefore a fixed capacitance that does not change with applied potential, as Helmholtz first postulated.

The next layer in the Stern double layer model is the diffuse layer. Based on a double layer theory proposed independently by Guoy and Champman, Stern concluded that adjacent to the layer of fixed charge at the OHP, there is a space in which charge

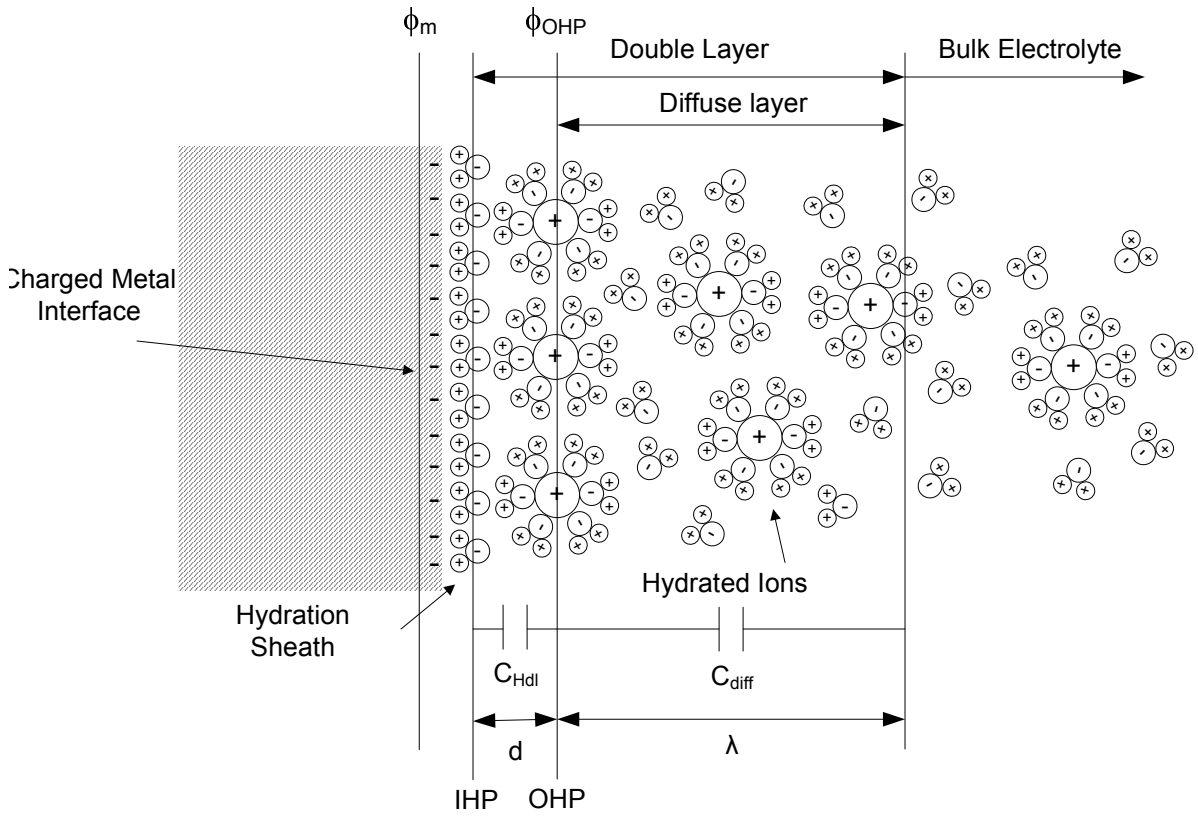

Figure 3-1. Equilibrium electrode/electrolyte interface.

is distributed. The net charge in this area exponentially decays to zero as a function of distance [91]. The charge on the electrode surface will equal the charge in the Helmholtz double layer plus the charge in the diffuse layer, $q_m = q_{IHP} + q_{diff}(x)$. If using the relation,

$$\frac{\partial \Phi}{\partial x} = \frac{q}{\epsilon}, \tag{3–2}$$

where ϵ is permittivity [91], it can be seen that the two layers constitute two potential drops

$$\Phi_m - \Phi_{ref} = \Phi_m - \Phi_{OHP} + \Phi_{OHP} - \Phi_{ref}, \tag{3–3}$$

where the drop in the Helmholtz double layer is linear and exponentially decaying in the diffuse layer [91]. The definition for capacitance is

$$C = \frac{\partial q}{\partial \Phi}, \tag{3–4}$$

where q is the charge on the electrode [91]. Therefore,

$$\frac{1}{C_{dl}} = \frac{1}{C_{Hdl}} + \frac{1}{C_{diff}}, \tag{3–5}$$

where the double layer capacitance C_{dl} is equal to the series combination of the Helmholtz double layer capacitance C_{Hdl} and the diffuse layer capacitance C_{diff}. The capacitance values are given by

$$C_{Hdl} = \frac{A\epsilon}{d} \tag{3–6}$$

and

$$C_{diff} = A\frac{\epsilon}{\lambda}\cosh\frac{zF\Phi_{OHP}}{2RT}, \tag{3–7}$$

where A is the electrode area, λ is the Debye length, z is the charge number of species i, F is Faraday's constant, R is the universal gas constant, and T is temperature [91], [36]. The diffuse layer capacitance given above is only valid for an electrolyte having one cationic species and one anionic species with the same charge number.

In practice, the total double layer capacitance is dominated by the Helmholtz double layer capacitance. In sufficiently concentrated solutions, C_{diff} becomes much larger than C_{Hdl}, and therefore has negligible influence on C_{dl} [91]. The double layer capacity is typically $10 - 20\ F/cm^2$ [92]. Since it has been shown that current is capacitively coupled in the double layer, the current to voltage relationship in the bulk electrolyte is considered next.

As stated in Section 2.2, the neural signal is recorded via two electrodes in the tissue. One is in close proximity to the neuron, and the other is sufficiently far away so as not to measure the same signal. The potential difference measured across the two electrodes then equals the voltage dropped across the electrolyte plus the voltage dropped across the double layer of the electrodes as

$$Vm = IR_e + V_{dl}, \tag{3–8}$$

where R_e is the electrolyte resistance. R_e, then, is the other circuit element that physically describes the equivalent impedance of the electrode-electrolyte interface.

The following discussion will outline the derivation for an analytical equation describing the electrolyte resistance of a disk electrode. Flux of ionic species is given by

$$\mathbf{N}_i = -z_i u_i F c_i \nabla \Phi - D_i \nabla c_i + \mathbf{v} c_i, \tag{3–9}$$

where u_i is the mobility, c_i is the concentration, D_i is the diffusion coefficient, and $\mathbf{v}$ is velocity of species i [36]. The terms relate the flow of ions to migration, diffusion, and convection, consecutively. The corresponding current density can be given as

$$\mathbf{i} = F \sum_i z_i \mathbf{N}_i. \tag{3–10}$$

Following the law of electroneutrality in the bulk electrolyte, the convection term is zero, and assuming there is no concentration gradient, (3–10) yields

$$\mathbf{i} = -\kappa \nabla \Phi, \tag{3–11}$$

where the conductivity of the electrolyte is

$$\kappa = F^2 \sum_i z_i^2 u_i C_i. \tag{3–12}$$

The potential Φ in the electroneutral-bulk electrolyte satisfies Laplace's equation [36]

$$\nabla^2 \Phi = 0. \tag{3–13}$$

The equivalent resistive term in the bulk electrolyte is then found by solving the Laplace equation, with boundary conditions as given by (3–10) [36]. For a disk electrode with a reference electrode a semi-infinite distance away, the resistance of the bulk electrolyte is given as

$$R_e = \frac{1}{4\kappa r_0}, \tag{3–14}$$

where r_0 is the radius of the disk electrode.

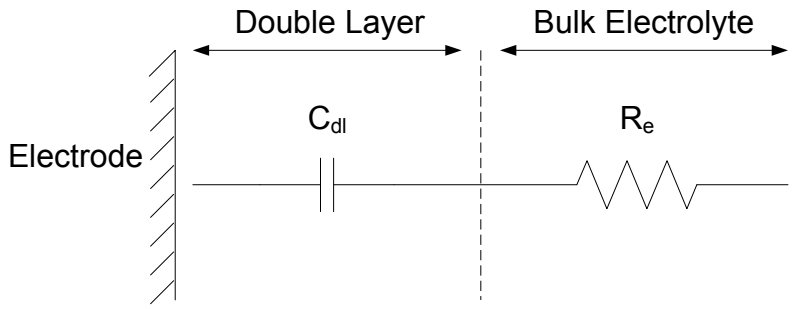

Figure 3-2. Equivalent circuit for the nonfaradaic interface [1].

Thus, the impedance of the electrode-electrolyte interface may be modeled as given in Figure 3-2 in absence of electrochemical reactions (i.e. nonfaradaic interface) [1].

3.1.2 The Faradaic Interface

Unlike the previous case, electrochemical reactions take place at the electrode surface in the faradaic interface. Current flow in the double layer region may occur via double layer charging or electrochemical charge transfer [91]. The physics established thus far, describing the double layer and bulk regions for the nonfaradaic case, also hold true for the faradaic interface. The only new development addressed in this section is the faradaic charge transfer mechanism at the interface.

In the faradaic interface, chemical reactions are thermodynamically favorable under equilibrium and nonequilibrium conditions [36]. This statement means that when the electrode is immersed in the electrolyte, reduction and oxidation reactions automatically occur at the electrode surface. The current density produced by one reversible redox reaction, $O + ze^- \leftrightarrows R$, is given by the Butler-Volmer equation

$$i = i_0 \exp\left(\frac{\alpha_a F}{RT}\eta\right) - exp\left(-\frac{\alpha_c F}{RT}\eta\right), \tag{3–15}$$

where i_0 is the exchange current density, η is the applied voltage, or overpotential, and $\alpha_{a,c}$ are the transfer coefficients for the anodic and cathodic reactions, respectively [36]. This equation shows that the total net current will be the difference of the anodic and cathodic currents. At electrical equilibrium, or zero overpotential, the rate of oxidation

equals the rate of reduction and no net current is produced. However, anodic and cathodic currents exist and equal the exchange current density, $i_0 = i_a = i_c$.

Electrochemical reactions allow charge to be transferred from the electrolyte to the metal and visa versa. The equation for current determines the rate at which this happens relative to an overpotential. Thus, the resistance to charge transfer given in Ωcm^2 is defined by [93]

$$R_c t = \frac{\partial \eta}{\partial i}. \tag{3–16}$$

The Bulter-Volmer current is a nonlinear function; however, at small overpotentials, it may be considered linear. If $\alpha_c = (1 - \alpha_a)$, (3–15) can be written as [93]

$$i = i_0(\eta F/RT). \tag{3–17}$$

Therefore, $R_c t$ is given by

$$R_c t = \frac{RT}{i_0 F}. \tag{3–18}$$

This resistive term is placed in parallel with the double layer capacitance in the equivalent circuit model as shown in Figure 3-3 [1].

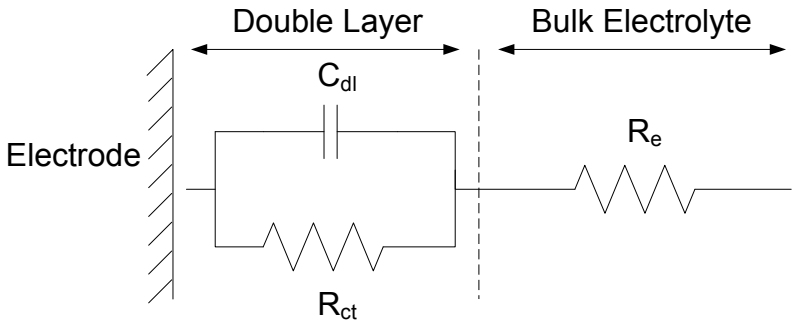

Figure 3-3. Equivalent circuit for faradaic interface [1].

The electrochemical theory discussed so far is valid for one reversible reaction at the electrode-electrolyte interface. The effect of multiple or mixed reactions is given next. The graph in Figure 3-4 shows the voltage versus log current density relationship for two arbitrary redox reactions [51]. In this scenario, the quasi-equilibrium potential and current density for these reactions are where the lines cross for the two reactions. Thus,

oxidation of species N is occurring on the anode and reduction of species M is occurring on the cathode. This non-reversible reaction could represent a corroding system, if the metal is being oxidized into its ionic form [51]. The potential and current density at which the anodic reaction rate equals the cathodic reaction rate are called the corrosion potential, E_{corr}, and corrosion current density, i_{corr}. Notice the difference between the exchange current density for a single reaction i_0.

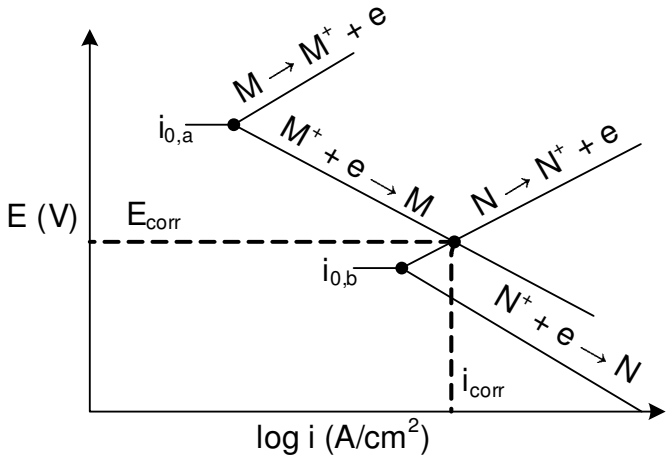

Figure 3-4. I-V relationship of two reactions occurring at the interface.

Similar to (3–15), the current density at an interface with mixed reactions is

$$i = i_a \exp\left(\frac{2.303\eta}{\beta_a}\right) - i_c \exp\left(-\frac{2.303\eta}{\beta_c}\right), \tag{3–19}$$

where $\beta_{a,c} = \frac{RT}{\alpha_{a,c}F}$ is the Tafel slope [51]. For small overpotentials, (3–19) is linearized and the polarization resistance becomes

$$R_p = i_{corr}\frac{\beta_a\beta_c,}{2.303(\beta_a + \beta_c)}, \tag{3–20}$$

where $i_{corr} = i_a = -i_c$ [51].

3.1.3 Interface Summary

Section 3.1 considered two simple and ideal cases; the blocking and faradaic electrode-electrolyte interface. In the blocking case, the electrode is capacitively coupled by the double layer capacitance and allows alternating current to flow with no

change to the electrode or surrounding tissue. In the faradaic case, both direct and time-varying current may flow via double layer charging and electrochemical reactions. If the reactions are not reversible, then the electrode could be corroding and chemical species could be entering into the tissue. There are other phenomena that could also take place, including mass transfer limitation by diffusion[93]. However, the phenomena described previously are sufficient for characterization of the electrode-electrolyte interfaces seen in this work.

3.2 Need for Electrochemical Analysis of Electrode Materials

Tungsten is commonly used for recording sites on intracortical microelectrode arrays. Commercial microelectrode arrays as well as many noncommercial arrays from various research groups, including the authors', are made with tungsten microwires [11, 15, 23, 27, 39]. Tungsten electrodes formed from 50 μm diameter microwires are desirable for intracortical applications because of their strength and rigidity. The microwires can be inserted into neural tissue without buckling. However, tungsten is not impervious to corrosion. A failure mechanism for microelectronic integrated circuits has been shown to be the corrosion of tungsten via-plugs [94]. Tungsten coils, due to their thrombogenicity, had been used clinically to occlude unwanted vasculature and have since been taken off the market due to degradation of the coils [95]. Sanchez et al. showed structural modification of tungsten microwires after four weeks of *in vivo* implantation [96]. Their observation suggested corrosion had occurred at the end of the tungsten microwires.

Although the corrosion and anodic dissolution of tungsten are well documented for acids [97–100] and bases [99–101] at various potentials, the rate and electrochemical mechanism of tungsten corrosion in biological solutions are not well documented. In a comprehensive study, Anik et al. showed that the dissolution of tungsten depends on specific system conditions such as potential and pH [99]. One study used similar conditions seen by tungsten microwires in neural recording applications. Peuster et

al. performed an *in vitro* assessment of the corrosion of tungsten coils in Ringer's solution, a type of physiological saline solution, via weight loss measurements and concluded that one coil would dissolve in 6 years [95]. Their analysis however, did not specify a corrosion rate in units of mass per area per time and thus is not useful to estimate corrosion in other systems. Therefore, a study that quantifies the corrosion rate for tungsten microelectrodes used in intracortical recording applications is needed. Moreover, the electrochemical behavior of tungsten microelectrodes should be compared to the behavior of platinum microelectrodes, which are also widely used for neural recording applications and considered inert for such applications [102–104].

It would be prudent to know if the inflammatory response also affects charge transfer at the microelectrodes, since Biran et al. concluded that the presence of microelectrodes in neural tissue elicits a chronic inflammatory response that may lead to the injury of nearby neurons [74]. Reactive oxygen species such as H_2O_2 are produced by the reactive microglia during the inflammatory response [75]. Two studies investigated the influence of H_2O_2 on titanium used for structural implants in the body (i.e. hip implants), [105, 106]. They showed that millimolar concentrations of H_2O_2 modified the natural oxide layer on the titanium resulting in decreased corrosion resistance. To our knowledge, there are no studies that analyze the electrochemical response of tungsten in biofluids containing H_2O_2. Since hydrogen peroxide is an oxidizing agent, it would be beneficial to assess the reactivity of tungsten in electrolytes containing physiological saline and H_2O_2. The reactivity of platinum in electrolytes containing H_2O_2 has been explored [107–110]; however, the potential at which the experiments were done is unrealistic for neural recording applications. Thus, an analysis of the reactivity of platinum in saline electrolytes containing H_2O_2 under the conditions seen in recording applications is also warranted.

The electrochemical analysis of tungsten and platinum electrodes is discussed in Chapter 7. The next two chapters present the design and characterization of the UF microelectrode array.

3.3 Implications

Electrochemical analysis of the metal-electrolyte interface provides insight into the possibility of unfavorable electrochemical reactions occurring on electrodes used in *in vivo* applications. The mechanism of charge transfer may be purely capacitive or include a faradaic pathway. If a faradic pathway contributes to charge transfer for a recording electrode, it would be useful to understand the electrochemical reaction or reactions taking place. Foremost, it would be useful to assess if the electrode will corrode over time, as corrosion would ultimately lead to failure of the device. Secondly, it would be useful to know if the faradaic reaction is adding any unwanted species to the neural tissue if used as an intracortical microelectrode.

The work presented in Chapter 7 aims to increase the knowledge of corrosion of tungsten in electrolytes that model physiological media by specifying a corrosion rate as well as the electrochemical reactions responsible for the corrosion. This work also takes a closer look into the reactivity of platinum in solutions modeling biological media and defines possible reaction mechanisms. In the next chapter, the UF intracortical microelectrode array is presented.

CHAPTER 4
UF RECORDING MICROELECTRODE ARRAY

The UF microelectrode array design leverages the recording properties of conventional microwire electrode arrays with additional features including a flexible micromachined ribbon cable seamlessly integrated to the rigid probes. The goal is to produce electrode arrays that are highly customizable in terms of geometry/layout, have similar recording properties as commercial microelectrode arrays, and are easy to mass fabricate. Characteristics of the UF FWIRE design include the following. The microelectrode array is capable of being inserted in to the neural tissue without buckling, has an array of 8 channels, a standard interface with an 18 pin Omnetics connector, provides strain relief to the back-end connections, and has a substrate that is compatible with the integration of electronics. The chosen approach is to use a flexible polymer substrate and incorporate microwires to the front-end of the device to act as the recording electrode sites. Two generations of microelectrode design are discussed in this chapter. Both generations use micromachining techniques to realize the device. Generation 1 electroplates the microwires, while Generation 2 hybrid packages pre-made microwires to the flexible substrate. Fabrication details, bench-top and acute *in vivo* results of the microelectrode arrays are discussed in sequential order.

4.1 Generation 1

Using conventional micromachining techniques, small-profile metal traces are enclosed between flexible polyimide insulation, making a cable, as seen in Figure 4-1. The electrode probes extend from the cable end 2 mm and include 20 μm $\times$ 50 μm electrode sites on the tips. The electrode area is chosen for sufficient compromise between signal selectivity and noise performance as given by [84]. The corresponding probe dimensions assure adequate structural integrity according to calculation using Euler-Bernoulli beam theory. The metal traces and corresponding bond sites can be made to any size specification and spacing distance via photolithography.

Polyimide, chosen as the cable material for its flexibility and good dielectric properties, is widely used in the medical field as a neural implant material with negligible tissue response [111, 112]. Parylene-C, chosen for the probe insulation material, has also been successfully used as an insulating material on chronically implanted microelectrodes [113–115]. Nickel is chosen as the rigid probe material due to its ability to be electroplated easily. However, Geddes et.al. caution that nickel implants can instigate allergic response in some individuals [116]. Therefore gold is electroplated on the exposed Ni electrode sites to increase its biocompatibility.

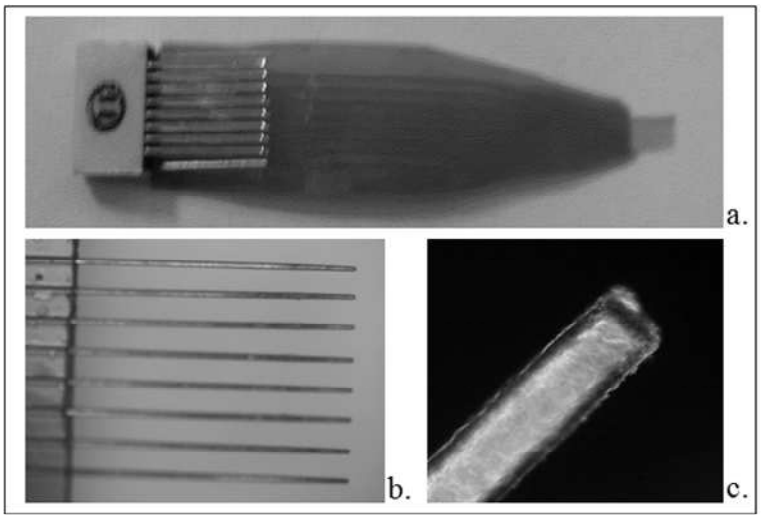

Figure 4-1. Flexible substrate microelectrode array with Omnetics connector. a) Finished device. b) Microelectrode array. c) Probe tip showing insulation along shank and gold plating on tip.

4.1.1 Fabrication

All processing is performed on the surface of a 4 inch silicon wafer covered with Kapton tape (which provides adequate adhesion between the subsequent polyimide layers). The polyimide bottom insulation layer (PI 2611, HD Microsystems) is spin deposited and cured to a final thickness of 20 μm. Sputtered nickel, 100 Å, is patterned to define the probe, wiring, and bond pad dimensions. Then Ni is electrodeposited on the Ni seed to an average thickness of 20 μm via a 10 mA direct current for 4 hours in a nickel sulfamate bath (Nickel S, Technic Inc.). Adhesion promoter (VM9611, HD

Microsystems) is next applied followed by three spin coatings of the PI 2611 to achieve the final 20 μm top layer of insulation. Al (1000 Å) is patterned as a hard mask for the subsequent oxygen plasma etch. The etching process includes an O_2 reactive ion etch (RIE) that removes the polyimide from the top of the bond pads and the probe tips. The remaining polyimide under the probe tips is isotropically etched in a plasma barrel asher. Then the probe-cable assembly is removed from the substrate wafer and primed for parylene-C deposition with a silane adhesion promoter (Acros Organcis). The parylene-C vapor deposition step insulates the shank of the metal probes to a thickness of 2-4 μm. Then the probe ends are manually cut with a blade to expose bare metal for the electrode sites. Finally, the probes are immersed in an electroless gold plating solution (TechniIMGold AT, 600, Technic Inc.) that covers the electrode sites as well as the bond pad sites with 0.1 μm of gold. An Omnetics connector is then fixed to the bond pads with silver epoxy.

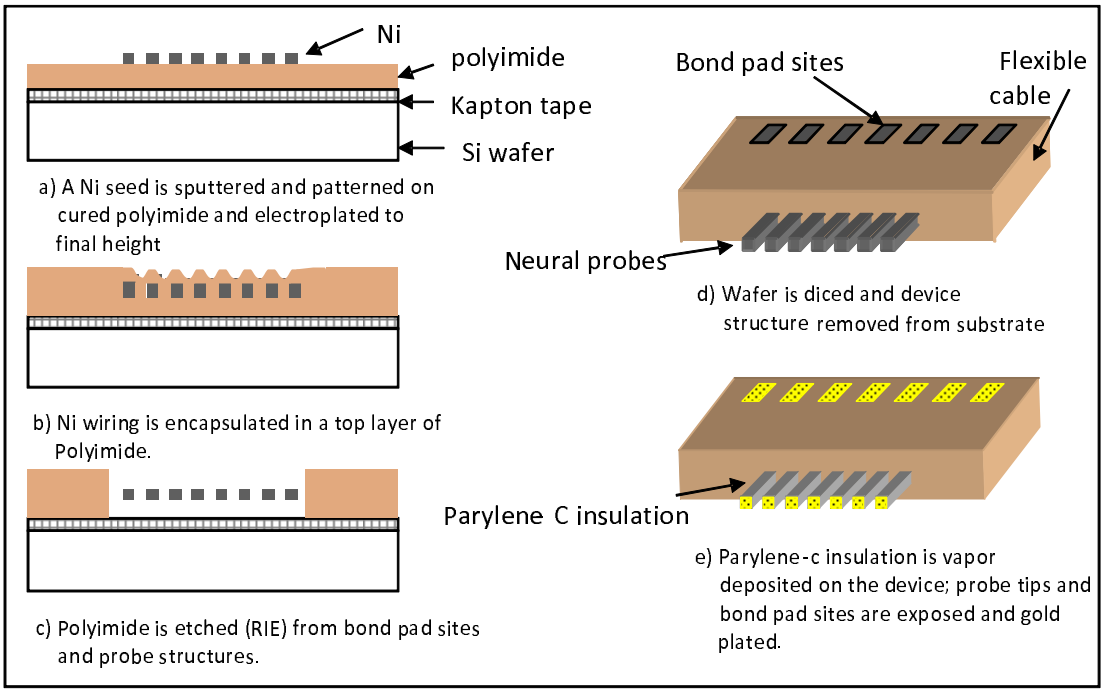

Figure 4-2. Fabrication process flow for generation 1 microelectrode.

4.1.2 Bench-Top Electrical Testing

Benchtop and *in vivo* results are discussed in this section. EIS is used to ascertain the impedance magnitude at the frequency range of interest, as a metric for comparison. The minimum detectable signal is also given via an analytical model of thermal noise.

Electrochemical impedance spectroscopy was performed on one microelectrode array in 0.9% NaCl at room temperature using a Solatron Impedance Analyzer and Galvanostat. A silver/silver chloride reference electrode and platinum counter electrode were used. Measurements were taken over a frequency range of 5 Hz to 10 kHz at open circuit potential with a sinusoidal perturbation voltage of 10 mV. All data shown is consistent with the Kramers-Kronig relation as prescribed by [117]. An impedance of 0.9 MΩ $\pm$ 0.02 MΩ is given for a single probe at 1 kHz.

Regression of the impedance data was performed to obtain an equivalent circuit describing the physical nature of the electrode/electrolyte interface. The most appropriate circuit that physically explains the interface consists of R_e (electrolyte resistance) in series with a parallel combination of R_{ct} (charge transfer resistance), and Z_{CPE} (double layer constant phase element), where $Z_{CPE} = ((j\omega)^{\alpha} Q_{dl})^{-1}$. The regressed parameters are given in Figure 4-3.

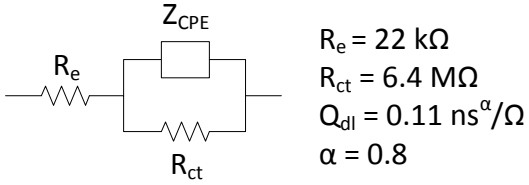

Figure 4-3. Equivalent circuit for electrode/electrolyte interface.

Thermal noise from the real part of the electrode/electrolyte interface impedance is assumed to be the dominant noise source [118]. The resulting noise voltage can be given as follows

$$V_n(rms) = \sqrt{4kT \int_{\omega_{low}}^{\omega_{high}} (R_e + \frac{R_{ct}}{1 + (\omega^{\alpha} Q_{dl} R_{ct})^2}) d\omega} \tag{4–1}$$

where ω_{high} and ω_{low} are the high and low pass-band frequencies of the amplifier [118]. The theoretical rms noise voltage of the designed neural probe is 2 μV based on the regressed equivalent components and frequency range of 100 Hz to 6 kHz.

4.1.3 Implantation

Adult male 250 g Sprague-Dauley rats were used to test the recording performance of the flexible electrode arrays. All procedures have been approved by the University of Florida IACUC Board and were performed in the University of Florida McKnight Brain Institute. Prior to surgery, the rats were anesthetized and the surgical site was thoroughly sterilized. The top of the skull was then exposed by a midsaggital incision from between the eyes and the landmarks bregma and lambda are located on the skull [119]. The microwire array was implanted to a depth of 1.66 mm as shown in Figure 4-4 into the forelimb region of the primary motor cortex. The electrodes are stereotaxically moved to the appropriate site and lowered to the appropriate depth using a micropositioner (1 mm per hour) to minimize distress to the brain tissue (FHC, Bowdowinham, ME). The array was then grounded using a 1/16" diameter stainless steel screw. A low profile Omnetics connector was used to attach the recording wire.

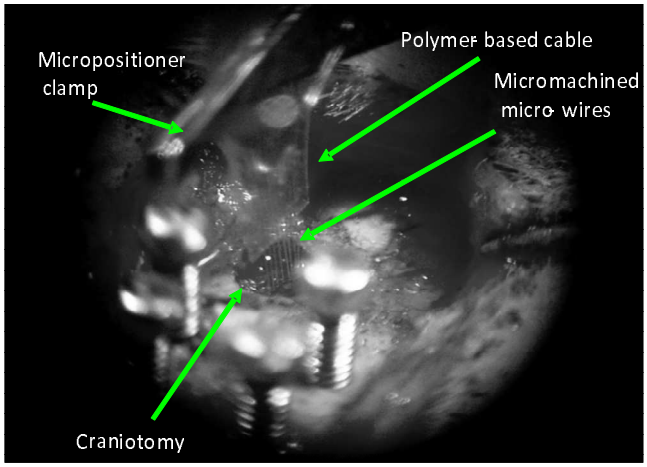

Figure 4-4. Surgical implantation of generation 1 microelectrode.

4.1.4 Surgical Recording

Extra-cellular potentials recorded at 12,207 Hz during surgery were analyzed and spike sorted using Spike2 (CED, U.K.) software package. Recordings were analyzed over a period of 130 s at a cortical depth of 1.66 mm. To detect and sort neural activity within each channel, an automated waveform matching system within Spike2 was used to construct templates using threshold detection.

Once a set of waveform templates was generated for a data stream, all those templates (noise) that did not match characteristic neural depolarization behavior were removed. The remaining waveform templates were sorted according to amplitude and shape, and any waveform templates that were significantly similar to each other were combined into a single template. Clustering of waveform variance within templates was verified through principal component analysis (PCA). Each waveform template was statistically unique and representative of a distinct neuron within the channel. Using these two values, the signal to noise ratio for each neuron template was calculated. To ensure proper reporting, all spike waveform templates that possessed peak to peak amplitude of a magnitude below three times the value of the noise floor were considered too close to the noise to be reliably and consistently distinguished and were removed from the study. Values of neural yield, noise floor, amplitude, and SNR are reported for each channel within Table 4-1.

Action potential amplitudes as large as 115 μV and as small as 13 μV are discriminated by the electrode and recording system. The average noise floor is 4 μV_{rms} for a frequency range of 500 Hz to 6 kHz. Figure 4-5 shows recorded data from electrode number 6.

4.1.5 Summary

A flexible substrate microelectrode array has been designed using microfabrication techniques and tested in vivo. Acute electrophysiological recordings show excellent yield of recordable neurons and signal to noise ratios from 10 bB to 27 dB. The neural probe

Table 4-1. Neuronal Yield for Generation 1 Microelectrode Array

Electrode	1	2	3	4	5	6	7	8
Yield (neurons)	2	2	2	3	6	5	3	4
Noise Floor (μV, rms)	4.1	5.0	5.3	4.4	5.2	3.8	3.7	4.3
Neuron Amplitude (μV , PtP)	20.1	23.3	32.6	26.1	114.7	90.4	31.4	45.1
	13.2	15.5	24.7	18.3	56.8	52.3	13.4	29.7
				14.2	34.6	35.7	11.7	21.0
					21.3	21.0		16.0
					18.8	13.8		
					17.4			
SNR (dB)	13.8	13.4	15.8	15.5	26.9	27.6	18.6	20.4
	10.2	9.9	13.4	12.4	20.8	22.8	11.2	16.8
				10.2	16.5	19.5	10.0	13.8
					12.2	14.8		11.4
					11.2	11.2		
					10.5			

array consists of eight probes with gold-plated electrode sites (1000 μm^2) on the tip that protrude from a flexible cable.

Due to failure in the back-end Omnetics connection, *in vivo* recordings were unable to be performed after the surgery. However, the electrode array was left implanted in the rat's brain for a remaining 2 weeks. It then was removed and images were taken. Remarkably, the electroplated metal of the electrode was recessed within the parylene-c insulation as seen in Figure 4-6 by approximately 20 μm showing corrosion which could lead to ultimate failure. Thus, nickel as well as the nickel/gold combination were removed from future designs.

The Achilles's heel of Generation 1 is the need for electroplating of a metal to a thickness of 20 μm or more. It is difficult to find noble metals that can be electroplated and even harder to plate them to such a thickness. Therefore, the process flow has been

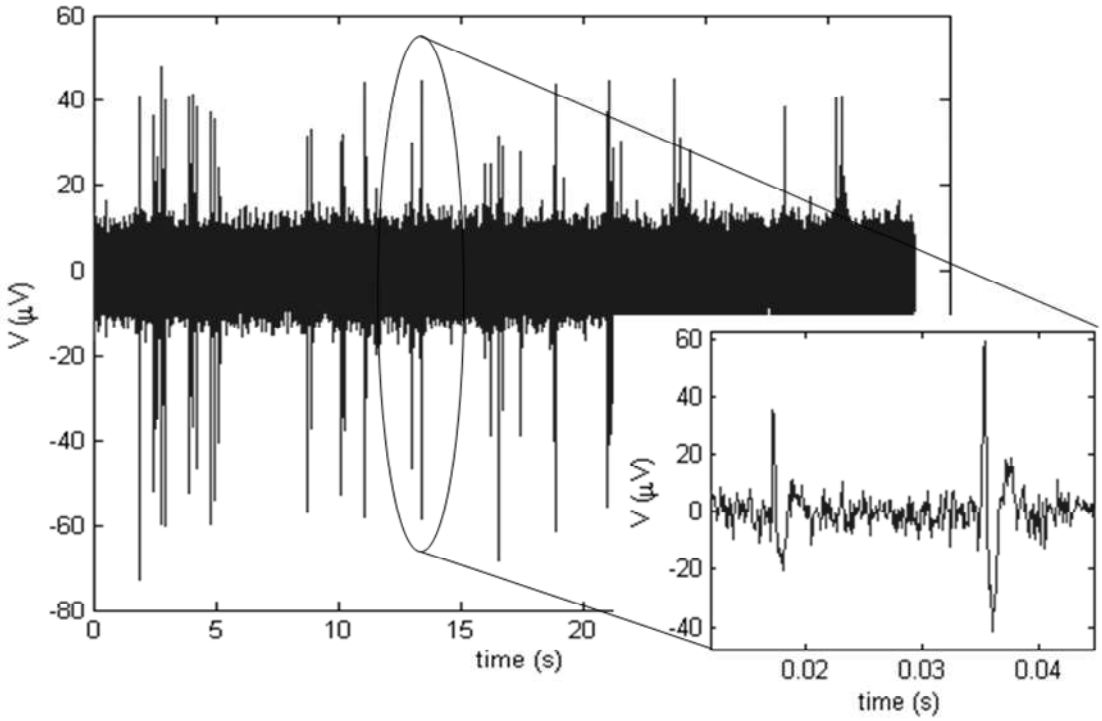

Figure 4-5. Data from neural recording in the rat motor cortex at a depth of 1.66 μm during implantation surgery. Inset shows two distinct neurons recorded by single probe.

changed in Generation 2 to allow the incorporation of a greater number of electrode materials.

4.2 Generation 2

This section will highlight a second generation microelectrode design that incorporates the hybrid packaging of tungsten microwires. Generation 2 is a design closely resembling Generation 1 in form and function. The end goal with this generation of microelectrode arrays is to provide a viable micromachined platform on which a fully implantable wireless system may be incorporated.

Based on the inadequacy of Generation 1, namely corrosion of the electroplated nickel microwire, Generation 2 incorporates pre-fabricated tungsten microwires in the design. Tungsten is chosen since it is used in commercially available microelectrode arrays, which have large use in the neuroscience community. However, as Chapter 7

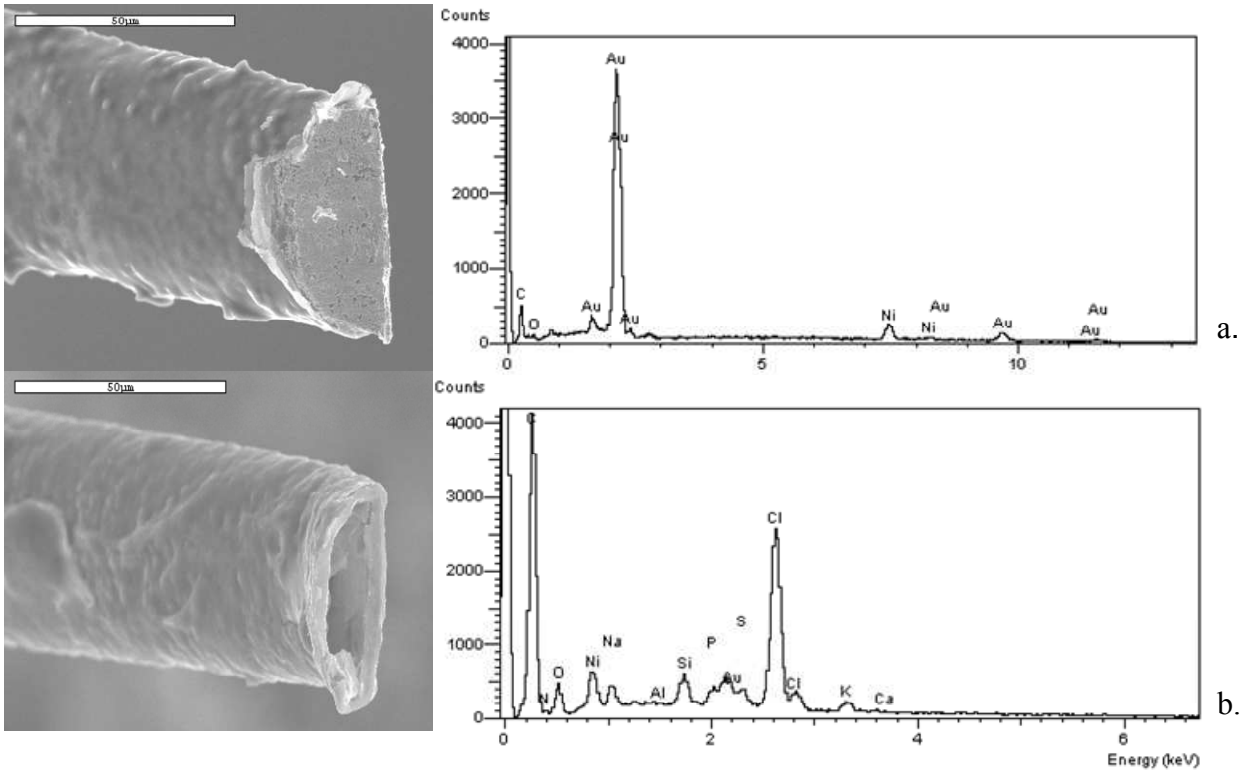

Figure 4-6. Corrosion of Electrode a. SEM and EDS measurement results of typical gold-plated nickel electrode. b. SEM and EDS meaurement results of typical electrode after *in vivo* implantation for two weeks. Notice that metal had been eroded from the surface but parylene-C insulation remains unchanged.

cautions, tungsten also corrodes in biological environments. Fortunately, the established design is applicable to any type of metal wire.

The generation 2 microelectrode array shown in Figure 4-7 consists of three major components: a polymer substrate with encapsulated wiring, tungsten microwires, and nuts used for anchoring and grounding. Rigid 50 μm diameter tungsten micro-wires are attached to the end of a micromachined flexible cable in a 1-D array, allowing for insertion into the neural tissue without buckling. The micro-wires are spaced 250 μm apart as prescribed for decoupled neural recording [34]. Nuts are provided for screws that anchor the device to the skull and supply the reference potential. Incorporating the fasteners yields a secured flat platform for future population of flip-chip bonded electronics. Device dimensions are given in Figure 4-7.

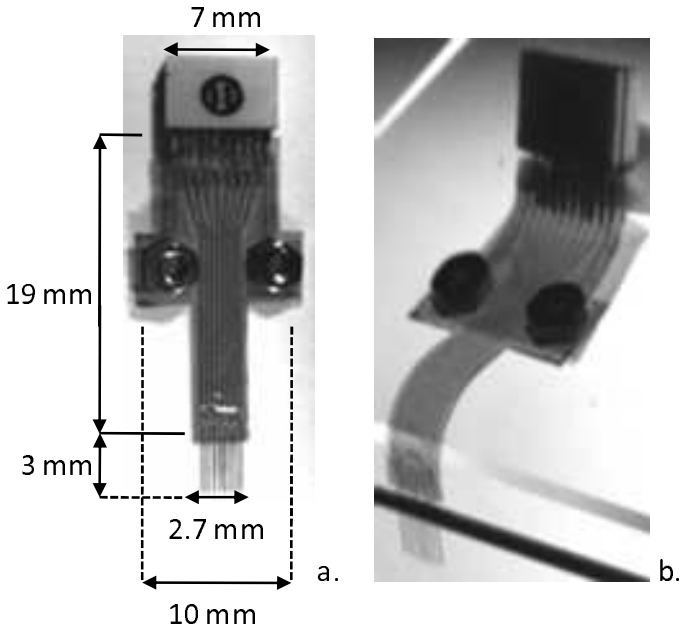

Figure 4-7. Polymer microelectrode array with Omnetics connector. a. Top view. b. Flexibility of microelectrode is shown with assumed *in vivo* position.

4.2.1 Fabrication

The process flow for this electrode was developed based on the process used for the previous generation electrode [26]. Changes were incorporated to improve the quality and reliability of the end product. Aluminum was first sputter deposited on a 4-inch-diameter silicon wafer to a 1 μm thickness as the sacrificial layer. The bottom insulation layer of polyimide (PI 2611, HD Microsystems) was then spin-deposited along with an adhesion promoter (VM 9611, HD Microsystems) and cured at 300°C. After four spins, the resulting thickness was 24 μm. A layer of gold was then sputter deposited to a thickness of 0.1 μm, which was patterned via lift-off to define the wiring and bond pads. Polyimide was next spun five times and cured to achieve a thickness of 30 μm, thereby making the top insulation layer. Chromium was sputter deposited to a thickness of 1000 Å and patterned as a hard mask via lift-off. Then an O_2 reactive ion etch (RIE) was performed to define the device footprint, uncover bondpads and etch grooves for guided placement of the micro-wires. Fifty μm diameter tungsten wires insulated with polyimide (California Fine Wire) were then placed manually in the etched

grooves that formed a jig and electrically connected to the gold wiring of the substrate using a conductive silver epoxy (Epotech). A dicing saw was used to cut the secured micro-wires at a specified length and established a consistent, planar surface for all recording sites. The microelectrode array was then released from the wafer by removing the sacrificial aluminum layer using anodic metal dissolution (constant current in 10% NaCl) as described by reference [10]. The attachment sites for the tungsten wires and stainless steel nuts were coated with insulating epoxy (Dualbond 707, Cyberbond) and PDMS (Silicone type A, Dow Corning). Lastly, an Omnetics connector was attached to the array with conductive silver epoxy.

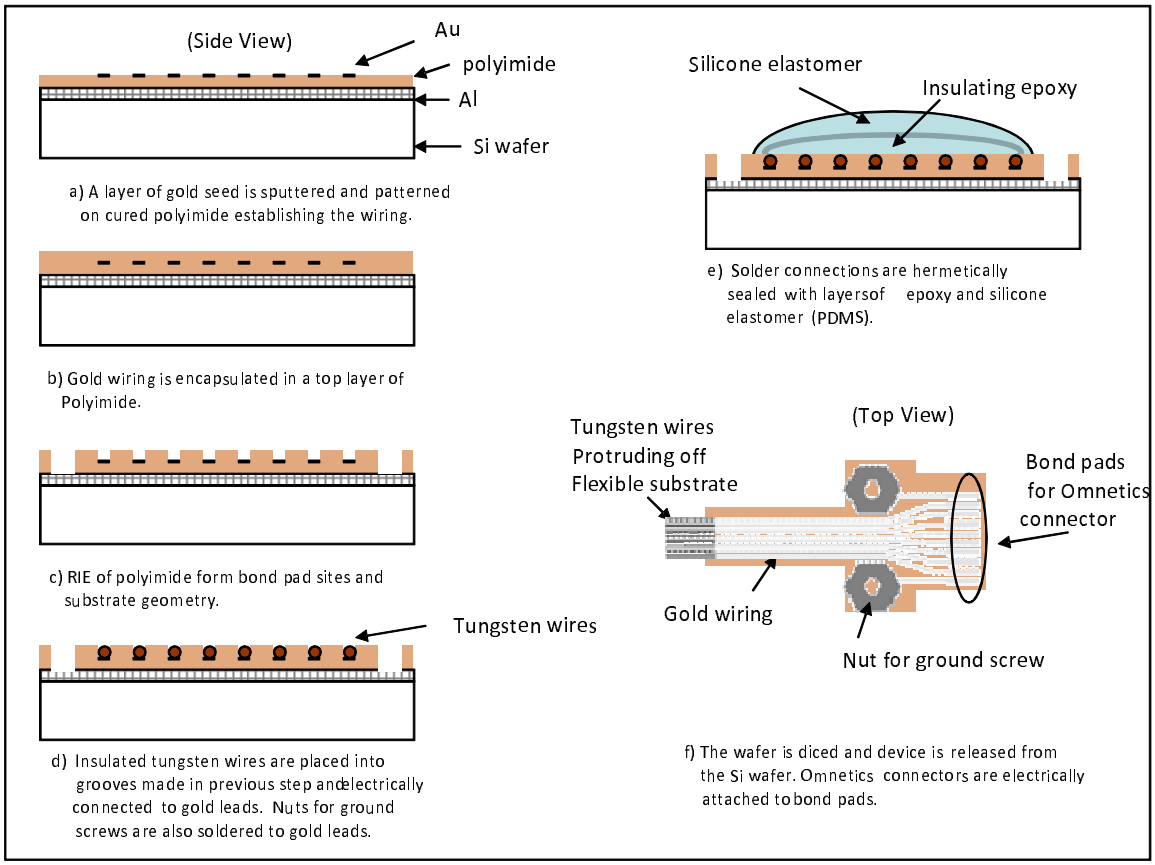

Figure 4-8. Fabrication process of generation 2 microelectrode array.

4.2.2 Bench-Top Electrical Testing

A Gamry potentiostat (Series G 300) was used for electrochemical impedance spectroscopy. Individual tungsten recording sites were measured with respect to a

large surface area platinum counter electrode and Ag/AgCl reference electrode in 0.9% phosphate buffered NaCl (Sigma) at room temperature. The perturbation voltage was 50 mV. All experimental data were consistent with the Kramers-Kronig relation as prescribed by reference [117]. The average impedance at 1 kHz for all recording sites was 50$\pm$ 10 kΩ. This value was characteristic of small surface area electrodes and was on the same order of magnitude as electrodes in the Utah array [50].

Using the equivalent circuit model shown in Figure 4-9 to describe the electrode/electrolyte interface, the impedance data was regressed giving the reported circuit parameters. These parameters were determined using data in the range of 100 Hz to 10 kHz.

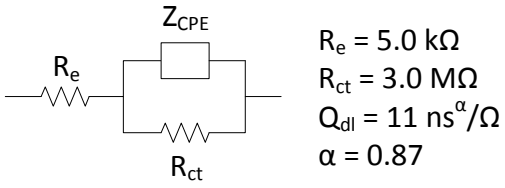

Figure 4-9. Equivalent circuit for electrode/electrolyte interface. R_e is the electrolyte resistance, R_t is the charge transfer resistance and Z_{CPE} is the double layer constant phase element given by $Z_{CPE} = ((j\omega)^{\alpha} Q_{dl})^{-1}$.

Experimental noise data was measured for the tungsten recording sites immersed in phosphate buffered saline at room temperature with reference to an Ag/AgCl electrode at equilibrium. The thermal noise signal from the electrochemical interface was amplified by a low noise voltage amplifier (Stanford Research System (SRS) 560) with gain of 1000 and then recorded with a SRS 785 spectrum analyzer from 1 Hz to 10 kHz. The thermal noise may be calculated from the real part of the electrode/electrolyte interface impedance as follows

$$V_n(rms) = \sqrt{4kT \int_{\omega_{low}}^{\omega_{high}} (R_e + \frac{R_{ct}}{1 + (\omega^{\alpha} Q_{dl} R_{ct})^2}) d\omega} \qquad (4\text{–}2)$$

where ω_{high} and ω_{low} are the high and low pass-band corner frequencies of the recording amplifier, k is Boltzmann's constant, and T is temperature [118]. The theoretical rms noise voltage of the neural probe is 1.27 μV based on the regressed equivalent

components in the frequency range of 100 Hz to 6 kHz. The experimental rms noise voltage determined from the noise data is 1.59 $\pm$ 0.12 μV in the same frequency range.

4.2.3 Implantation

The flexible electrode arrays were implanted into an adult male Sprague-Dawley rat to test the electrode-substrate configuration and recording performance. All animal procedures have been approved by the University of Florida IACUC. The rats were first anesthetized and the surgical site was thoroughly sterilized. The top of the skull was exposed by a mid sagital incision between the eyes, and the landmarks bregma, and lambda were located on the skull. A craniotomy was drilled (+1 mm anterior to bregma, 2.5 mm lateral) at the site corresponding to the forelimb region of the motor cortex [119]. At the site of the electrode implantation, the dura was removed to expose the cortex. The entire assembly was implanted vertically as shown in Fig. 3a and lowered to a depth of 1.66 mm using a micropositioner to minimize distress and damage to the brain tissue. While driving the electrode, electrophysiologic recordings were used to locate pyramidal cell activity in layer V of the cortex. During this procedure, the assembly was observed to be rigid and no buckling was present. Once the electrode was positioned, it was supported with cranioplastic cement (Plastics-1) attached to a screw placed adjacent to the craniotomy. After the array was secured, the entire assembly was folded down to lay flat against the table of the skull as shown in Fig. 3b. The flexible substrate was then permanently grounded using a second screw.

4.2.4 Surgical Recording

Neuronal recordings were obtained using a TDT System 3 Real-time Signal Processing System (Tucker-Davis Technologies, Alachua, FL). The headstage was interfaced to the substrate through an Omnetics 18 pin low-profile connector. Extracellular signals were recorded at a sampling rate of 12,207 Hz (16 bits resolution) and bandpass filtered from 500 Hz to 6000 Hz. Data were recorded, digitized and stored on a personal computer for use in offline analysis.

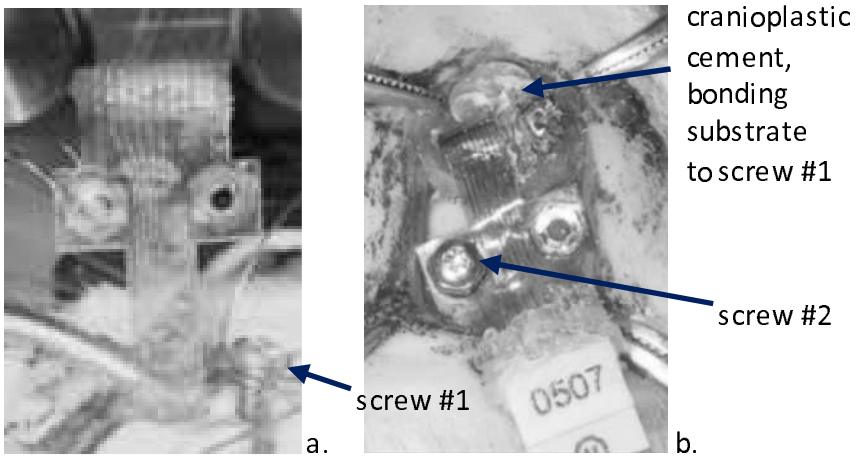

Figure 4-10. *In vivo* testing. a. Vertical implantation without buckling. b. Final placement of microelectrode secured to skull with screw.

Action potentials were discriminated off-line with Spike2 (CED, UK). For each of the eight electrodes, simultaneous recordings lasting 170 seconds were used in the analysis. To detect candidate action potentials, a threshold was applied to the data and a set of templates was formed. Signals with at least a biphasic component within a 1.6 ms window that occurred more than 25 times with similar shape (80%) was categorized as a new neural template. All waveforms that did not match characteristic neural depolarization behavior were considered as noise and removed. The remaining waveforms were sorted according to the amplitude and shape of generated templates, and any waveform templates that were significantly similar to each other were combined into a single template. Principal component analysis (PCA) was used to cluster waveform variance within templates. ISI distribution curves for each neuron in the channels displayed individual Poisson distributions as expected, and showed distinct neurons for each unit waveform.

After the action potential waveforms were properly isolated and sorted, the peak-to-peak amplitude (PPA) was evaluated by computing the average waveform of all spikes belonging to the same neuron. The potential difference was then measured from the apex of the depolarization peak to the apex of the hyperpolarization peak. In

addition to the PPA, the noise floor of each channel was evaluated by computing the root mean square value of all signals excluding recognized neuron waveforms within the channel. The signal-to-noise ratio (SNR) for each neuron was calculated using a ratio of these two values. A representative section of recorded data is shown in Figure 4-11. Here we can qualitatively see three distinct neuron waveforms with a low noise floor.

The overall performance of the electrode is quantified in terms of neuronal yield, noise floor, peak to peak amplitude, and SNR and is reported in Table 4-2. A total of 5 waveforms could be extracted from this 8-channel array. The electrodes and recording system performed to discriminate action potential amplitude as high as 30 μV and as low as 12.8 μV. The average RMS noise floor is 3.3 μV. The "pile plots" of action potentials shown in Figure 4-12 indicate the repeatability of the waveforms.

Table 4-2. Performance of Generation 2 Microelectrode Array

Electrode	1	7
Yield (neurons)	3	2
Noise Floor (μV, rms)	4.1	2.9
Neuron Amplitude (μV, PtP)	303.0 22.3 12.	20.7 14.2
SNR (dB)	17.3 14.7 9.9	17.1 13.8

4.2.5 Summary

A prototype of a flexible substrate tungsten microelectrode array has been developed and tested for the Florida Wireless Implantable Recording Electrode (FWIRE) project. This generation 2 design uses discrete tungsten micro-wires as the electrodes in contact with the brain and a flexible polymer substrate designed to lay flat on the skull which provides a base for future designs incorporating flip-chip bonded electronics. Bench-top experiments give an average impedance of 50 kΩ at 1 kHz and an rms noise

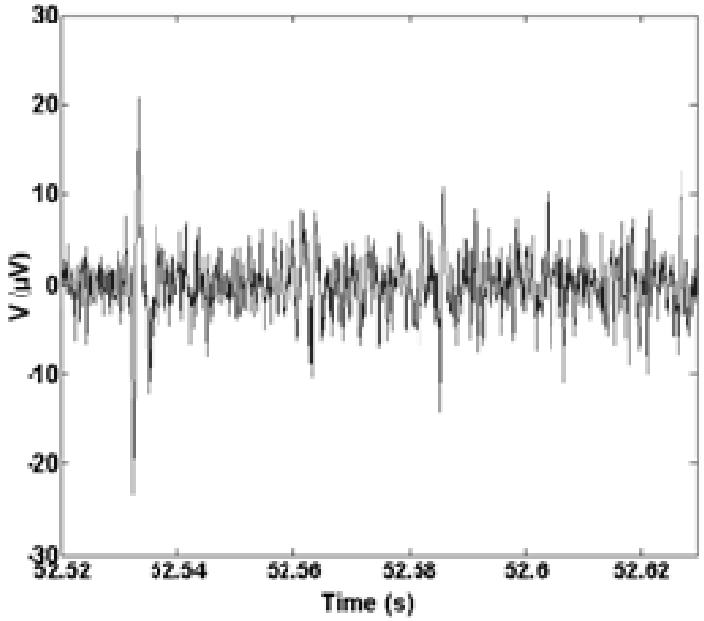

Figure 4-11. Data from neural recording channel number 1 in the rat motor cortex at a depth of $1.66\ \mu m$ during implantation surgery.

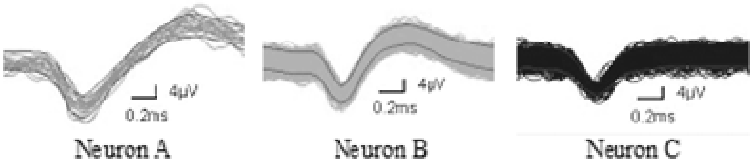

Figure 4-12. Three distinct neurons extracted during spike sorting in channel number 1 of the recorded data.

floor less than 2 μV. Acute recordings show signal to noise ratios as high as 17 dB with a corresponding noise floor of 3.3 μV for two channels showing discernable action potentials. Thus, the minimum detectable signal is limited by the recording electronics. The presented design may be adapted to use more noble micro-wire materials such as platinum or iridium to decrease the risk of surface modification via electrochemical processes with tungsten wires. The hybrid manufacturing approach taken with this design allows the microelectrode array to be implanted accurately and without buckling as the micro-wires provide sufficient structural integrity during insertion.

4.3 UF Microelectrode Summary

Much experience in polyimide micromachining, bench-top electrical characterization, and *in vivo* implantation has been gained through the realization of two generations of microelectrodes described in this chapter. Generation 1 incorporated a process flow using only micromachining steps. However, this required electroplating a metal as thick as 20 μm. Severe corrosion of nickel was seen after two weeks of implantation. Thus, the electroplating step was removed from the next generation as metals suitable for *in vivo* use could not be electroplated that thick. Generation 2 used hybrid-packaging of tungsten micro-wires to a similar polyimide substrate. This generation loses the advantage of bulk processing, as the micro-wires have to be serially hand-assembled. Also, there exists a greater risk of failure due to hybrid-packaged connections. However, successful acute *in vivo* recording results suggest that the microelectrode may be used chronically.

Furthermore, the electrodes, or recording sites, constitute an integral design component. Their biocompatibility and structural reliability establish the crux of a chronically viable device. To date, there are many biocompatibility issues with rigid probes made from microwires or Si substrates as reviewed in Section 2.4. Thus, future BMI recording system designs must be compatible with changes in electrode requirements as more of the biocompatibility problems are solved. The generation 2 UF microelectrode array, being hybrid-packaged, allows incorporation of other microelectrode constructs. This capability provides advantages over the ”Utah” and ”Michigan” electrode, whose Si-based electrode shanks are integral to their design.

CHAPTER 5
UF MICROELECTRODE ARRAY HYBRID-PACKAGED WITH AMPLIFIER IC

For Brain Machine Interfaces to work as therapeutic devices for debilitated individuals, they must provide the necessary function and reliable results for the patient's lifetime. Therefore, strategies to optimize function and reliability determine future recording microelectrode system designs. For a clinically viable solution, the recording system in the BMI must be fully implantable such as cochlear implants and functional electrical stimulation (FES) implants for Parkinson's disease. A fully-implantable structure for BMI applications requires that electronics for amplification, data compression, wireless telemetry, and power systems be incorporated onto the implantable microelectrode substrate.

The challenge of realizing wireless implantable neural recording systems for Brain-Machine Interfaces has been undertaken by a handful of institutions [49, 120–122]. All designs employ hybrid integration with the electronics. The Utah system integrates interface electronics via flip-chip bonding techniques to the top of a Si micromachined 100$\times$100 electrode array implanted into the cortex [120]. The Michigan system uses a silicon flexible cable to rout the signals from the implanted Si micromachined electrodes to a platform containing hybrid-packaged interface electronics located some distance away on the top of the skull [49, 123]. In the time since the Florida Wireless Integrated Recording Electrode (FWIRE) was proposed [122], researchers from Brown University have adopted a design very similar to the UF design, where a flexible polymer cable connects an implantable microelectrode array to the hybrid-packaged interface electronics, which are positioned on the skull [121]. The Brown system employs the silicon-micromachined Utah microelectrode array, while the FWIRE system uses tungsten microwires as the recording electrodes. The FWIRE design further differentiates itself from the other designs by employing a novel pulsed-based data representation scheme, which minimizes transmission bandwidth

and allows spike sorting after transmission [122, 124]. The microelectrode platform discussed in this section is a first step in achieving a recording system with wireless transmitting capability for the FWIRE project. It is similar to generation 2 described previously except it includes a hybrid-packaged amplifier integrated circuit and has a slightly different form factor and anchoring scheme. The design, fabrication, *in vitro* and *in vivo* characterization of the amplifier-microelectrode system is described in this chapter.

5.1 Design

The design considerations for the UF implantable microelectrode array include:

1. a platform with electronics residing on the skull reducing heat transfer to brain tissue,
2. a seamless, flexible connection between implanted electrodes and platform for electronics,
3. a grounding scheme that doubles as an anchoring mechanism, and
4. hybrid-packaging techniques that allow attachment of multiple integrated circuits.

The placement of interface electronics on a platform residing on the skull rather than on top of the cortex allows for less restrictive power constraints on the interface electronics as tissue heating is less of a concern. This design has strategic advantages over the fully-implantable ”Utah” microelectrode array design, which places the electronics on top of the cortex [120]. In this design, the flexible connection between the implanted electrode array and the electronics allows out-of-plane bending such that the electrode array may be implanted perpendicularly to the electronics platform and planar micromachining techniques may be used for the fabrication of the device. The flexible connection also prevents the transfer of strain to the implanted electrodes from movement of the electronics platform. The connection is made seamless by using the same substrate for the entire device. This design ensures a minimum number of connection points that would require hermetic sealing and a relatively simple fabrication

process as compared to the ”Michigan” design that uses a flexible cable to connect its electrodes and interface electronics [45, 123]. A grounding scheme that doubles as an anchoring mechanism, to our knowledge, is not used in any of the existing designs. Since all recorded signals are typically referenced to a bone screw, this design minimizes the space needed for the implant by making the reference, or ground, screw the same as an anchoring screw. Lastly, a flip-chip bonding technique is used to hybrid-package ASICs to the substrate. Flip-chip bonding rather than wire-bonding die or soldering packaged ICs minimizes the total space needed for the chips as well as keeps the total height of the implanted platform to a minimum. This strategy provides advantages over the Brown university design, which uses wire-bonding techniques to attach the ASICs. The guiding principle of the UF design is the use of a relatively simple process flow utilizing tungsten microwires that have been used *in vivo* previously with high neuronal yield in a robust and customizable manufacturing process.

System Layout: To test the neural recording system prototype with the constraints listed above, it is implemented in a rodent-animal model. The system consists of a) electrodes that can either be inline or offset from the substrate, b) patterned wire traces in cable form connecting the electrode to the integrated electronics, c) an integrated amplifier, and d) an integrated ground bolt as shown in Figure 5-1. Until the wireless component of this design is completed, we offer access to the amplifier via a standard Omnetics 18 pin connector. This will eventually be replaced in the final design.

The animal model is a Sprague-Dawley rat as depicted in Figure 5-1. The electrodes must be implanted into a craniotomy (+1 mm anterior to bregma, 2.5 mm lateral) at the site corresponding to the forelimb region of the motor cortex [119]. As seen from the figure, the region of space available for the flexible platform to rest on the skull is essentially the space between the Bregma and the Lambda. Also, it should be noted that the area behind the Lambda point comprises sensitive sinus tissue, and hence it is not advisable to secure the substrate beyond the Lambda point. Moreover,

the average width of the space between Bregma and Lambda is close to 15 mm. The layout of the design was changed from generation 1 such that the device can be implanted inline with the central axis of the rat skull as shown in Figure 5-1. In order to accommodate the entire device inside the available design space (i.e. between Bregma and Lambda), care was taken while deciding the dimensions of the substrate. The length of the platform is 19 mm excluding the tungsten wire length, and the width is 10 mm. Nearly one-third of the substrate will be bent over the Bregma point, thus reducing the overall length of the flat surface well within the limits. Figure 5-2 shows the photograph of the microelectrode array and the flexible platform carrying the amplifier chip. The enlarged inset shows the array of 8 tungsten microwires. Figure 5-3 shows the photograph depicting the flexibility offered by the electrode substrate. This positioning scheme would be followed after *in-vivo* placement.

The electrode sites were shifted left of the midline of the device for implantation in the appropriate area of the motor cortex. A slot for a second screw is also added in this design, allowing less critical placement by the surgeon. Also a perpendicularly mounted Omnetics connector is used in this design scheme.

The implantation of the electrode is performed with the help of a stereotaxic placement system. The electrode substrate is held vertically at its rear tip and driven slowly into the already drilled craniotomy. Keeping this procedure in mind, the entire package is designed with a relatively rigid back end that enables an easy implantation using the stereotaxic placement system.

5.2 Fabrication

Fabrication of the flexible electrode substrate was carried out using a process scheme analogous to our previous electrode generation. The critical steps of the fabrication process are shown in Figure 5-4. A 100 mm diameter Si wafer was used as a supporting platform for all the subsequent processing steps. First, a 1 μm thick aluminum sacrificial layer was sputter deposited. Polyimide was spin-deposited

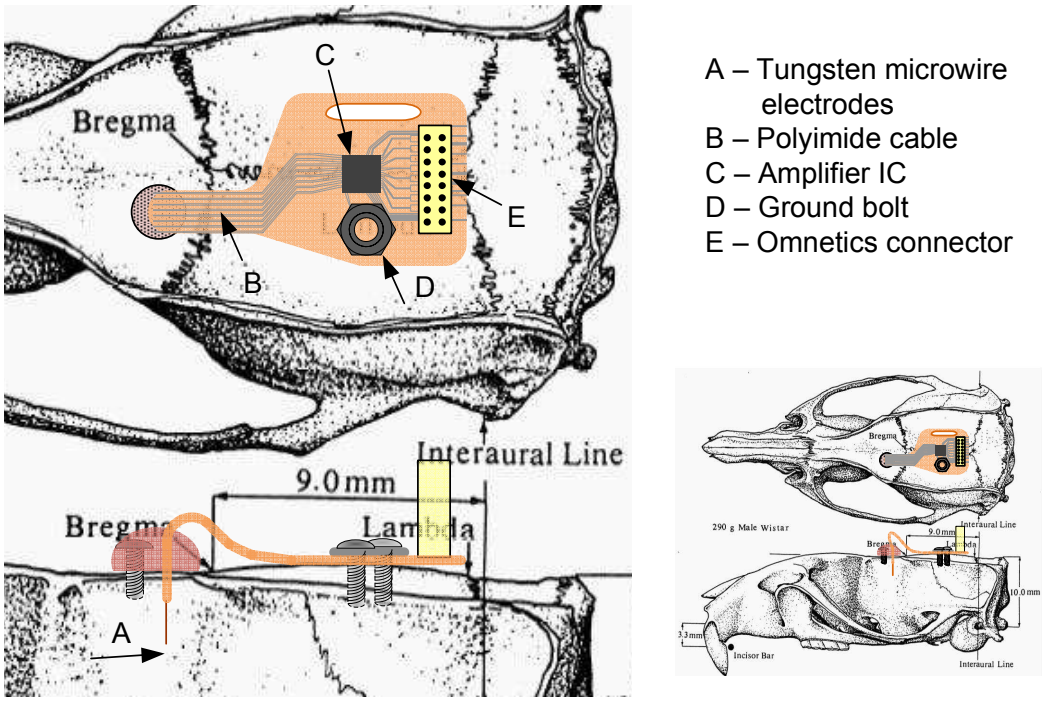

Figure 5-1. *In vivo* placement of microelectrode array on rodent skull. Inset shows full view.

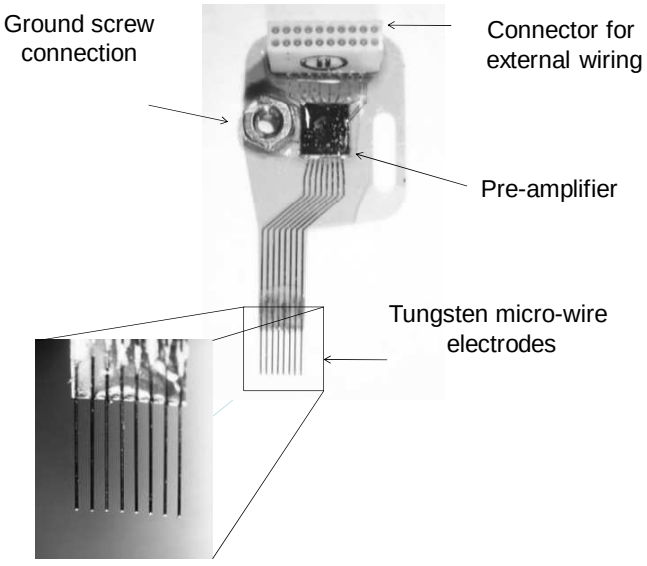

Figure 5-2. Flexible polyimide microelectrode array with integrated amplifier. Inset shows the enlarged image of the tungsten microwires.

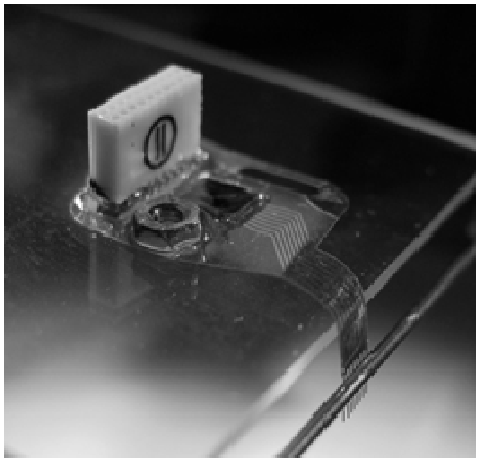

Figure 5-3. UF amplifier-microelectrode system showing the flexibility of the electrode substrate and the final implant position.

and cured as in Section 4-8 and a titanuim/gold layer was sputter deposited to a thickness of 0.01 μm and 0.2 μm, respectively. The deposited metal was patterned as shown in Figure 5-4 for the electrical interconnects and a top layer of polyimide was spin-deposited and cured. Each layer of polyimide has a thickness around 20 μm. The top polyimide layer was selectively etched anisotropically using a Reactive Ion Etcher to uncover amplifier and Omnetics bond pads and to establish the device outline. Insulated tungsten wires of 50 μm diameter were manually placed onto the gold traces and electrically connected with a conductive silver epoxy (AbleBond epoxy). The devices were separated from one another by cutting the wafer with a dicing saw. Each individual device was released from the Si wafer by anodic dissolution of the Al sacrificial layer.

The amplifier die was then bonded to the flexible substrate via a flip-chip bonding process. To enable an effective electrical contact to the pads of the amplifier die, gold stud bumps of 50-70 μm diameter were placed on the die bond pads through a wire bonding process. A photograph of the chip with stud bumps is shown in Figure 5-5 The amplifier bond pad vias on the flexible substrate were then manually filled with a conductive silver epoxy (Ablebond). They had dimensions of 150 μm by 150 μm to accommodate the IC pads of area 130 μm by 130 μm. The distance between

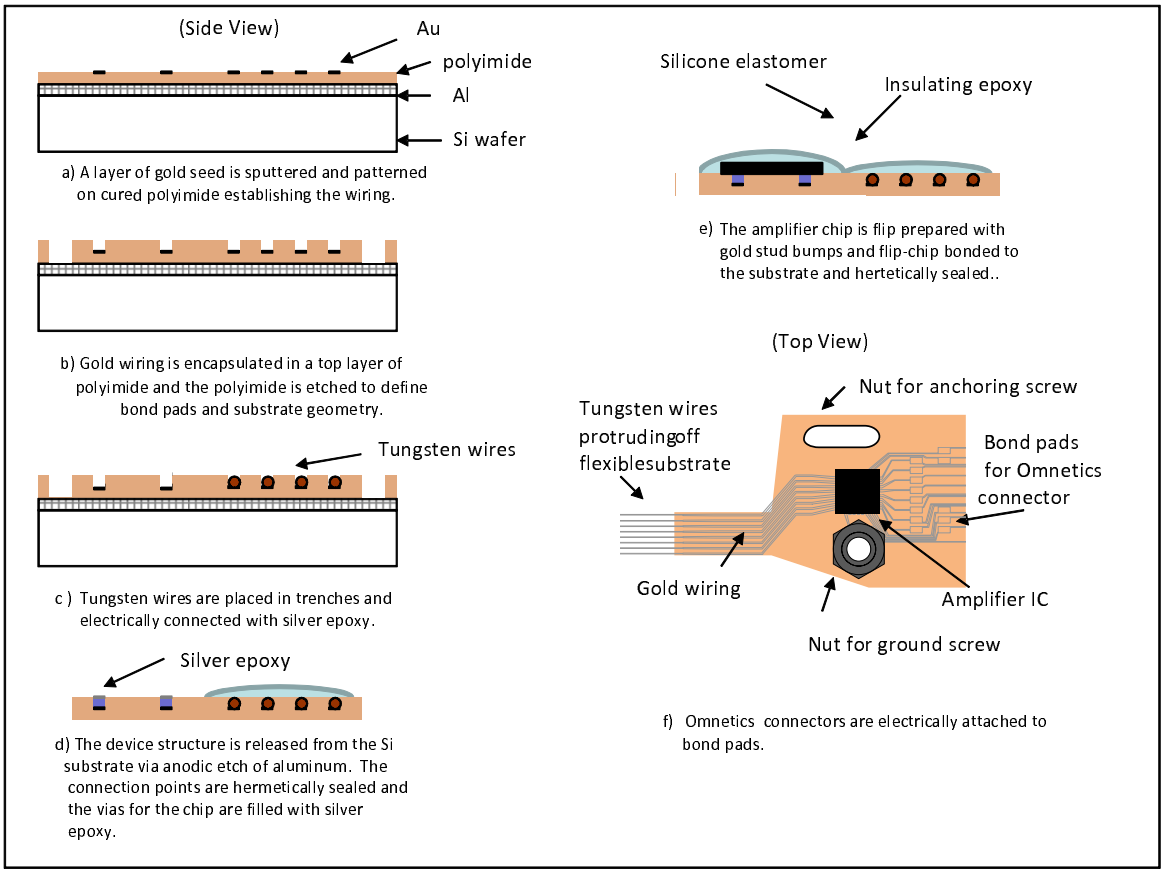

Figure 5-4. Fabrication process flow for UF amplifier-microelectrode system.

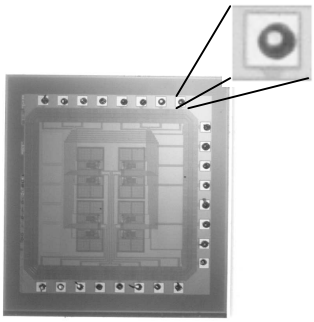

Figure 5-5. Amplifier die with gold stud bumps on bondpads.

two adjacent contact pads was 120 μm. A flip-chip placement system (Model 850, Semiconductor Equipment Corp.) was used to place the die on the substrate. A furnace was used to cure the silver epoxy after placement and then, the amplifier die was coated with a low-moisture-absorbing-underfill epoxy (Epo-tek 302-3M) to hermetically seal

the bond pads. Also, a vertical mountable Omnetics connector was attached to the substrate with a conductive epoxy and supported by underfill epoxy.

5.3 Power System for Amplifier-Microelectrode System

External hardware is needed to provide power for the amplifier IC hybrid-packaged to the UF flexible-substrate microelectrode array and for transmitting the measured neural signals. This section describes the hardware and interface connections to the Tucker Davis recording system. Figure 5-6 shows the circuit boards housed in a shielded box. The circuit board on the right labeled ”power board” regulates voltages from a 6 V battery power supply that are sent to the amplifier and provides wired pass-through connections for the measured neural signals. The buffer board on the left consists of 8 amplifiers that buffer the 8 channel neural signals and provide low impedance inputs to the RA8GA amplifier. The voltages regulated for the amplifier are given in Table 5-1. The voltages V_{dd} and Ac_{gnd} are controlled by fixed voltage regulator ICs, while V_{bias} and V_{buffer} are controlled by potentiometers and are tunable. The input/output connections on the box are illustrated in Figure 5-7. The input connections are defined as the connections going to the implanted array and the output connections are going to a Tucker Davis Technologies (TDT) amplifier. A commutator with DB25 connector attaches to the power box, then a head stage with an 18 pin Omnetics connection on one end attaches to the commutator. The male Omnetics connector on the head stage connects to a female Omnetics connector on the microelectrode array. These connections deliver power to the UF amplifier and transfer the measured eight channels of neural signals to the TDT signal processor. Also, a BNC connector provides an external port to the system ground, which is used for bench-top calibration. The output connection on the other side of the power box is a DB25 connector that attaches via a cable to the TDT RA8GA amplifier.

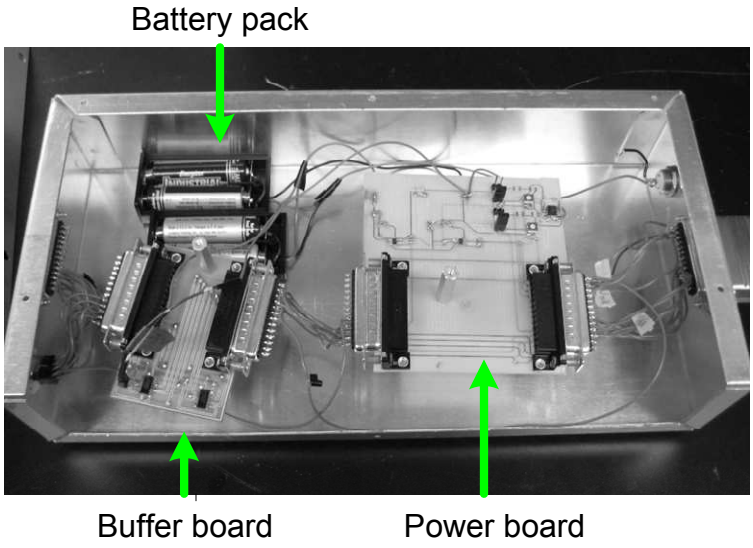

Figure 5-6. Contents of power box.

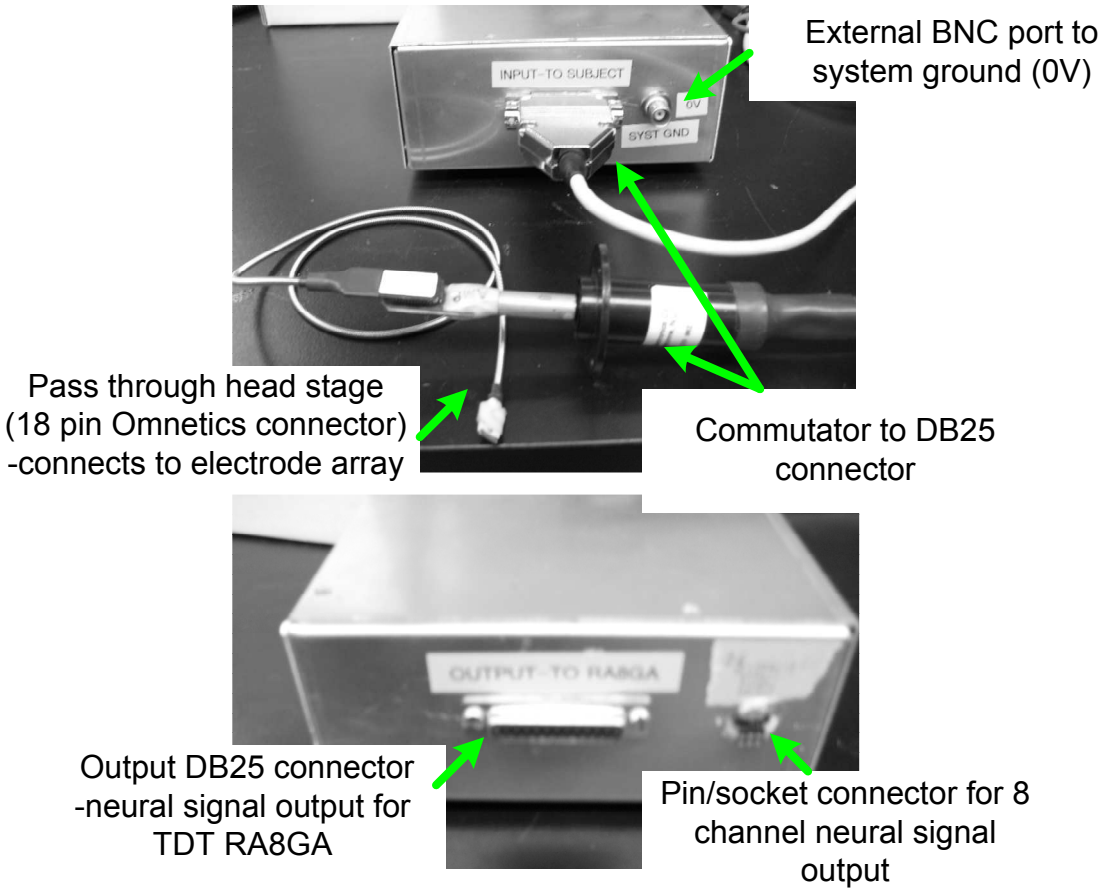

Figure 5-7. Input/output connections for power box.

Table 5-1. Voltage Specifications for UF Amplifier

	Voltages to power UF amp (V)
V_{dd}	5
V_{ss}	0
Ac_{gnd}	2.5
V_{bias}	2.6
V_{buffer}	1.5

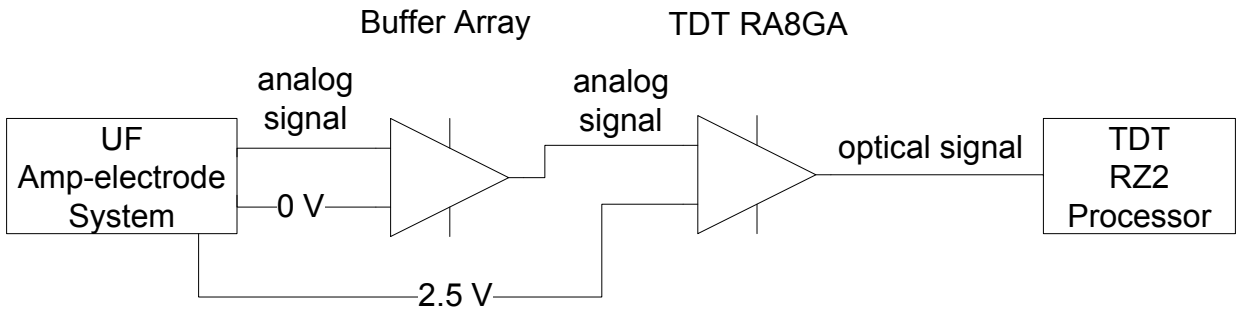

Figure 5-8. Experimental setup with TDT recording system.

5.4 Experimental Setup with TDT Recording System

This section explains how the UF amplifier-electrode system interfaces with the Tucker Davis Technologies (TDT) recording system and discusses specifications regarding noise. A schematic of the system integration is given in Figure 5-8. The UF amplifier-electrode system interfaces first with a buffer amplifier array then a TDT variable gain amplifier (RA8GA) and then the TDT RZ2 signal processor. The TDT RA8GA must be used after the UF amplifier-microelectrode system in order to interface with the RZ2 signal processor that requires optical signals. The RA8GA amplifier has three input settings: 0.1V, 1V and 10V. They amplify the incoming signal by 10, 1, and 0.1, respectively and can accommodate signals no greater than 0.1 mV, 1 V and 10 V, respectively. The manufacturer specified scaling factors that the output voltage must be multiplied by to get the correct output voltage are 10, 170, and 1700, respectively. The input impedance of the RA8GA is on the order of 10 kΩ [39], which poses attenuation issues with the UF system, whose output impedance is relatively high. A buffer amplifier

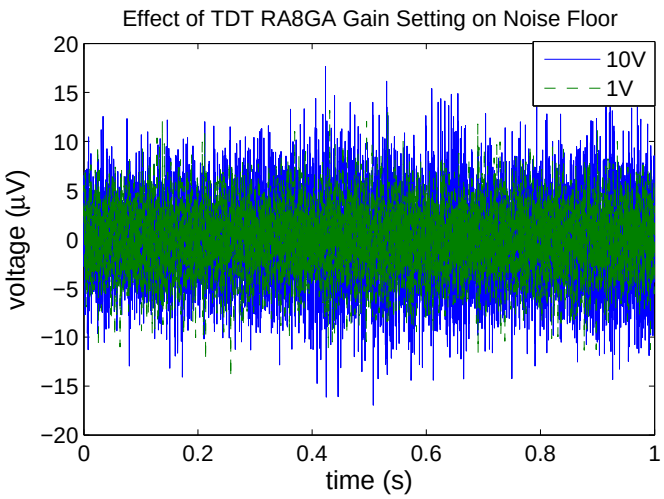

Figure 5-9. Time series noise floor affected by RA8GA preamplifier input setting.

is used after the UF amplifier-electrode system to ensure a low impedance input to the RA8GA.

Choosing the correct input setting on the RA8GA to use is integral to system performance. The output signal of the UF amplifier-microelectrode system has a dc component at 2.5 V and and an ac component anywhere from tens of mV to hundreds of mV. Since the RA8GA cannot AC couple the input signal, the differential signal given as the input is the output from the UF referenced to 2.5 V rather than the system ground of 0 V. Because the dc output of the UF system is not exactly 2.5 V, the resulting signal going into the RA8GA is usually greater than 100 mV so the 0.1V input setting can not be used. If used, the input signal saturates the amplifier and a voltage of 0 is seen on the TDT viewing program. The 1V or 10V input settings can be used; however, the 10 V input setting adds more noise to the system as shown in Figure 5-9. Thus the 1V input setting is always used for the neural recording episodes.

To show that the UF amplifier-electrode system measures the neural signals as effectively as the Tucker Davis electrodes, the noise floor was measured for each system and is compared in this section. The recording setup shown in Figure 5-8 was used to measure time series noise voltages of the UF electrode and a PZ2 preamplifier and

RZ2 recording system were used to measure time series noise for the TDT electrode. The top plot in Figure 5-10 compares the input referred noise floors of two different UF amplifier-electrode systems (UF1 and UF2) with the noise floor of the TDT electrode. They are very similar. (The scaling factor for the UF system is 170/90 with the 1V input setting.) Therefore, it has been shown that the UF amplifier-electrode system can measure neural signals of the same magnitude as the TDT electrode system. The bottom plot in Figure 5-10 shows the output referred noise voltages measured and recorded by the UF electrode and the TDT RZ2 processor. There is no built-in scaling factor in the recording software, thus the output voltage must be multiplied by 170 (scale factor of the RA8GA 1V input setting) and divided by the gain the of the UF amplifier (90) to get the correct input referred noise voltage.

5.5 Bench-Top Characterization

The effect of poor grounding and electromagnetic interference on the noise floor of the system are examined in this section. The analysis of signal degradation due to voltage division at the amplifier and reduced common mode rejection from impedance mismatching between recording electrode and reference is provided. Lessons learned for future integration with electronics are also given.

5.5.1 Effect of Grounding Reference Input to Amplifier

This section explores the effect of grounding the reference input of the differential amplifier on the noise floor of the system. Figure 5-11 shows a schematic of a hypothetical one channel amplifier and the connections if the reference input is floating or connected to system ground. *In vivo*, the differential signal given to the amplifier is always the voltage seen between a tungsten wire implanted into the cortex and a stainless steel screw, which is lodged in the skull of the rat with the bottom in contact with the cerebral spinal fluid that resides on top of the brain. The difference is that in the floating case, the reference is not connected to system ground, which is 0 V referenced to the battery ground; and in the grounded case it is.

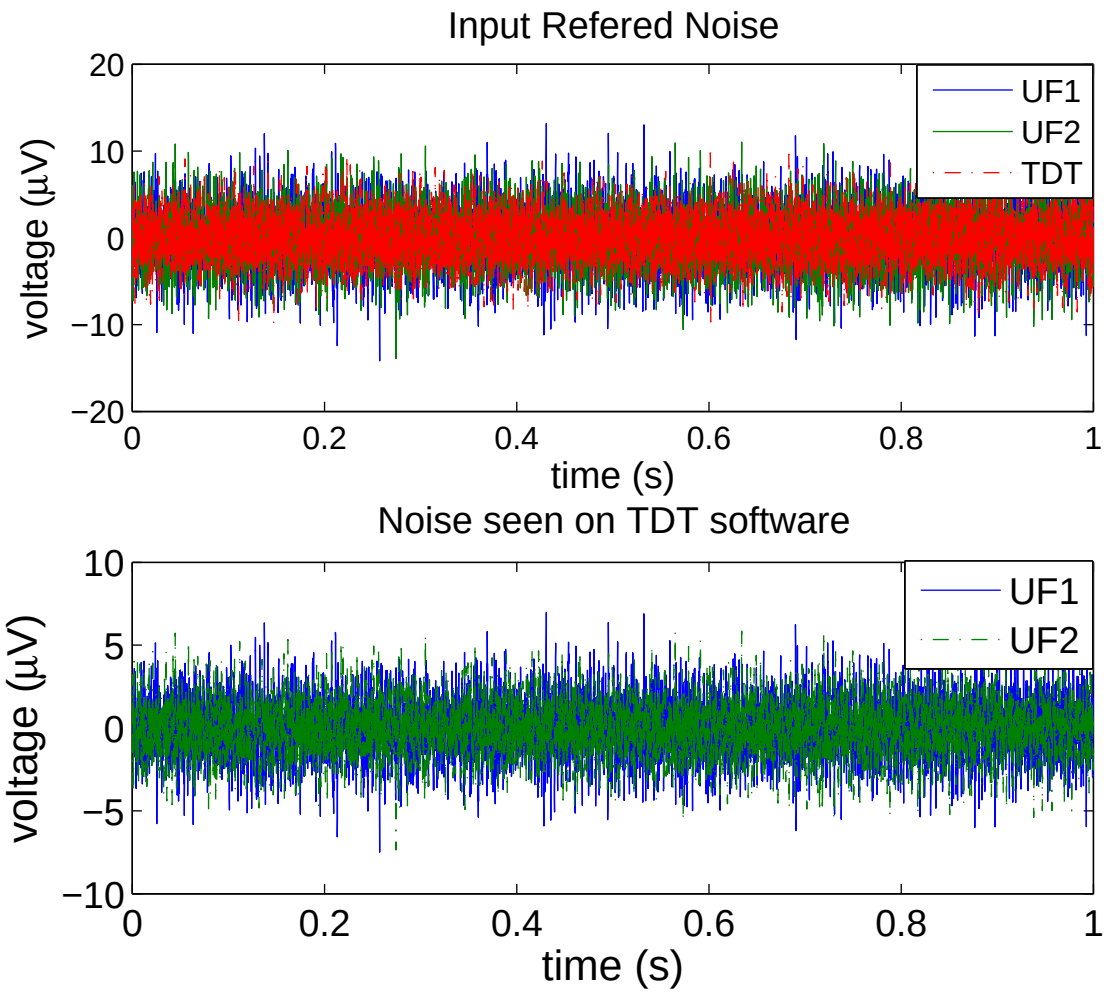

Figure 5-10. Time series noise floor seen on the TDT viewing program. The top plot is the input referred noise scaled by the gain of the amplifier and the scaling factor of the RA8GA (1V input setting). The bottom plot shows the unscaled output referred noise voltage seen by the TDT recording program.

To understand why grounding makes a difference, a closer look is taken at how the microelectrode is implanted and how the reference is connected to the brain fluid. During implantation, the microelectrode array is secured to a stereotaxic apparatus and driven into the brain tissue. The reference connection, which is the nut on the microelectrode substrate, is attached to a temporary screw already secured to the skull with a 1 ft long alligator clip. After the array is implanted to the final depth, it is bent over to rest on the skull and a screw is fit into the reference nut, eliminating the alligator clip,

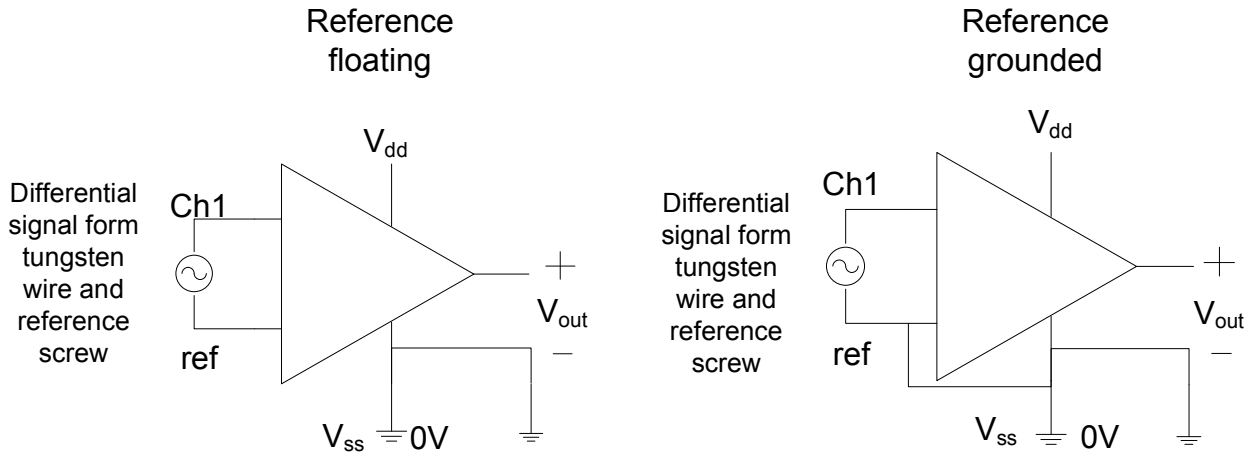

Figure 5-11. Amplifier connections showing floating vs. grounded reference configuration.

and thus making the distance from the nut on the substrate to the brain fluid very short (a few centimeters) compared to the previous case.

Results from noise measurements show that the amount of noise pick-up in the system is greatly affected by the length of the connection from the reference input of the amplifier (i.e. nut on the substrate), to the brain of the rat in a ungrounded setup. Figure 5-12 shows the square root of the noise power spectral density of the amplifier-electrode system when the reference is grounded and floating with different lengths of reference-brain connections. In the grounded case, the amount of noise is the same regardless of the length of the reference-brain connection. In the ungrounded case, the noise measured with the short connection (length of the screw) is very similar to the grounded cases; however, the noise measured with the long reference-brain connection (1 ft alligator clip) is much greater and unacceptable for neural recording. Thus to avoid coupling noise to the system, the reference input should always be grounded to the ground of the amplifier. In these experiments, a beaker of saline was used to model the brain fluid, the noise voltages are input referred, and a SRS 785 spectrum analyzer was used to measure the power spectral density of the noise.

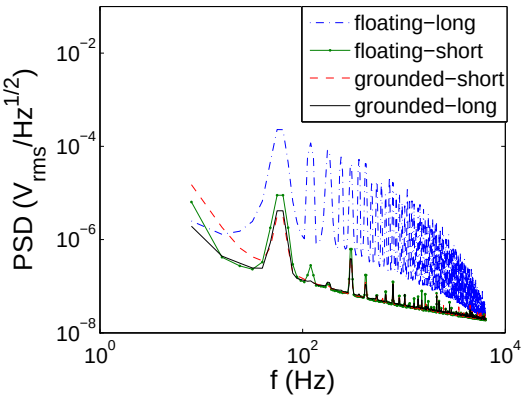

Figure 5-12. Square root of the power spectral density of the amplifier-microelectrode system showing effect of the reference connection on the noise floor.

5.5.2 Effect of EMI on Noise Floor

The last section showed the necessity of grounding the reference input; this section shows the extent of electromagnetic interference (EMI) to a properly grounded system. The noise floor was measured for the amplifier-microelectrode array inside and outside of a Faraday cage. The experimental setup was similar to the last case in that a beaker of 0.9% saline was used to model the brain fluid and both the reference (screw attached to the nut) and channel inputs (tungsten wires) were immersed in it. Figure 5-13 shows the power spectral density of the noise for three channels on the array inside the Faraday cage and outside the Faraday cage. The noise measured inside the Faraday cage is a combination of the thermal noise of the electrode-saline interface and thermal and electronic noise of the amplifier, only. Very little EMI is measured. The noise measured outside the Faraday cage is greatly affected by EMI as the 60 Hz power frequency and its harmonics are seen. Since a Faraday cage cannot be implemented in the *in vivo* setting with the rat, EMI will always be present in the recordings. Table 5-2 shows the extent that the EMI has on the recorded noise floor. Using the frequency range of 500 Hz to 6 kHz, which is what is used when recording with the TDT system, the noise floor is not increased significantly. However, wider bandwidth recordings result

in a larger noise floor. This effect needs to be kept in mind for future generations of UF microelectrode systems.

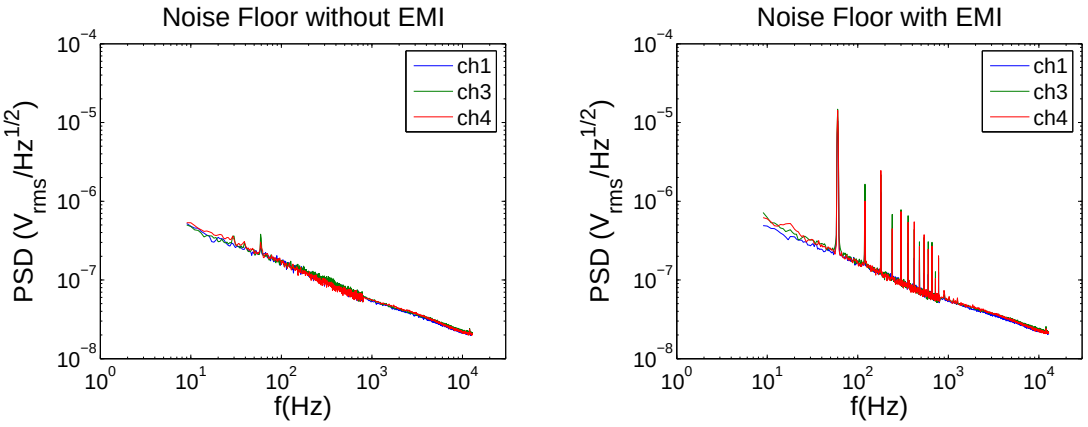

Figure 5-13. Square root of the power spectral density of three channels on the amplifier-microelectrode system showing how electromagnetic interference (EMI) of the 60 Hz power line can affect noise floor (input referred). For the case with no EMI, the microelectrode array was placed inside a double Faraday cage.

Table 5-2. Noise floor

Electrode Channel	Noise Floor without EMI (μV_{rms})		Noise Floor with EMI (μV_{rms})	
	10 Hz-12.8 kHz	500 Hz-12.8k Hz	10 Hz-12.8 kHz	500 Hz-12.8kHz
1	4.73	3.46	13.8	3.52
3	4.90	3.50	19.2	3.72
4	4.87	3.56	18.5	3.69

5.5.3 Impedance Concerns with On-Chip Amplifier

Differential signal attenuation and common mode signal propagation are dependent on the relative magnitudes of impedances corresponding to the recording electrode, reference electrode, and input to the amplifier. Since the input impedance of the recording amplifier is finite, an attenuation of the differential signal due to voltage division at the input is possible. Moreover, Legatt and Stecker caution that common-mode rejection may be compromised by mismatch of the recording and reference electrode impedances [118, 125]. Legatt claims that amplification of common-mode signals

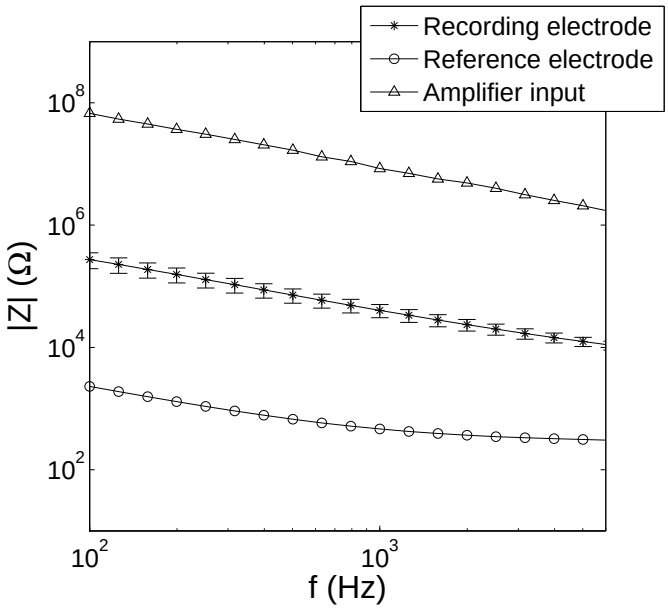

Figure 5-14. Comparison of recording electrode, reference electrode and amplifier input impedances. Error bars on recording electrode correspond to the sample standard deviation of 8 channels on the array.

contributes to much of the output noise seen with EEG systems. The impedance values for the recording electrode, reference electrode, and the input to the amplifier are given in Figure 5-14. Impedance for the amplifier was measured by the Agilent 4294A impedance analyzer. Impedance values for the recording and reference electrodes were measured by a Gamry 300 potentiostat and frequency response analyzer.

The following derivation, taken from Legatt et al. [125], gives analytical equations for the voltage at the output of a differential amplifier. Scenarios relating the magnitude of the impedance of the recording electrode to the reference electrode and input of the amplifier are derived. Figure 5-15 shows a block diagram of common mode, V_c, and differential, V_d, input signals interfacing with impedances of the recording and reference electrode and the differential amplifier, where Z_e is the impedance of the recording electrode, Z_{ref} is the impedance of the reference electrode, Z_{amp} is the input impedance of the amplifier, V_a and V_b are nodal voltages, and V_0 is the output signal. V_d is the signal of interest and is the neural voltage waveform in this case. The output voltage can

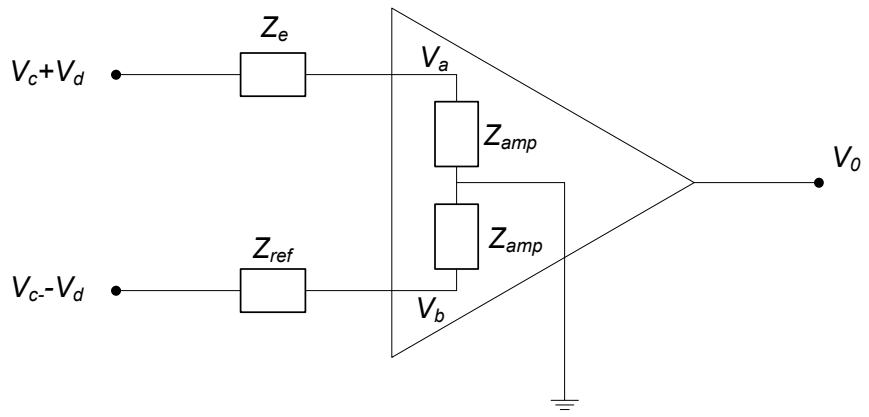

Figure 5-15. Schematic diagram of differential amplifier attached to recording electrode and reference electrode.

be given as

$$V_0 = G(V_a - V_b) + \frac{G}{CMRR}(V_a + V_b), \tag{5–1}$$

where G is the gain of the amplifier and $CMRR$ is the common-mode rejection ratio. Using voltage division, Equation 5–1 may be stated as

$$V_a - V_b = V_d \left(\frac{Z_{amp}}{Z_e + Z_{amp}} + \frac{Z_{amp}}{Z_{ref} + Z_{amp}} \right) + V_c \left(\frac{Z_{amp}}{Z_e + Z_{amp}} - \frac{Z_{amp}}{Z_{ref} + Z_{amp}} \right). \tag{5–2}$$

Two terms are shown in Equation 5–2, one relating to the differential signal and the other to the common signal, that will be amplified and given as output. Ideally, Z_{amp} is much larger than Z_e or Z_{ref} so that V_d is not attenuated and V_c is reduced to zero. Figure 5-16 shows the attenuation factor of V_d for a range of Z_e and Z_{ref} impedance values when the input impedance of the amplifier is $10^7\Omega$. (This impedance is very close to the value experimentally measured at 1 kHz for the amplifier on the UF microelectrode.) Note that the normalized value of 1 represents no attenuation of the differential signal. The circle indicates the assumed range of impedance values for typical recording and reference electrodes. As the figure shows, there is possibly 5% attenuation for a combination of recording and reference electrode impedances in that range for an amplifier input impedance of $10^7\Omega$. However, if the recording electrode impedance is the same as the input impedance to the amplifier, then the attenuation

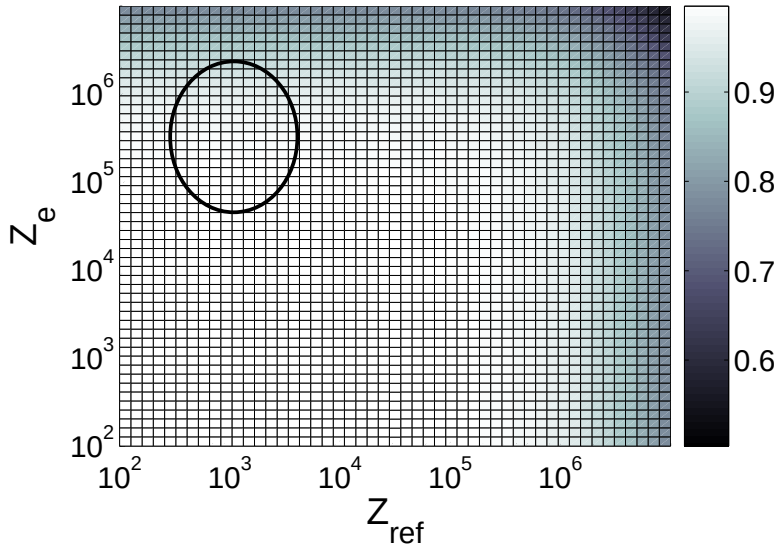

Figure 5-16. Attenuation factor of V_d as a function of Z_e and Z_{ref} corresponding to voltage division at input of the amplifier.

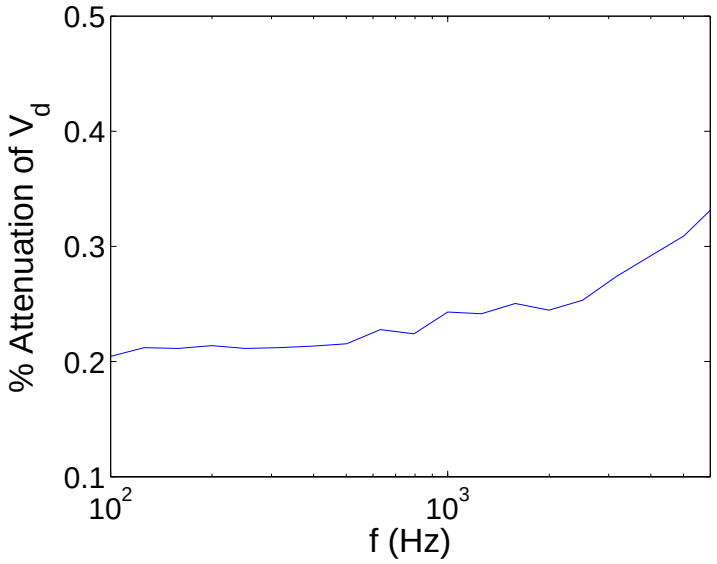

Figure 5-17. Percent attenuation of the differential signal V_d as a function of frequency due to voltage division at the input of the amplifier.

is 50%. For the impedance values in the UF amplifier-microelectrode system, the attenuation of V_d is minimal (∼0.3%) as shown in Figure 5-17.

The amplification of the common mode signal is assessed next. Figure 5-18 shows the dependence of attenuation of V_c on the recording and reference electrode

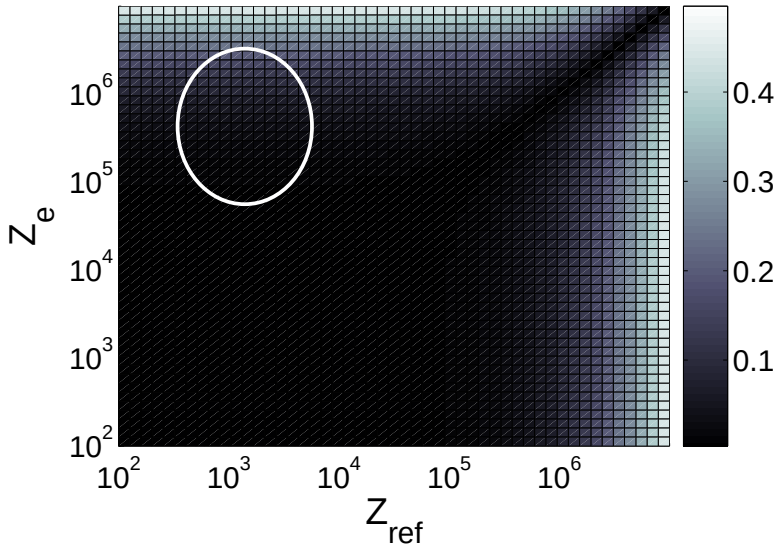

Figure 5-18. Attenuation factor of V_c as a function of Z_e and Z_{ref} corresponding to voltage division at input of the amplifier.

impedances for $Z_{amp} = 10^7\ \Omega$. In the impedance range applicable to this work, the plot shows that at most 5% of the common-mode signal will be amplified by the amplifier gain and result as an unwanted disturbance in the output signal. Using the impedance values as a function of frequency for the UF amplifier-microelectrode system, no more than 0.8% of the common-mode signal will be amplified by the amplifier as shown in Figure 5-19.

An effective common-mode rejection ratio dependent on the relative impedance values of the recording and reference electrode is given next following the derivation by Legatt et al. [125]. Assuming $Z_e \ll Z_{amp}$ and $Z_{ref} \ll Z_{amp}$, Equation 5–2 may be simplified to

$$V_a - V_b = 2V_d + V_c \frac{Z_{ref} - Z_e}{Z_{amp}}. \tag{5–3}$$

Similarly,

$$V_a + V_b = V_d \left(\frac{Z_{amp}}{Z_e + Z_{amp}} - \frac{Z_{amp}}{Z_{ref} + Z_{amp}} \right) + V_c \left(\frac{Z_{amp}}{Z_e + Z_{amp}} + \frac{Z_{amp}}{Z_{ref} + Z_{amp}} \right) \tag{5–4}$$

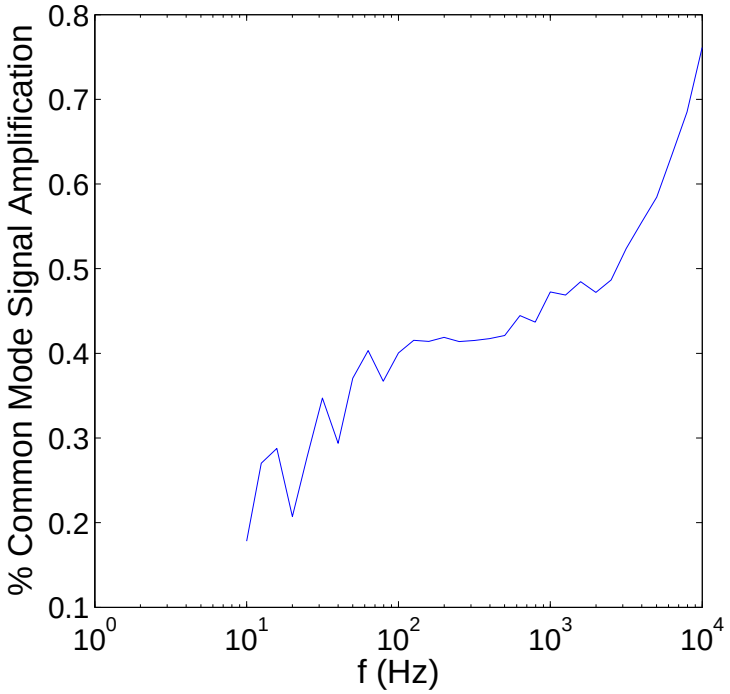

Figure 5-19. Percent of the common-mode signal V_c as a function of frequency that will be amplified due to voltage division.

and

$$V_a + V_b = 2V_c + V_d\left(\frac{Z_{ref} - Z_e}{Z_{amp}}\right). \tag{5–5}$$

Plugging Equation 5–3 and Equation 5–5 into Equation 5–1 yields

$$V_0 = GV_d\left(\frac{2CMRRZ_{amp} + (Z_{ref} - Z_e)}{Z_{amp}CMRR}\right) + GV_c\left(\frac{CMRR(Z_{ref} - Z_e) + 2Z_{amp}}{Z_{amp}CMRR}\right). \tag{5–6}$$

The effective common-mode rejection ratio is taken to be the gain associated with V_d divided by the gain associated with V_c. Thus,

$$CMRR_{eff} = \frac{2CMRRZ_{amp}}{2Z_{amp} + CMRR(Z_{ref} - Z_e)}, \tag{5–7}$$

using these simplifications $Z_{amp} \gg (Z_{ref} - Z_e)$ and $CMRR \gg 1$. Figure 5-20 shows the effective common-mode rejection ratio due to a mismatch in recording and reference electrode impedances. According to Legatt's derivation, the effective CMRR will be significantly decreased for a large mismatch in impedance. In this study,

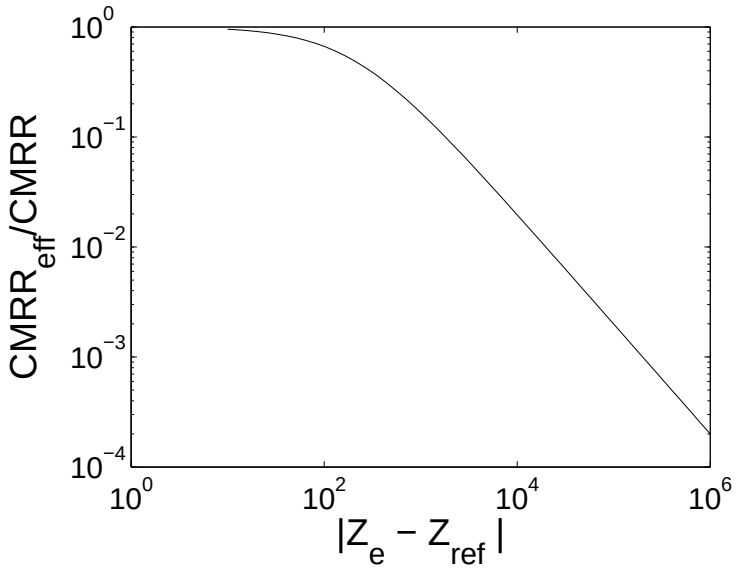

Figure 5-20. Normalized effective common-mode rejection ratio as a function of the difference of the impedance between recording electrode and reference electrode.

the reference electrode and recording electrode have impedances that differ by two orders of magnitude. Figure 5-21 shows a hypothetical effective common-mode rejection ratio using the impedance values given in Figure 5-14. The nominal CMRR for the UF amplifier is 10,000. Thus according to Legatt's derivation, the effective CMRR will decrease by a factor of 20. However, a measurement performed to test this hypothesis did not show congruent results for the UF microelectrode. When the impedance of the reference and recording electrode were matched by replacing the large area reference screw with a 50 μm diameter tungsten microwire (similar to the recording electrode), the amount of common-mode noise (60 Hz EMI) actually increased rather than decreased. Therefore, other factors besides impedance mismatch contribute to the presence of 60 Hz EMI common-mode noise seen in Figure 5-13. Understanding the origin of such factors are a topic of future research.

5.5.4 Lessons Learned for Integration with the Integrate-and-Fire Chip

The important lessons learned from the previous benchtop studies that pertain to successful integration with a UF integrate-and-fire (IF) chip are discussed next. First,

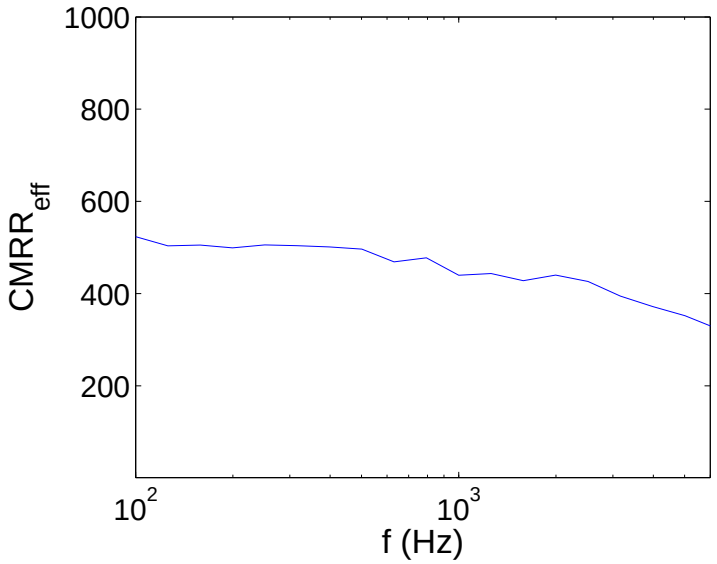

Figure 5-21. Effective common-mode rejection ratio as a function of frequency for impedance values in the UF microelectrode array.

the reference connection to the amplifier should be connected to the system ground (V_{ss}) of the amplifier to reduce noise pick-up during implantation. If this can be done on a chip level, instead of on the flexible substrate, that is advised. The signal coming from the amplifier must be filtered to eliminate the 60 Hz power line EMI, before it is sent to the integrate-and-fire electronics. A band-pass filter from 500 Hz to 6 kHz was used successfully in this study.

5.5.5 Frequency Response and Impulse Response of System

The frequency response and the impulse response of the amplifier-microelectrode system were experimentally obtained to confirm that the system will be able to correctly record and amplify a neuronal action potential. The frequency response was measured using an SRS785 spectrum analyzer. The input signal, 100 μV white noise, was applied to a beaker of saline within which the microelectrode was immersed. The frequency response of the system given in Figure 5-22 shows a pass-band gain of 39 dB. The response of the system to pulses of width 1 ms and 100 μs are given in Figure 5-23. Minimal distortion is seen on the 1 ms pulse; more pronounced distortion is seen in

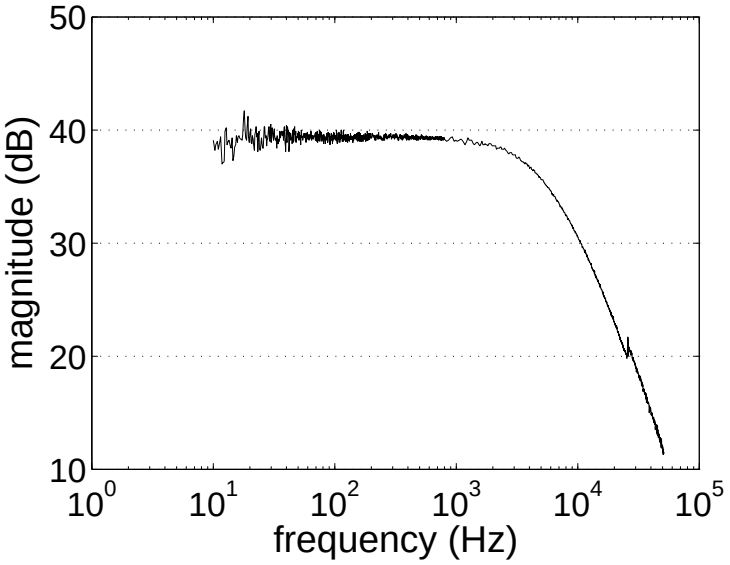

Figure 5-22. Frequency response of amplifier-microelectrode system. The pass-band gain is 39 dB.

the 100 μs pulse response. Since an action potential has pulse lengths on the order of milliseconds, this amplifier-microelectrode system measures the signal without appreciable distortion.

5.6 *In-Vivo* Testing

The recording performance of the amplifier-microelectrode system was validated by conducting an in-vivo investigation on an anesthetized rodent. The flexible microelectrode-amplifier system was implanted into an adult male Sprague-Dawley rat. All animal procedures have been approved by the University of Florida IACUC. The rat was anesthetized at the beginning and the surgical site was sterilized completely. A mid sagital incision was made between the eyes to uncover the top of the skull, and the landmarks bregma, and lambda were then identified on the skull. A craniotomy was drilled (+1mm anterior to bregma, 2.5mm lateral) at the site corresponding to the forelimb region of the motor cortex [119]. At the site of the electrode implantation, the dura was removed to expose the cortex. The entire assembly was implanted vertically and lowered using a micropositioner. While driving the electrode, electrophysiologic recordings were used

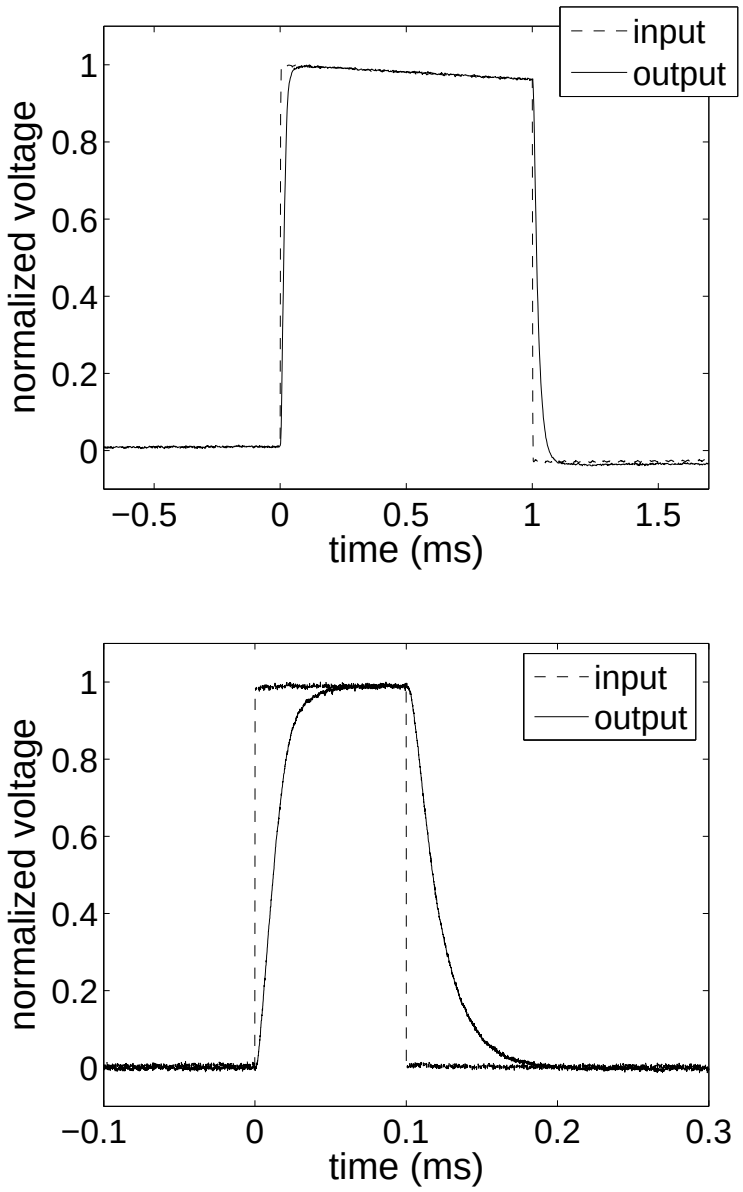

Figure 5-23. Impulse response of amplifier-microelectrode system. Figure 5-23A shows the response to a 1 ms pulse, characteristic of a neural action potential. Figure 5-23B shows the response to a 100 μs pulse.

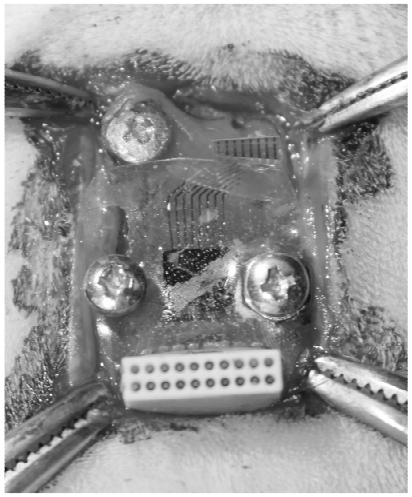

Figure 5-24. Flexible substrate electrode array implanted in rodent model.

to locate a depth where unit cell activity was greatest. The electrodes were driven to a depth of 3.6 mm. During this procedure, the assembly was observed to be rigid and no buckling was present. Once the electrode was positioned, it was supported with cranioplastic cement (Plastics-1) attached to a screw placed adjacent to the craniotomy (top screw in Figure 5-24). After the array was secured, the entire assembly was folded down to lay flat against the table of the skull as shown in Figure 5-24. The flexible substrate was then permanently grounded using a second anchoring screw.

The electrode array was implanted in the animal for 42 days and neural signals were measured at regular intervals over the implanted duration. The results observed from the chronic implantation of the microelectrode array are described next.

5.6.1 *In-Vivo* Recording Results

Recordings were made with the implanted amplifier-microelectrode system and Tucker Davis Technologies recording software and storage hardware on the day of surgery and intermittently over the following 42 days. On the day of surgery, many large amplitude action potentials were measured at the final implant depth of 3.6 mm. Figure 5-25 shows characteristic spikes recorded from one channel. However, consistent spikes of similar large amplitudes were not seen again over the implant

duration. The subsequent recordings exhibited consistent, but low amplitude neural activity. Table 5-3 shows the yield, or the number of neurons seen consistently over the implant duration, for each electrode on the array. Spike2 was used to sort the recorded

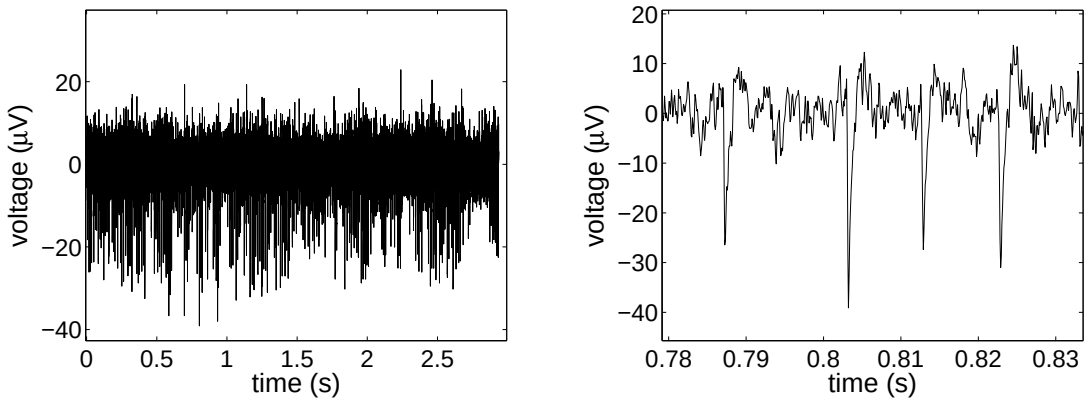

Figure 5-25. Large amplitude action potentials recorded on day of implantation.

data for various days over the implant duration using the same methods described in Section 4.1.4 and Section 4.2.4. Figure 5-26 depicts a characteristic action potential of a single neuron seen consistently over the implant duration. The graphs show average waveforms of sorted action potentials over a one minute time segment. The red lines give the error bounds. Statistical analysis of the waveform templates prove that the same neuron was consistently measured over the course of the implant time.

Table 5-3. Neuronal Yield for Generation 2b Microelectrode Array

Electrode	Neuronal Yield
1	2
2	1
3	3
4	2
5	1
6	1
7	0
8	1

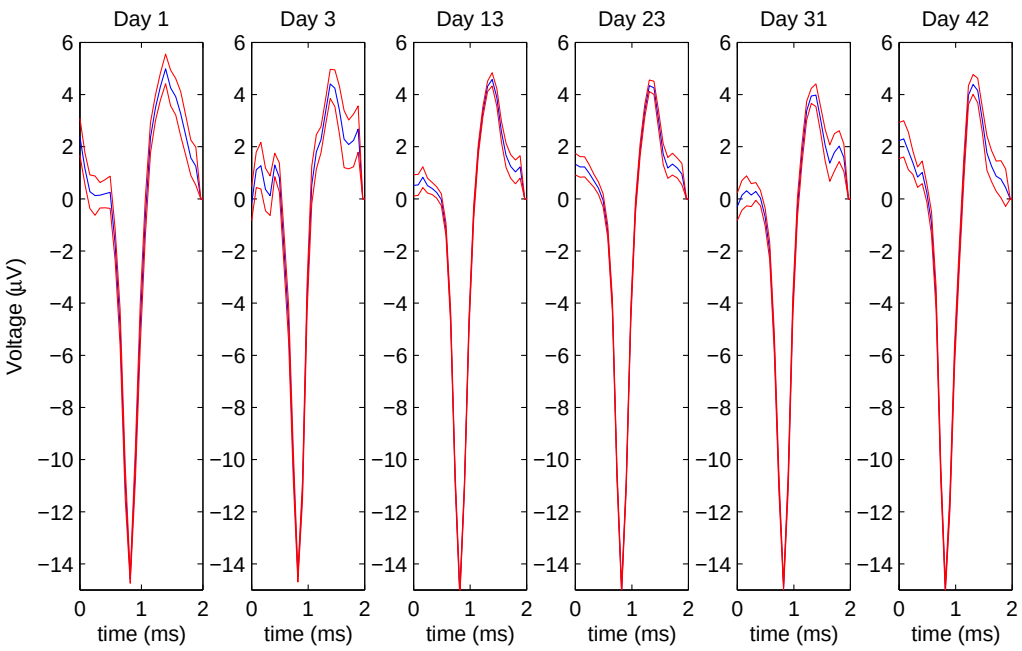

Figure 5-26. Action potential of a single neuron spike sorted over the implanted period.

Noise floor and signal to noise ratio are the other recording performance metrics considered for the amplifier-microelectrode system. The noise floor for the electrode array over the implant duration is shown in Figure 5-27. Day 0 corresponds to bench-top measurements made in 0.9% saline. The bench-top noise measurement for a Tucker Davis electrode attached to a Tucker Davis amplifier (PZ2) is given in red in the figure. The Tucker Davis electrode noise floor is statistically similar to the noise floor for the UF microelectrode array. Results for days 1 through 42 are taken from in vivo recordings with the UF microelectrode array. The data points give the root mean square values of a one second or greater segment of data, free of sorted action potentials. The error bars correspond to the sample standard deviation of seven channels in the electrode array. After an initial increase in the average noise floor, it remained constant around 4.5 μVrms. Figure 5-28 shows the average signal to noise ratio (SNR) across seven channels in the array over the implant duration. SNR was calculated as the peak to peak voltage of an action potential divided by the rms noise floor value. Results for this electrode show SNRs as high as 5.4 on the day of surgery and consistent vales near 3.8

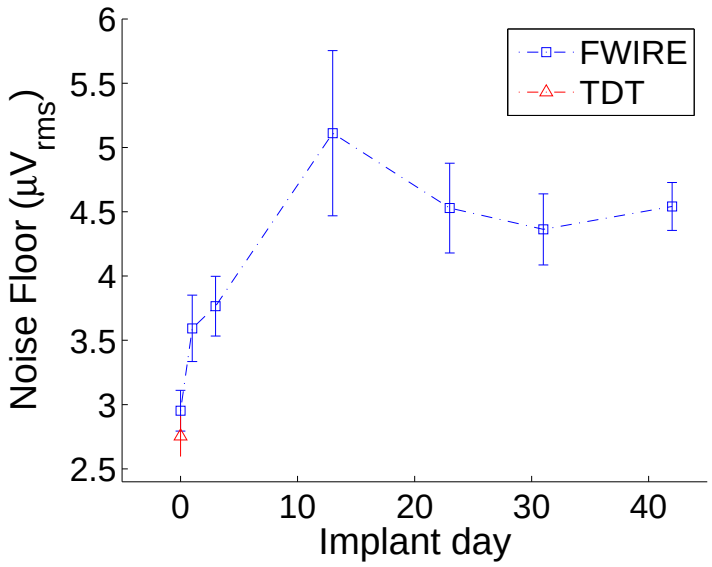

Figure 5-27. Noise floor for the electrode array over the implanted duration. FWIRE corresponds to the UF amplifier-microelectrode system and TDT corresponds to a Tucker Davis micro-wire electrode array and PZ2 amplifier.

after 23 days implanted. The spike sorting results showed at least one neuron on seven of the electrode channels. All action potentials corresponding to single neurons used for the SNR calculation were consistently recorded from day 1 to day 42.

Performance metrics including noise floor, signal to noise ratio, and neuronal yield showed that the amplifier-microelectrode array performed adequately. The noise floor was statistically similar to the noise floor of a Tucker Davis electrode in *in vitro* experimentation over a frequency range of 500 Hz to 6 kHz. The average noise floor measured *in vivo* on the first day of implantation was less than one microvolt higher than that measured in saline. The increase in the noise floor was assumed to be from addition of background neuronal noise. The average noise floor then increased to a value about one microvolt higher than it was on day one. The cause of this increase in noise after day one is more ambiguous; however, the same trend has been reported by the Michigan group [21]. They also measured impedance values over time and concluded that an increase in electrode impedance by 30% to 100%, which coincided

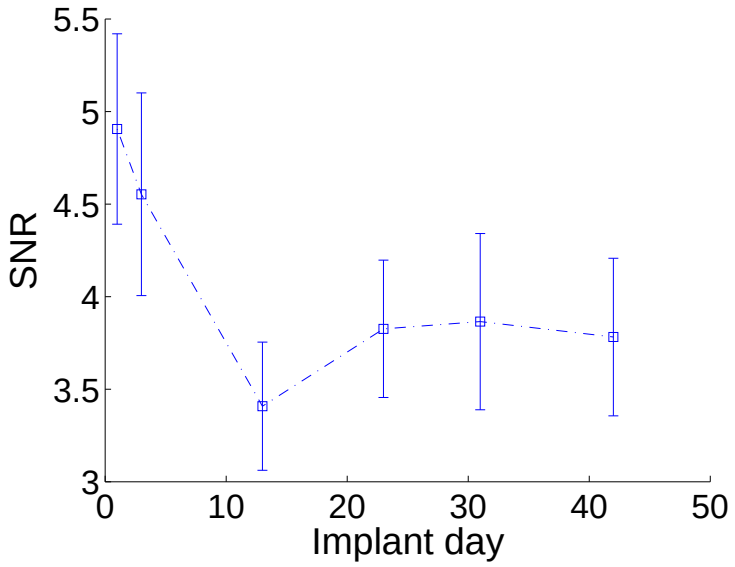

Figure 5-28. Signal-to-noise ratio for the electrode array over the implant duration. FWIRE corresponds to the UF amplifier-microelectrode system and TDT corresponds to a Tucker Davis micro-wire electrode array and PZ2 amplifier.

with the increase in noise, was at least partially the cause of the increase in noise floor. Tresco's group reported that increases in electrode impedance of the same magnitude are attributed to cellular adhesion [77]. Signal to noise ratios reported for the UF microelectrode array after day one were low compared to most published data, but because they are dependent on the proximity of an active neuron, they are not a relevant indication of performance quality especially when the noise floor is adequately low. The percentage of active electrodes on the UF microelectrode array over the implant duration stayed constant at 88% and 1 to 3 independent neurons were measured on each active channel. Thus, the UF microelectrode array with hybrid-packaged amplifier IC shows acceptable performance for recording applications lasting two months.

5.6.2 Post-Implant Electrode Assessment

Motivation for the electrochemical analysis of electrode materials in this work is given by examining the electrode sites of the UF intracortical microelectrode array after

implantation in brain tissue. Figure 5-29 shows scanning-electron-microscope (SEM) images of the tungsten microwires used in the UF intracortical microelectrode array before and after implantation in a rodent motor cortex. The microelectrode array was implanted for 87 days. Images labeled a and b show electrode surfaces (cross section of the insulated wires) after they have been cut with a dicing saw prior to implantation. The microwires have a sub-micron layer of gold on the outside surface of the tungsten wires, beneath the polyimide insulation. Though not easily seen in the SEM images, a thin ring of gold between the polyimide and tungsten is exposed to the biological environment. Images c and d show the changed state of the tungsten wire after 87 days *in vivo*. The inset in c highlights the area of gold exposed to the tissue. Notable differences between the before and after images include a larger area of gold exposed in the after state as well as a swelling of the polyimide insulation and the presence of a film on the surface of the electrode. The larger electrode area will correspond to a lower impedance and thus a lower thermal noise voltage at the interface; however, the electronic noise of the amplifier will still dominate the system. Also, the resulting measured voltage signal will be averaged over the larger surface area. A magnified view of image d in Figure 5-30 and energy-dispersive X-ray spectroscopy (EDS) results for two exposed regions on the electrode surface is shown in Figure 5-29. The top EDS graph gives results characteristic of a bare tungsten surface. The bottom EDS graph gives results characteristic of a bio-film that is rich in carbon, oxygen and nitrogen. Thus, it is assumed that part of the bio-film became dislodged on the top right portion of the electrode and is exposing the tungsten surface. This image shows that the tungsten is recessed within the gold plating and the structure of the tungsten surface has changed from being smooth to rough. In three of the electrodes in the array, the average distance that the tungsten surface was recessed within the gold plating was measured to be 24 ± 8 μV after an implantation duration of 87 days. The distance was measured via an optical microscope where the change in focal length was measured. The corrosion of

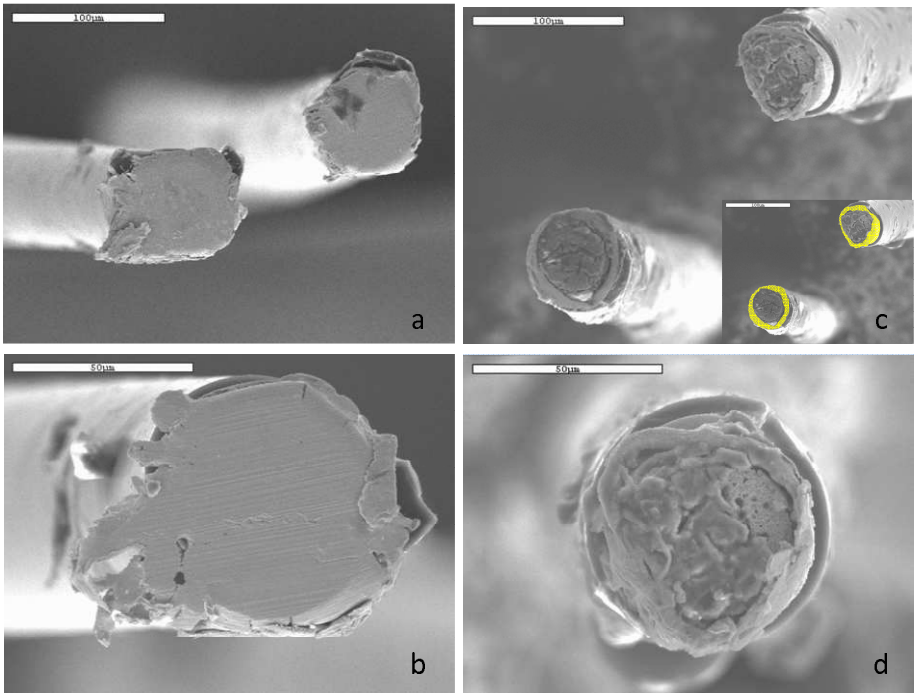

Figure 5-29. SEM images of tungsten micro-wires before and after 87 days implanted. a,b) Characteristic electrodes before implantation. c,d) Characteristic electrodes after implantation. The inset in c highlights the area of gold exposed to the tissue.

tungsten microwires is systematically studied in an *in vitro* experiment and the effect of the tungsten corrosion on long-term recording performance is discussed in Chapter 7.

5.7 Summary

A prototype of a chronically implantable active microelectrode array has been designed for a Sprague-Dawley rat and tested in a long-term *in vivo* experiment. This design successfully incorporated an 8-channel amplifier IC via flip-chip bonding to a polyimide-based substrate. Chronic recording results confirm that the amplifier-electrode system reliably measures and amplifies single unit neural signals over 42 days. Past 42 days, signal recording was intermittent and much noisier. Analysis after explantation showed that the polyimide layer delaminated near the Omnetics connector allowing the ground and power signal input pads to be shorted together through the bio-fluid. Next generations should incorporate a silicone insulation layer on the extent of the

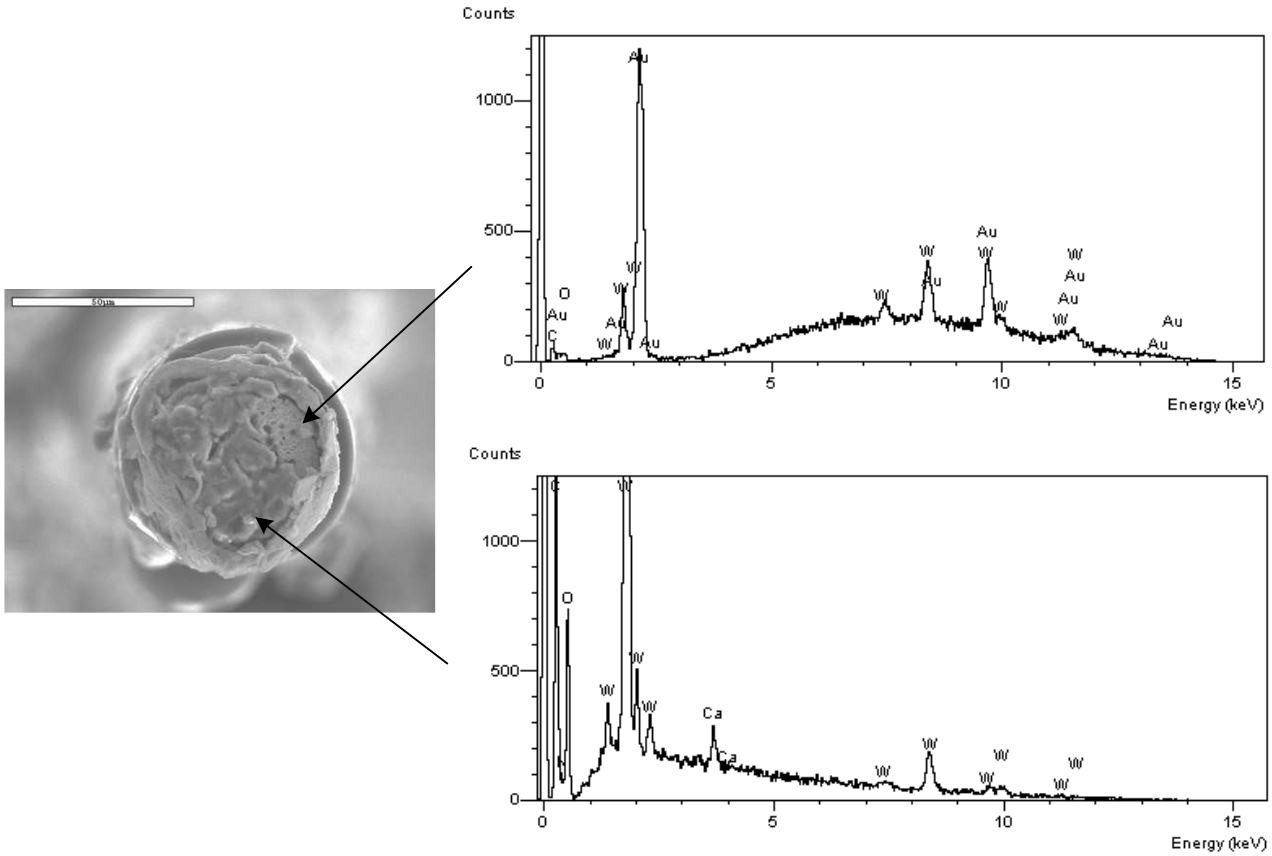

Figure 5-30. EDS results of two sites on one electrode after 87 days *in vivo*. The top graph shows results characteristic of a bare tungsten and gold surface. The bottom graph shows results characteristic of a bio-film.

polyimide surface. Furthermore, SEM images of the tungsten recording sites after explantation showed considerable change in the electrode surface suggesting corrosion of the tungsten. Though the results for 42 days do not suggest that the corrosion of the tungsten microwire had any adverse effect on the recording performance thus far, there is a possibility that adverse effects may occur in prolonged studies. The results of a detailed analysis of corrosion properties of tungsten microwires are presented in Chapter 7. The experimental methods are explained in the next chapter.

CHAPTER 6
ELECTROCHEMICAL CHARACTERIZATION OF ELECTRODES: METHODS

As exemplified in Chapter 5, the implanted tungsten microwires undergo corrosion. This chapter presents the experimental methods for the electrochemical characterization that will quantify the rate of corrosion experienced by tungsten microwires in physiological saline solutions. The key measurement technique, electrochemical impedance spectroscopy (EIS), is described. Uncommon graphical representations of the impedance data that provide useful information on the interface physics are explained. The procedure for error analysis of the measured impedance data is also described. Moreover, the metal samples used in the EIS measurements must be different from the microwire electrodes used in neural recording microelectrodes. Reasons for this change are given and a method for ascertaining the quality of the sample electrodes is also presented.

6.1 Electrochemical Impedance Spectroscopy

Electrochemical impedance spectroscopy (EIS) is a measurement technique used to characterize charge transport at an electrochemical interface under steady-state conditions [93]. A typical experimental set-up is shown in Figure 6-1. The working electrode is the surface under scrutiny. The counter electrode is a large area electrode whose interfacial phenomena may be neglected [93]. The reference electrode is an electrode that possesses a reversible reaction with an ion in the cell solution that has a constant and well-defined electrochemical potential [93]. By applying a small sinusoidal voltage or current perturbation across the working and counter electrode and subsequently measuring the resulting current or voltage signal across the working and reference electrode, the impedance at a given frequency may be measured. Care must be taken to ensure that the perturbation voltage is small enough to ensure that the current to voltage relationship remains linear [126]. The perturbation signal is swept over a range of frequencies and the resulting frequency-dependent impedance

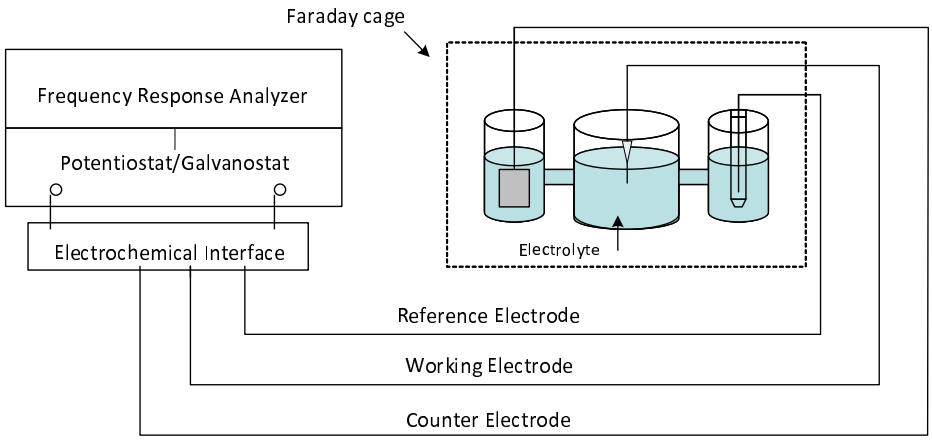

Figure 6-1. EIS experimental set-up.

is characteristic of the interface between the working electrode and the electrolyte medium.

EIS has been used in studies characterizing stimulating and recording electrodes for pacemaker and intracortical applications as well as various studies on micro-scale electrodes. Interfacial capacitance was assessed by EIS in physiological saline on Pt, Ti, and TiN pacemaker electrodes used for stimulation [87, 88]. Impedance and charge transfer characteristics of electrodeposited IrO_2 in saline solution were compared to bare metal surfaces using EIS [127]. The final application of the IrO_2 plated electrodes was for neural stimulation and recording. Platinized-platinum microelectrodes used for neural stimulation were characterized using EIS [102]. Yang et al., Cui et al., and Ates et al. investigated conducting polymer films grown or deposited on metal microelectrodes via EIS [128–130]. Price et al. used EIS to assess optimal insulation thickness for their microelectrode arrays [131]. Zhang et al. modified microelectrodes with immobilized antibodies for selective capture of human antigens and used the change in impedance measured by EIS as the sensing mechanism [132]. This work uses EIS to ascertain the reactivity of a metal in biological saline solutions under quasi-equilibrium conditions, and in the case of a reactive system undergoing corrosion; this work quantifies the corrosion rate through extrapolation of the polarization resistance from the impedance data.

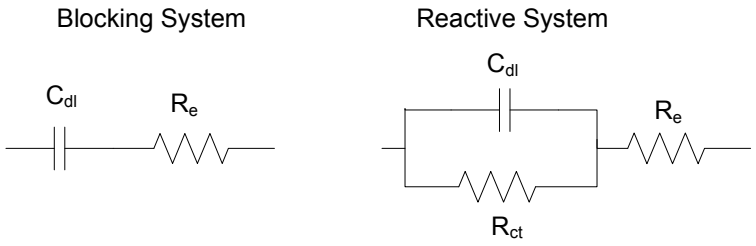

Figure 6-2. Equivalent circuits for blocking and reactive system (nonfaradaic and faradaic interface) [1].

6.1.1 Graphical Data Analysis Techniques

This section introduces graphical techniques used to analyze electrochemical impedance data. Bode plots of impedance magnitude and phase are frequently used in electrical engineering to view impedance data and are also used in electrochemistry; however, they do not show interface characteristics as well as other graphical methods. The complex impedance plane or Nyquist plot and plots of logarithmic imaginary impedance as a function of frequency, introduced by Orazem et al. [133], are used to acquire meaningful information about the electrochemical system.

To compare the graphical techniques for analysis of impedance data, plots of theoretical curves for blocking and reactive systems modeled by the equivalent circuit diagrams in Figure 6-2 are discussed here. Figure 6-3 shows Bode plots, where impedance magnitude and phase as a function of frequency are shown. Both blocking and reactive systems show resistive behavior at high frequencies, denoted by the zero degree phase angle. The blocking system is dominated by the capacitor at low frequencies and thus shows increasing magnitude of impedance and a phase angle of -90°. The reactive system has a resistive current pathway at low frequencies, therefore; the impedance magnitude levels off to a finite value and has phase angle of zero degree at low frequencies.

The Nyquist plot is useful for graphical estimation of the electrolyte resistance, R_e, and the charge transfer resistance, R_{ct}. Figure 6-4 shows a Nyquist plot, which is the negative of the imaginary impedance as a function of the real impedance, for the two

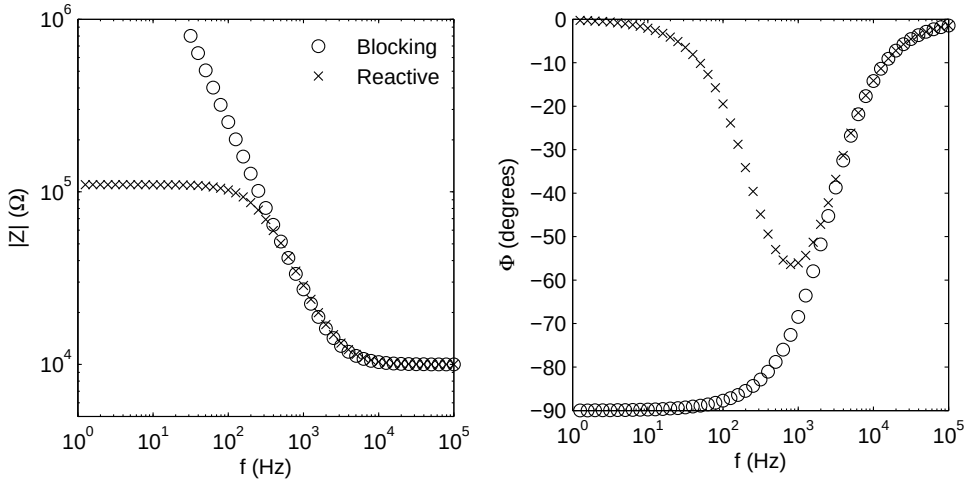

Figure 6-3. Bode plots of a blocking and reactive system.

interface cases. The high frequency asymptote gives the value of R_e for both systems. As the frequency decreases, the imaginary impedance value will either grow toward infinity for the blocking system or achieve a maximum and then decrease back to zero in the reactive system. The low frequency asymptote for the reactive system gives $R_e + R_{ct}$.

The logarithm of imaginary impedance as a function of frequency in Figure 6-4 gives a straight line of slope equal to -1 for all frequencies in the ideal blocking system and for high frequencies in the reactive system [133]. This method of viewing impedance data is most useful for experimental data showing non ideal behavior.

The Constant Phase Element: Experimental results of EIS measurements on metal-electrolyte interfaces do not normally show behavior that can be completely modeled by the reactive and blocking equivalent circuits in Figure 6-2. Deviations from ideal cases are modeled by the constant-phase element (CPE). The constant-phase element has a multitude of origins and is highly dependent on the system. It is commonly suggested that CPE behavior arises from an inhomogeneous surface [134]. Regardless of the physical meaning, it can be considered an element with a distribution of time constants, which can be modeled by Equation 6–1.

$$Z_{cpe} = \frac{1}{(j\omega)^{\alpha} Q}, \tag{6–1}$$

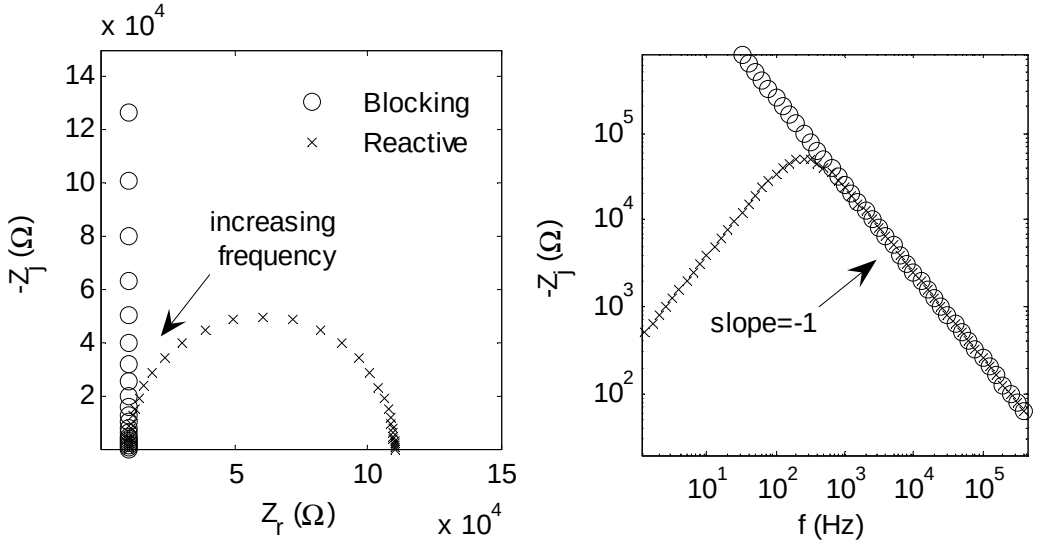

Figure 6-4. Nyquist plot (left) and logarithm of imaginary impedance as a function of frequency (right) of blocking and reactive systems.

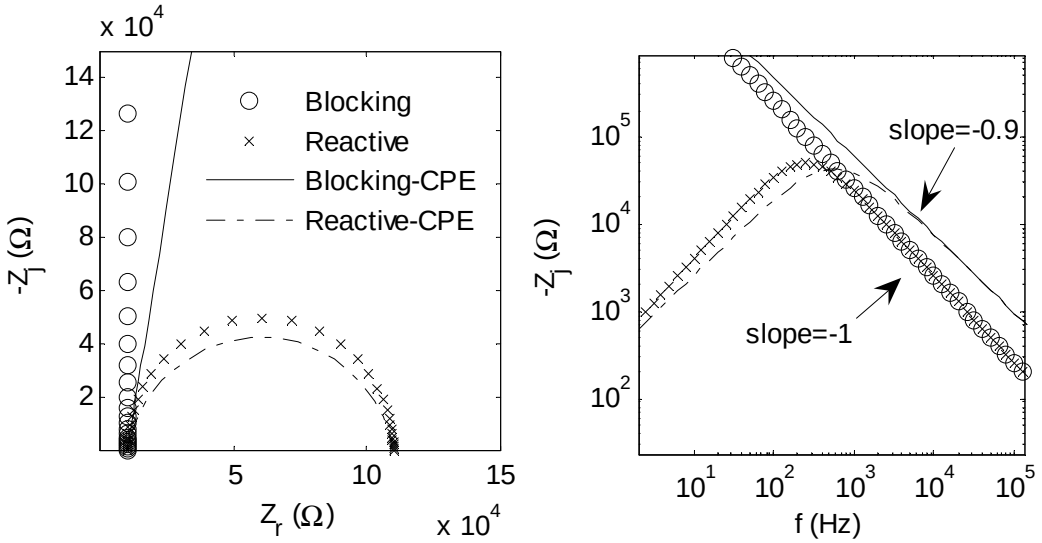

Figure 6-5. Nyquist plot (left) and logarithm of imaginary impedance as a function of frequency (right) for blocking and reactive systems with a constant phase element.

where α is a number from 0 to 1, and Q is the quantity of the CPE with units $s^{\alpha}/\Omega cm^2$ [134]. The CPE takes the place of the double layer capacitor in the interface equivalent circuits.

The Nyquist plot and logarithm of the imaginary impedance as a function of frequency show a unique dependence with the constant-phase element. In the Nyquist plot, the CPE makes the vertical line tilt to the right at an angle less than 90° in a blocking system; and in a reactive system, the semicircle is depressed as shown in Figure 6-5. In the graph of logarithm of imaginary impedance as a function of frequency, the slope of the impedance for both systems is decreased from 1 and equals the value of $-\alpha$ from Equation 6–1.

Thus, by using Nyquist plots and the logarithm of imaginary impedance as a function of frequency instead of Bode plots, more of the interface characteristics are apparent. The difference between a blocking and reactive system is simply given by the shape of the Nyquist plot (eg. a straight line versus a semicircle). Furthermore, values of circuit parameters (R_e, R_{ct} and α) are able to be estimated.

6.1.2 Error Analysis

This section explains the method used to assess stationarity, linearity, causality, and measurement error of the measured impedance data. This method proposed by Orazem [135] is an iterative approach that uses a measurement model, which inherently satisfies the Kramers-Kronig relation and thereby exhibits linearity, stationarity, and causality. The measurement model for complex impedance is given by [135]

$$Z = R_0 + \sum_{k=1}^{k} \frac{R_k}{1 + j\omega\tau_k}. \tag{6–2}$$

A resistor, R_0 modeling the electrolyte resistance, is in series with k Voigt elements, where a Voigt element is a capacitor in parallel with a resistor that has a characteristic time constant $\tau_k = 2\pi RC$. Complex nonlinear least squares regression is used to fit the experimental data to the measurement model with the largest number of Voigt elements

that is statistically significant. Then the variance for the real data for three or more measurement scans, N, is found by

$$\sigma^2_{Z_r}(\omega) = \frac{1}{N-1}\sum_{k=1}^{N}(\epsilon_{res,Kr,k}(\omega) - \bar{\epsilon}_{res,Kr}(\omega))^2, \tag{6–3}$$

where $\epsilon_{res,Kr,k}(\omega)$ is the residual error of the model to the data at frequency ω for scan k and $\bar{\epsilon}_{res,Kr}(\omega)$ is the mean value of the residual errors at frequency ω. The variance for the imaginary part is found similarly.

Next, the variance is transformed into an error structure so that it may be applied to a general impedance spectra. It has been shown that the variance of the real and imaginary parts of the impedance spectra are equal [136]. Thus the error structure of electrochemical impedance can be found when regressed to this formula

$$\sigma_{Z_r} = \sigma Z_j = \alpha|Z_j| + \beta|Z_r| + \gamma\frac{|Z|^2}{R_m} + \delta, \tag{6–4}$$

where α, β, γ, and δ are coefficients to be found in the regression, and R_m is the value of the resistor used in the measurement equipment [135].

The residual error ϵ_{res} found above includes bias error, stochastic error and error to the fit. However, reference [135] suggests that it can be a good estimate for the stochastic error if the same number of Voigt elements are used to fit each scan. Then, the model parameters account for drift in each subsequent scan, and error due to non-stationarity is the same from one scan to another. In a more sensitive analysis for stationarity, the error structure from Equation 6–4 is used to weight the regression of the imaginary impedance data for one scan, and then the real part is predicted via the Kramers-Kronig relation. If the predicted values are within the 95% confidence interval of the regression, then the data are consistent with the Kramers-Kronig relation. If data at the extents of the measured frequency range do not fit in the confidence interval then, they are discarded and the procedure is performed again. Inconsistency

with Kramers-Kronig relations means that bias errors, which could be from instrument artifacts or non-stationary behavior, are confounding the measurement.

Through this approach, an error structure representing the stochastic error is found, and the measured data are checked for linearity, stability, and casuality. The error structure can then be used as weighting for regression of physical models representing the electrochemical system.

6.2 Microelectrodes used for Electrochemical Characterization

To realistically assess the electrochemical behavior of tungsten microwires used in neural recording applications, the same microwires are used in the formation of the working electrode for EIS. The tungsten microwires used for intracortical microelectrodes consist of 50 μm diameter tungsten wires that are plated with a thin layer of gold and are insulated with approximately 3 μm of polyimide. The gold allows the microelectrode to be soldered easily. The ends of the wires are cut (via a dicing saw) in the microelectrode fabrication process to expose the cross-section as the recording site. During the cutting process, the insulation is pulled away from the tungsten microwire to some extent, creating an imperfect seal. For electrochemical characterization of the metal-to-electrolyte interface, an electrode surface with a well defined surface area and perfect seal with the insulation is needed. Otherwise, artifacts would arise from the imperfect insulation seal and confound interpretation of electrochemical phenomena at the interface. Gaps at the metal-to-insulator boundary can be modeled as porous electrodes. Many have presented unique impedance responses due to porous electrodes [137–139]. Thus, the tungsten microwires with polyimide insulation cannot be used. Also, the exposed sidewalls would affect the accuracy of the estimation of the surface area needed for calculation of the corrosion rate. Therefore, the working electrodes for the EIS study are made similarly to conventional microelectrodes used for electrochemical applications.

The use of microelectrodes (defined as electrodes with dimensions in the micrometer range) in electrochemical applications is briefly discussed to give a counterpoint to microelectrodes used in brain-machine interfaces. In electroanalytical chemistry, microelectrodes provide advantages over macroelectrodes including: fast mass transport, reduced capacitance, and low current [140, 141]. These properties remove the need for forced convection in the cell, reduce the RC time constant, which allows investigation of high speed kinetics, and render the Ohmic drop over the electrolyte resistance negligible such that use in high resistivity media is possible. Moreover, their small size provides an obvious benefit to biological applications where minimal tissue damage is necessary and spatial resolution is important. Wightman's group have been using microelectrodes since the 1980's to determine the presence of neurochemicals in the brain [142, 143], among many other applications. A more recent application of microelectrodes is in electrochemical impedance spectroscopy studies that employ scanning electrochemical microscopy (SECM) to assess local characteristics of bulk materials [144, 145].

Microelectrodes and microelectrode arrays (MEAs) for electroanalytical applications are fabricated in a number of ways [146]. Methods include insulating metal wires or carbon fibers with glass, epoxy, or a polymer and then polishing or electrochemically etching one end. Microfabrication techniques are used to lithographically pattern vapor deposited thin film metals and insulating dielectrics. Microelectrode arrays are typically fabricated using micromachining techniques. Whether made by either method, the microelectrodes are at risk for defects such as imperfect seals between the electrode and insulation [146]. Contaminants on the surface from perhaps a polishing step also pose threats to the quality of the measurement [146].

6.3 Quality Control of Microelectrode Fabrication

Few papers describe a method for quality control of microelectrodes. Thormann et al. find that square wave and AC voltammetry and short-time chronocoulometry

measurements are highly affected by imperfect seals between the metal and insulator [147]. Results show deviation to theory though an asymmetric voltammetric response, where the nonideal response is exacerbated as the pulse width is decreased or frequency is increased. Koster et al. provide a method for quality control of microelectrode arrays (MEAs) made by micromachining and used for amperometric transducers [148]. They use a combination of cyclic voltammetry, electrochemical impedance spectroscopy, and scanning electrochemical microscopy to assess the quality of their arrays. This work introduces a simple method that uses only electrochemical impedance spectroscopy (EIS) to assess the quality of microelectrode fabrication.

This method uses a graphical interpretation of impedance data following Orazem et al. [133] and Huang et al. [149–151]. In references [149–151], a method for comparing impedance data of electrodes of differing size and electrolyte conductivity is given as well as a criterion for distinguishing artifacts in impedance data. They proved that geometry induced current and potential distributions at high frequencies produced artifacts in the impedance spectra of disc electrodes. Therefore, we will use the same method to uncover artifacts in the impedance spectra of microelectrodes due to fabrication defects. This paper applies the method prescribed for blocking electrodes showing constant phase element (CPE) behavior [150].

6.3.1 Quality Control Methods

It has been shown that short-time scale electrochemical measurements are sensitive to imperfections in the metal to insulator seal in microelectrodes and that epoxy sealed microelectrodes are highly susceptive to such defects [147]. This quality control study uses two sets of Pt microelectrodes; one set is insulated with epoxy and the other with glass, which is known to have high probability of achieving a crack-free seal since glass has a similar coefficient of thermal expansion with Pt [146]. This work shows that by graphically analyzing the high frequency impedance data of the two sets, the quality of microelectrode fabrication may be determined for each. For this study, it

is assumed that the glass-insulated microelectrodes exhibit seals with no defects, while the epoxy-insulated microelectrodes exhibit seals with defects, which is consistent with what has been presented in the literature about glass-insulated versus epoxy-insulated microelectrodes [146].

Two sets of microelectrodes were made using 50 μm diameter Pt wire (California Fine wire). One set of Pt wires were secured in glass tubing with an insulating epoxy and one end was polished with AlO_2 sandpapers. The final grit sandpaper corresponded to 0.3 μm roughness. In the other set of electrodes, a glass tube was heated and sealed around the Pt wire. SiC sandpaper was used to polish one end of those samples to a final roughness of 1 μm. The unpolished side of all electrodes were electrically connected to a gold pin connector with silver epoxy.

A Gamry Series G 300 potentiostat was used for performing electrochemical impedance spectroscopy. Impedance responses of the Pt microelectrodes were measured with respect to a Pt counter electrode and Ag/AgCl reference electrode in 0.9% phosphate buffered NaCl (Sigma) at room temperature. The perturbation voltage was 10 mV, the frequency range was 10 kHz to 0.8 Hz, and all experiments were taken at open circuit potential. All experimental data were consistent with the Kramers-Kronig relation as prescribed by Orazem [152].

6.3.1.1 Graphical analysis

This study assumes the model for a blocking system with constant phase element (CPE) behavior, which is commonly represented as a resistor in series with a constant phase element [153] for Pt microelectrodes in saline solution. The equivalent circuit impedance is given as

$$Z = R_e + \frac{1}{(j\omega)^{\alpha} Q}, \tag{6–5}$$

where R_e is the electrolyte resistance, ω is angular frequency, α is a constant less than one, and Q is the CPE coefficient [150, 151]. Following Orazem et al. α may be graphically found by plotting the imaginary part of the impedance as a function

of frequency [133]. In a logarithmic plot, the slope of the impedance data gives the negative value of α. The value of Q is given by [150]

$$Q = \sin\left(\frac{\alpha\pi}{2}\right)\frac{-1}{Z_j\omega^{\alpha}}. \tag{6–6}$$

In References, [149–151], the authors develop a graphical method that elucidates geometry induced artifacts in the impedance spectra for a disc electrode. They introduce a dimensionless frequency K,

$$K = \frac{Q_{\text{eff}}\omega^{\alpha}r_0}{\kappa}, \tag{6–7}$$

where κ is the conductivity of the electrolyte, r_0 is the radius of the disc electrode, and Q_{eff} is a value representing $Q(\omega)$. Plotting the dimensionless imaginary impedance against the dimensionless frequency K in logarithmic scale produces a straight line with slope equal to -1 for a blocking system modeled by Equation (6–5). Their work shows that for frequencies greater than $K = 1$, the impedance is influenced by the current distribution and deviates from the ideal behavior of the impedance. The results give slopes that deviate from -1 at frequencies greater than

$$f_c = \frac{1}{2\pi}\left(\frac{\kappa}{Q_{\text{eff}}r_0}\right)^{1/\alpha}, \tag{6–8}$$

where f_c is the frequency at which $K = 1$. This frequency is inversely proportional to the radius of the electrode and for the case in this study f_c is on the order of 100 kHz, which is beyond the frequency range of interest. Thus, artifacts due to current distribution can be neglected.

The next section will use the graphical method of plotting imaginary impedance versus K to assess the quality of the electrode fabrication. Specifically, this method will be used to rule out any electrodes that have defects which allow the impedance spectra to diverge from ideal behavior, that is a slope of imaginary impedance versus K on a logarithmic plot not equal to -1. Based on results from [147], the physical reason for the defect is an imperfect seal between the metal and insulator.

6.3.2 Quality Control Results and Discussion

Impedance was measured for two sets of electrodes described in Section 6.3.1. Microelectrodes labeled 1a-4a were insulated with glass and polished with SiC sandpaper and exhibit ideal behavior for a blocking electrode. Microelectrodes labeled 1b-3b were insulated with epoxy and polished with AlO_2 sandpaper. These electrodes do not exhibit ideal behavior and have fabrication defects that can be explained with the theory of porous electrodes [137, 139].

6.3.2.1 Ideal behavior

Imaginary impedance versus frequency and Nyquist plots for electrodes 1a-4a are given in Figure 6-6. Results show spectra for four Pt microelectrodes that have little

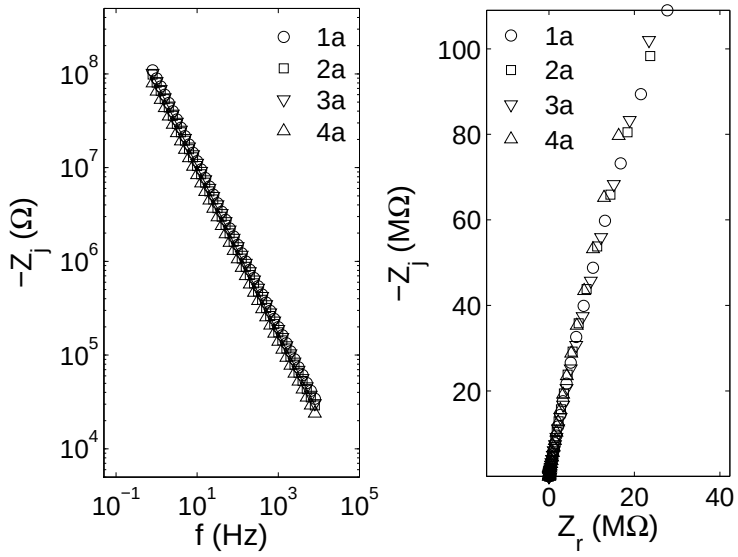

Figure 6-6. (left) Imaginary impedance as a function of frequency of four different Pt microelectrodes insulated in glass and polished with SiC paper. The value of $-\alpha$ corresponding to each electrode is found by calculating the slope of the lines. (right) Nyquist plot of the four Pt microelectrodes.

deviation from each other. The values of α are found by fitting the plots of imaginary impedance versus frequency to straight lines and extracting the slope via the curve fitting tool in Matlab. The CPE coefficient is calculated by Equation (6–6) and plotted in Figure 6-7. Values of α and Q_{eff} used for the calculation of K are given in Table 6-1.

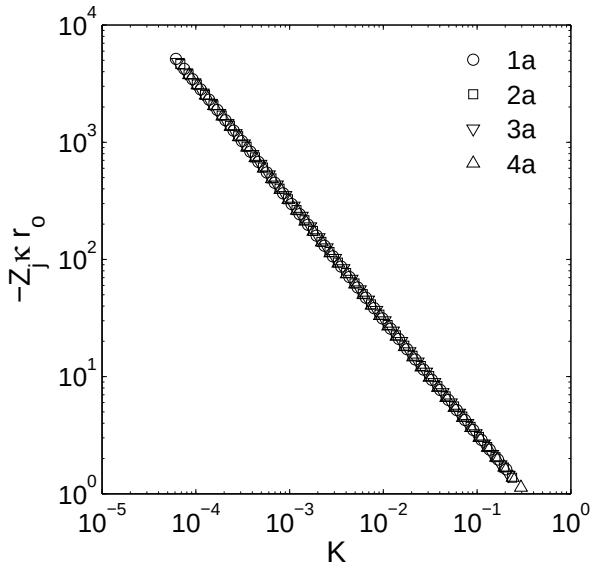

Figure 6-7. CPE coefficient Q as a function of frequency. The dotted lines show the effective values used for calculation of K in equation (6–7).

Table 6-1. Values of α and Q_{eff} for ideal electrodes from Figure 6-6 and Figure 6-7

Glass	α	Q_{eff} / $\Omega^{-1} cm^{-2} s^{\alpha}$
1a	-0.881	1.15×10^{-4}
2a	-0.885	1.27×10^{-4}
3a	-0.882	1.18×10^{-4}
4a	-0.885	1.59×10^{-4}

The dimensionless imaginary impedance as a function of dimensionless frequency K is shown in Figure 6-8 (using a conductivity of 0.19 mS/cm). All impedance data superimpose on the same line as expected for ideally constructed microelectrodes. Figure 6-9 shows the derivative of imaginary impedance with respect to K. Over the measured frequency span, the derivative does not deviate from -1 by more than 5%. This result suggests that any microelectrode showing derivatives that are different from -1 by more than 5% have fabrication defects.

6.3.2.2 Non-ideal behavior

The same method is followed for impedance data of electrodes 1b-3b. From examining the impedance data in Figure 6-10, it is evident that electrode 2b does not

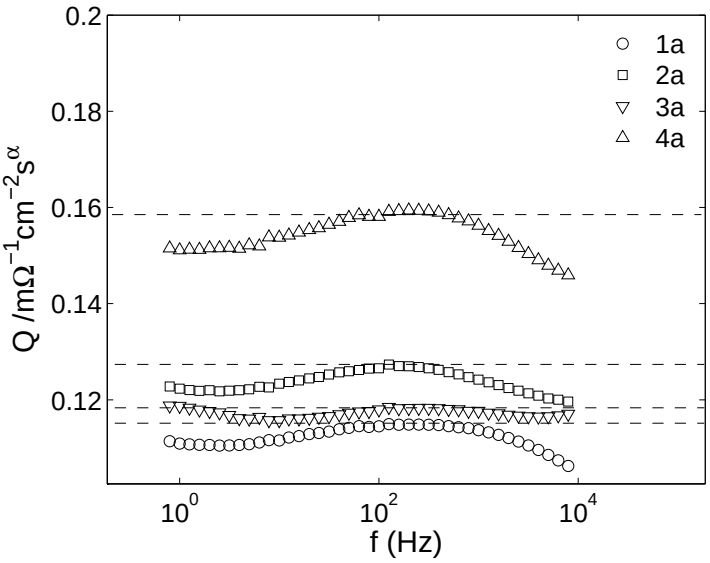

Figure 6-8. Imaginary impedance of the ideal electrodes in dimensionless units with respect to dimensionless frequency K.

show ideal behavior and would be suspect for defects; however, 1b and 3b appear acceptable.

The values for α are found by fitting the impedance spectra in Figure 6-10 to straight lines. Only frequencies higher than 100 Hz were used to calculate α for microelectrode 2b. Values for Q are plotted in Figure 6-11 and values used to calculate K are given in Table 6-2.

Table 6-2. Values of α and Q_{eff} for non-ideal electrodes extracted from Figure 6-10 and Figure 6-11

Glass	α	Q_{eff} / $\Omega^{-1}cm^{-2}s^{\alpha}$
1b	-0.848	8.22×10^{-5}
2b	-0.662	1.53×10^{-4}
3b	-0.766	1.25×10^{-4}

Examining the imaginary impedance as a function of K in Figure 6-12, it is evident that microelectrode 2b does not show ideal behavior. In Figure 6-13, when the derivative of dimensionless imaginary impedance with respect to K is plotted, the variation seen for electrodes 1b-3b is greater than seen for microelectrodes 1a-4a. Thus, it is likely

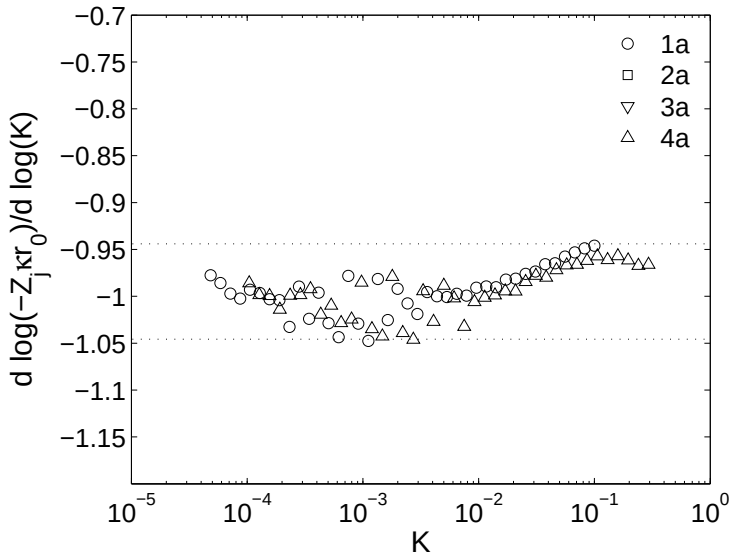

Figure 6-9. Derivative of the logarithm of dimensionless imaginary impedance of the ideal electrodes with respect to log$K$. Almost all data points lie within 5% of -1.

that all three of the epoxy sealed microelectrodes have some fabrication defect and are unsuitable for measurements.

6.3.3 Quality Control Summary

Since transient electrochemical measurements are shown to be sensitive to fabrication defects [147], a graphical analysis of electrochemical impedance data is proposed as a simple method of quality control of microelectrode fabrication. This work analyzed impedance data of a blocking system below the frequency f_c at which geometry induced artifacts arise for microelectrodes. The results suggested that ideally constructed microelectrodes will exhibit a slope of the imaginary impedance as a function of dimensionless frequency K in a logarithmic plot that does not vary from 1 by more than 5%. The proposed method will also work for a reactive system. If a reactive system is used, impedance data corresponding to frequencies greater than the characteristic frequency given by the RC time constant of the double layer capacitance and charge transfer resistance and lower than f_c should be used in the analysis.

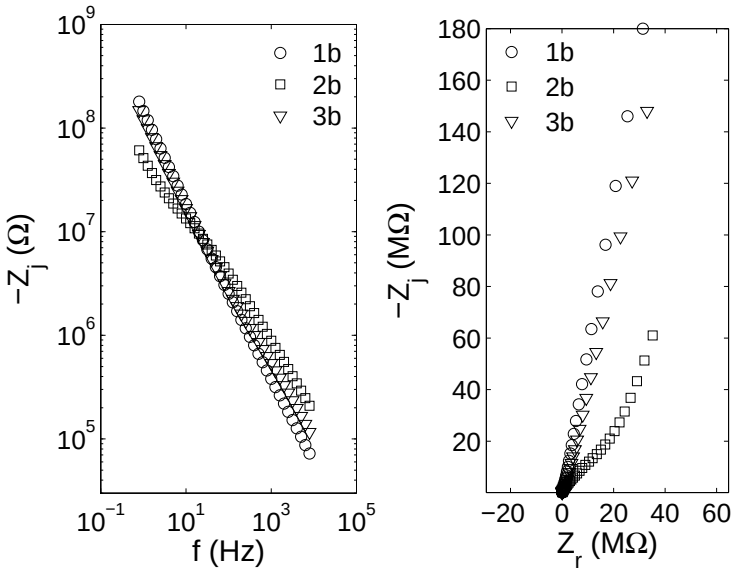

Figure 6-10. (left) Imaginary impedance as a function of frequency of four different Pt microelectrodes insulated in epoxy and polished with AlO_2 paper. The value of $-\alpha$ corresponding to each electrode is found by calculating the slope of the lines. (right) Nyquist plot of the four Pt microelectrodes.

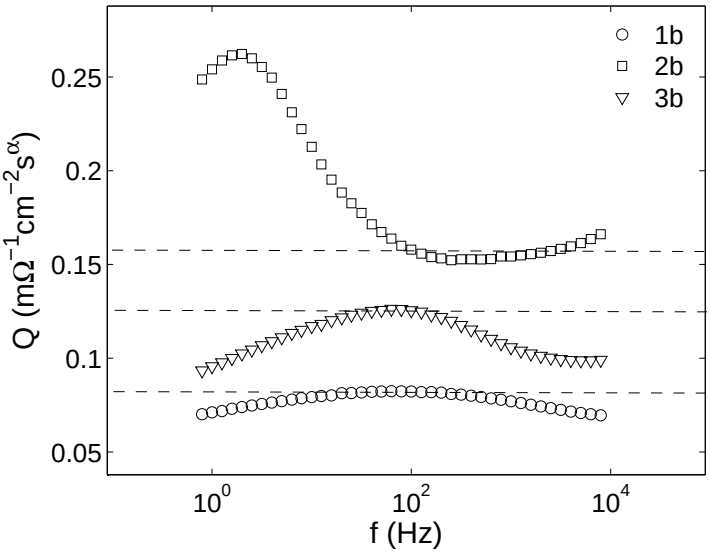

Figure 6-11. CPE coefficient Q of the non-ideal electrodes as a function of frequency. The dotted lines show the effective values used for calculation of K in equation (6–7).

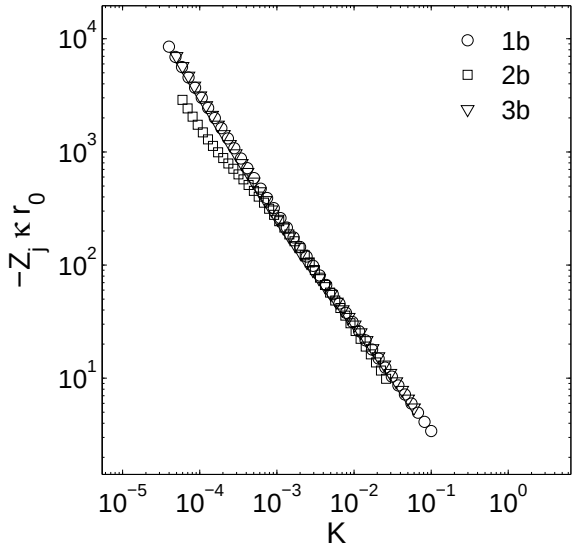

Figure 6-12. Plot of imaginary impedance of the non-ideal electrodes in dimensionless units with respect to dimensionless frequency K.

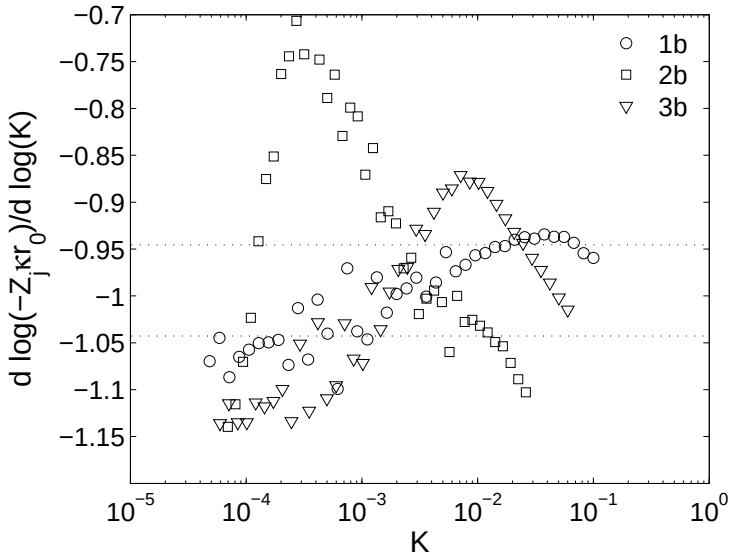

Figure 6-13. Derivative of the logarithm of dimensionless imaginary impedance of the non-ideal electrodes with respect to log$K$. Many data points differ from -1 by more than 5%.

CHAPTER 7
ELECTROCHEMICAL CHARACTERIZATION ELECTRODES: RESULTS

A well controlled *in vitro* study on the corrosion properties of tungsten and platinum microwires in physiological saline solutions is performed to assess the longevity of the wires for use in neural recording microelectrode arrays. Specific materials, instrumentation, and measurement parameters used for the impedance measurements are described first. The results of the electrochemical impedance spectroscopy (EIS) measurements are then presented. Analysis of the measured impedance using the Stern-Geary equation quantifies the rate of tungsten corrosion in biological saline solutions. The analysis of Pourbaix diagrams provides information on the electrochemical reactions occurring on the electrode surfaces. Based on the results, tungsten is not suitable for long-term implant use, while platinum is suitable.

7.1 Materials and Instrumentation

The working electrodes in the EIS measurements were made with tungsten or platinum wires encased in glass or epoxy. The glass insulation process was performed by placing the wires in borosilicate glass tubes and heating the structure in a furnace at a temperature (T=800°C) that softens the glass. Electrodes insulated in epoxy were made by placing the microwire in a glass tube and filling the tube with epoxy resin (Epo-tek 302-3M). With glass or epoxy sealed tightly around the wire, one end-face was polished with SiC sandpapers resulting in a final roughness of 1 μm and the other end is secured to a gold connector with silver epoxy (AbleBond). The quality control method discussed in Section 6.3 was used to identify an ideally fabricated electrode with an adequate seal between the insulation and the electrode. Three working electrodes each were made using 50 μm diameter gold-plated-tungsten, bare-tungsten, and platinum microwires. The gold-plated-tungsten and platinum working electrodes were insulated with glass, and the bare-tungsten electrode was insulated in epoxy because a furnace was not available at that time.

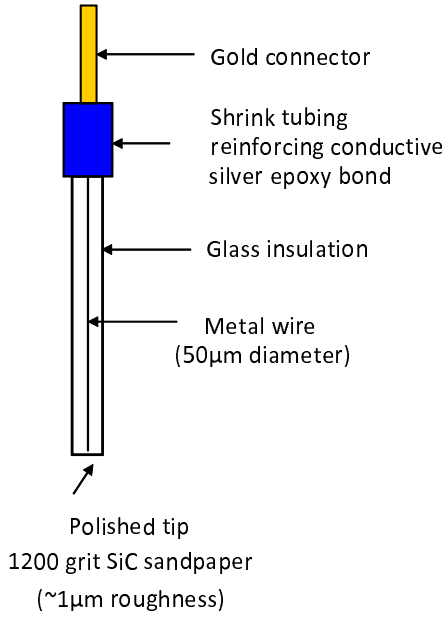

Figure 7-1. Schematic of working electrode for EIS measurements.

The electrolytes used in the EIS measurements were chosen to model the *in vivo* chemistry. They are 0.9% phosphate buffered saline (PBS) for healthy neural tissue and phosphate buffered saline that contains H_2O_2 to simulate tissue undergoing an inflammatory response. Since H_2O_2 is secreted from microglia that surround the implanted microwire electrode, local concentrations are difficult to estimate. Pan et al. and Fonesca et al. used hydrogen peroxide and PBS to assess corrosion of titanium for structural implant materials [105], [106]. They used concentrations that ranged from 10 mM to 100 mM. A concentration of 30 mM H_2O_2 was chosen for this study. A salt mixture (Sigma P-5368) was used to make the PBS with composition given in Table 7-1 and pH of 7.4.

Electrochemical impedance spectroscopy measurements were performed under potentiostatic control using a Gamry 300 G series potentiostat/glavanostat. Cyclic voltammetry was also performed with the Gamry system with voltage sweep rates of 50 and 100 mV/s. A silver/silver chloride reference electrode (BioAnalytical Systems RE-5B) was used in this study. Pt or Ti large area counter electrodes were used for

Table 7-1. Composition of Phosphate Buffered Saline

Chemical Compounds	Concentration (M)
NaCl	0.138
HCl	0.0027
Na_2HPO_4	0.01
KH_2PO_4	0.00176
*H_2O_2	0.03

*Concentration of H_2O_2 for electrolyte including PBS and H_2O_2

measurements in PBS electrolyte and an electrolyte containing PBS and 30 mM H_2O_2, respectively. A Ti counter electrode was used in solutions containing H_2O_2 because Pt was shown to be reactive. The EIS perturbation voltage was 10 mV. The frequency range for all experiments was 0.1 Hz to 20 kHz, and all measurements were taken at the equilibrium, or open circuit potential (OCP). The microelectrodes were polished and thoroughly rinsed in deionized water immediately prior to immersion in the electrolyte. Aa elapsed period of 5 minutes allowed the OCP to stabilize before the impedance measurements were taken.

7.2 Experimental Results

The EIS results for tungsten and platinum microelectrodes immersed in a PBS electrolyte are compared first, followed by the results of tungsten and platinum electrodes in an electrolyte containing PBS and hydrogen peroxide. Images of corroding tungsten microelectrodes in *in vitro* and *in vivo* settings are also given.

7.2.1 EIS of Tungsten and Platinum in Phosphate Buffered Saline

The comparison of the impedance data of platinum and tungsten microelectrodes immersed in a PBS electrolyte are shown in Figure 7-2. The tungsten microelectrodes exhibit reactive behavior since the impedance data for the tungsten microelectrodes show the presence of a resistive pathway at low frequencies (e.g. the impedance data shows a semicircle in the complex-impedance-plane plot). The platinum electrode exhibits blocking or nonreactive behavior since its impedance data trends toward

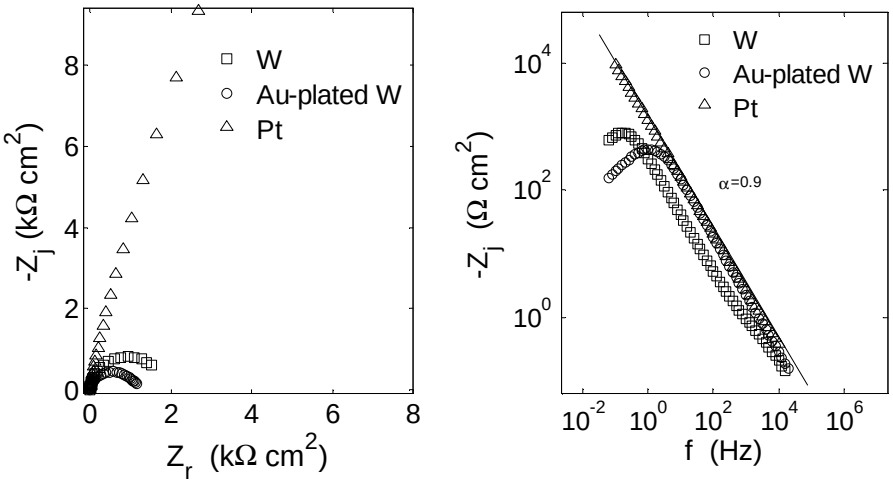

Figure 7-2. Nyquist plot (left) and imaginary impedance as a function of frequency (right) of tungsten and platinum electrodes in PBS.

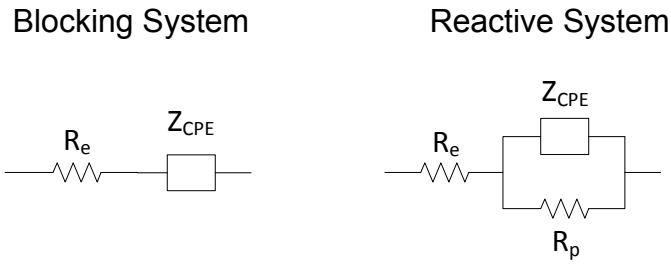

Figure 7-3. Equivalent circuits for blocking and reactive systems [1].

infinity as the frequency decreases. All electrodes show constant phase element (CPE) behavior as evidenced by the slope of the imaginary impedance as a function of frequency differing from negative one (i.e. $\alpha = 0.9$) [133]. The blocking and reactive systems can be modeled with a resistor in series with a constant phase element or the parallel combination of a resistor and constant phase element, respectively, as shown in Figure 7-3 [154]. R_e is the resistance of the electrolyte, R_p is the polarization resistance, and Z_{CPE} is the constant phase element impedance given by Equation 7–1,

$$Z_{cpe} = \frac{1}{(j\omega)^{\alpha} Q}, \tag{7–1}$$

where ω is the frequency, α is a number from 0 to 1, and Q is the CPE coefficient with units $s^{\alpha}/\Omega cm^2$ [134].

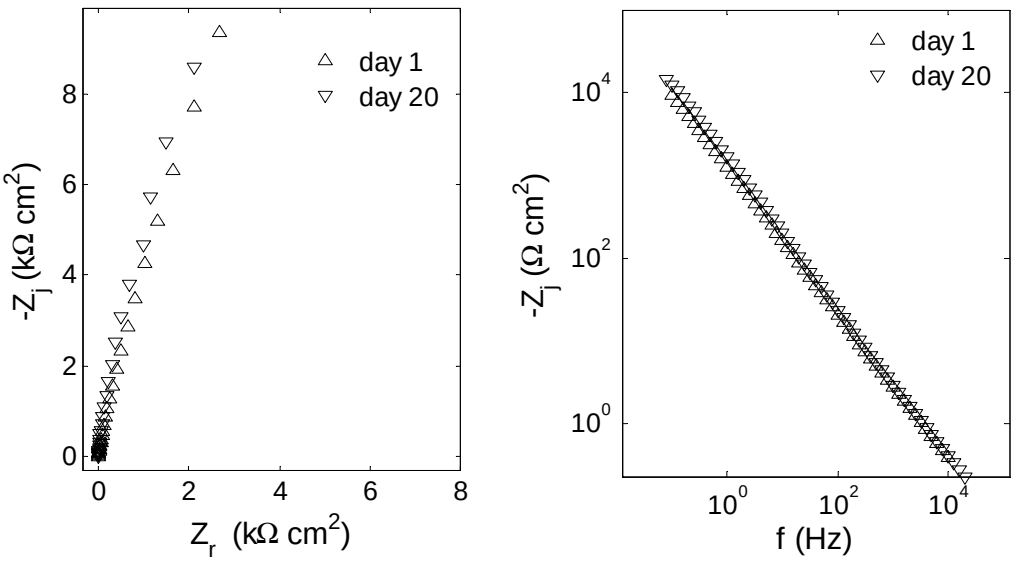

Figure 7-4. Nyquist plot (left) of imaginary impedance as a function of frequency (right) of a platinum electrode in phosphate buffered saline over time.

Impedance measurements taken after long periods of immersion in the electrolyte illustrate the observation of the nonreactive nature of platinum and give insight into the reactive nature of the tungsten electrode. Figure 7-4 shows the impedance spectra of platinum microelectrodes after 20 days in the PBS solution still exhibiting blocking, or unreactive, behavior. Figure 7-5 shows EIS results for a gold-plated tungsten microelectrode in PBS over 15 days. The progression of the semi-circular curves show a reactive system that changes over time. The change in the magnitude of the impedance over time is an indication that the electrode surface is being modified.

The dominant cathodic reaction on the tungsten electrode is found by testing the system reactivity to the oxygen concentration. EIS results showing the dependence of the faradaic reaction to the concentration of oxygen is presented in Figure 7-6. The concentration of oxygen was decreased by bubbling N_2 into the solution. After one hour of O_2 displacement via bubbling, the EIS measurement results show that the polarization resistance increases with decreased O_2 content. These results suggest that the reduction of oxygen is the rate-limiting cathodic reaction at the electrode surface.

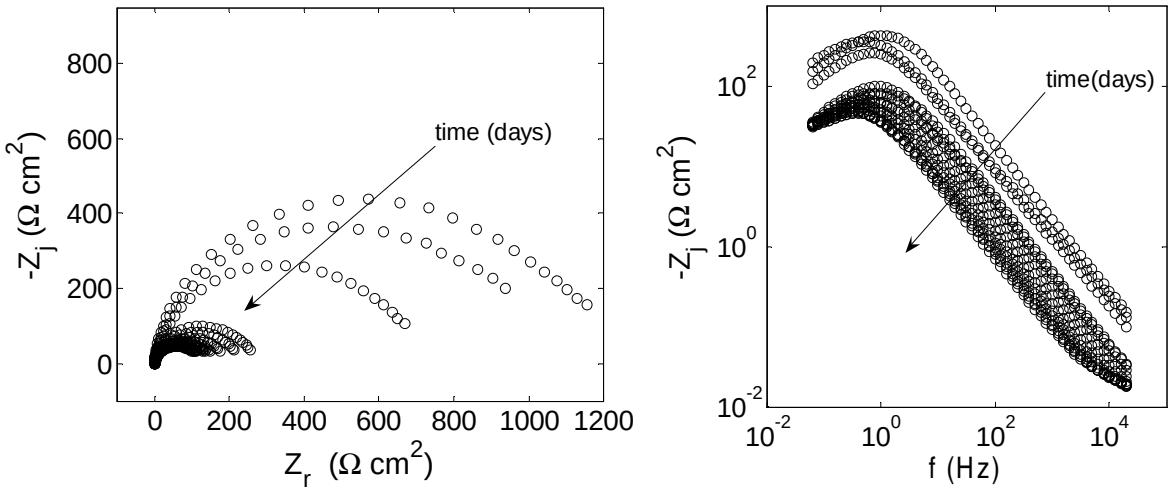

Figure 7-5. Nyquist plot (left) and imaginary impedance as a function of frequency (right) of a gold-plated tungsten electrode in phosphate buffered saline over 15 days.

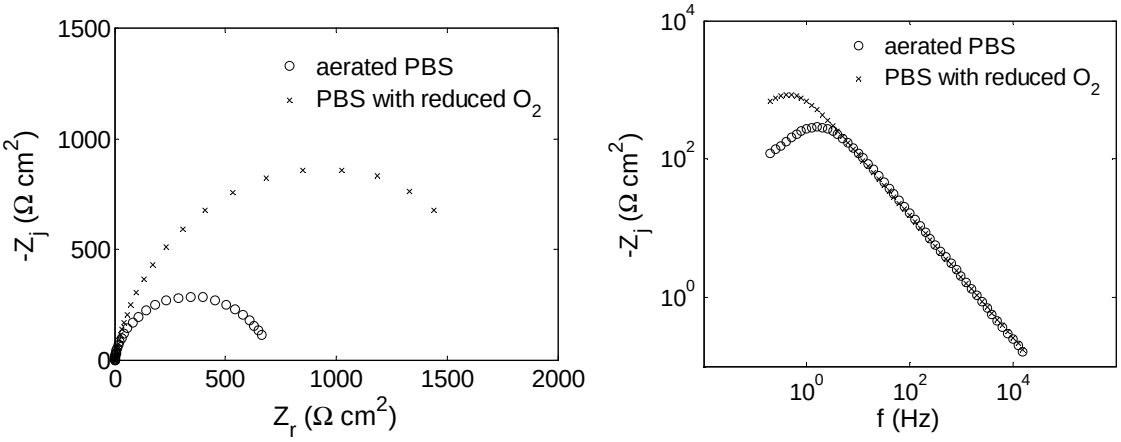

Figure 7-6. Nyquist plot (left) and imaginary impedance as a function of frequency (right) of tungsten electrodes in PBS showing dependence on O_2 concentration.

7.2.2 EIS of Tungsten and Platinum in Phosphate Buffered Saline and Hydrogen Peroxide

The oxidizing effect of H_2O_2 allows another cathodic pathway for charge transfer via the reduction of H_2O_2. EIS results are again used to experimentally ascertain the presence of a faradaic reaction in both systems. Figure 7-7 shows that faradaic reactions are occurring on both the gold-plated tungsten and platinum electrodes when H_2O_2 is present. The presence of a resistive pathway at the dc limit is evident by the semicircular shapes in Figure 7-7.

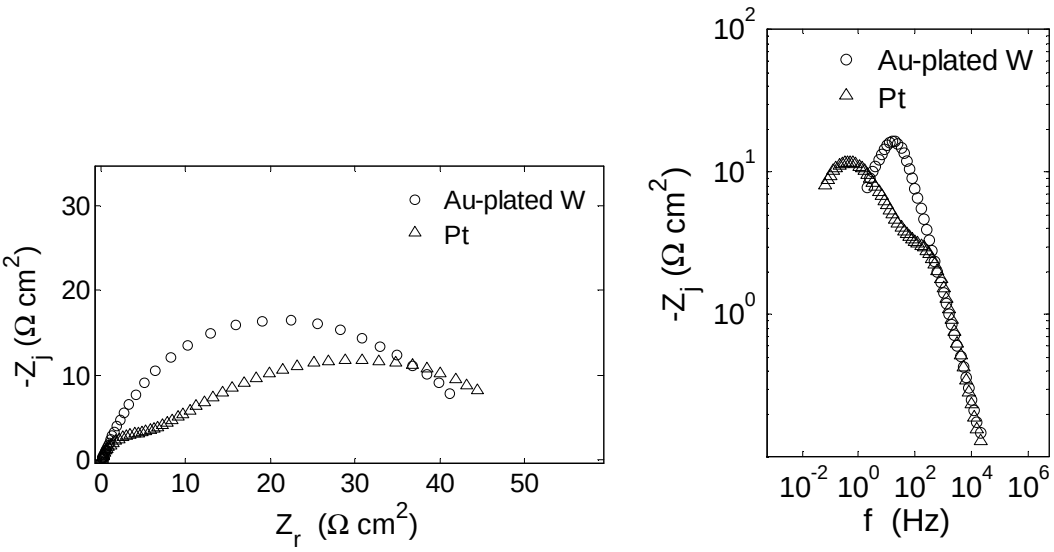

Figure 7-7. Nyquist plot (left) and imaginary impedance as a function of frequency (right) of a platinum and gold-plated tungsten electrode in PBS plus H_2O_2 showing reactive behavior.

7.2.3 Images of Tungsten Corrosion

The presence of tungsten corrosion is verified and unique trends are established by examining optical photographs taken over time. Figure 7-8 shows a polished surface of a tungsten-only electrode compared to the surface after 23 days of immersion in PBS. The surface after 23 days is porous and roughened. Over a shorter time interval, Figure 7-9 shows the state of six different gold-plated tungsten electrodes before and after immersion in PBS from one to six days. The top pictures correspond to the before state and the bottom pictures correspond to the after state. After one day in saline, the surface looked roughened as compared to the previous state. After two days in saline, there was a circular section in the center of the electrode that was depressed approximately 0.5 μm, which is out of focus in the photograph. A similar trend is seen for the other electrodes left in saline for longer periods. Each displays a circular depression in the center of the electrode that grows deeper with time. For the electrode left in saline for five days, the center was depressed approximately 4 μm and was porous. The picture of the electrode left in saline for six days shows that the entire tungsten

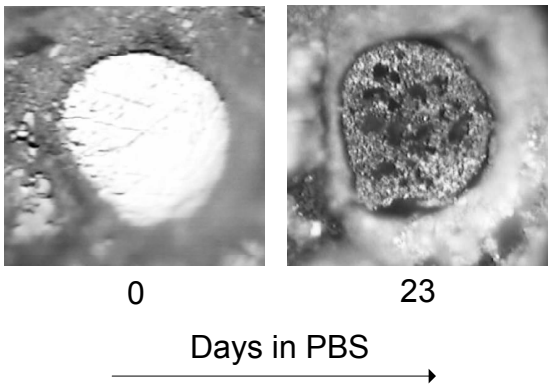

Figure 7-8. Photographs of a tungsten electrode before and after immersion in PBS for the specified period of time.

surface is recessed from the polished surface with the center even more depressed. These photographs suggest that the gold-plated-tungsten electrodes experienced uniform corrosion that was dependent on the microstructure of the drawn tungsten wires. Over an even shorter time period, Figure 7-10 shows the change of the surface of one gold-plated tungsten electrode in PBS and H_2O_2 over 24 hours. After one hour in the electrolyte, recesses were seen around the edges of the gold-tungsten interface as well as a roughened tungsten surface. The recesses on the perimeter of the electrode are what is expected for a primary current distribution on the disc electrode surface, where the current density is the highest at the perimeter [36]. As time progressed, the recesses expanded inward to the center of the electrode and after 24 hours, the bulk of the tungsten was recessed on the order of 10 μm below the original surface. These photographs suggest a much higher corrosion rate for gold-plated tungsten in saline solutions containing H_2O_2 than what was seen for the other two cases without H_2O_2.

7.3 Analysis and Discussion

This section analyzes faradaic reactions occurring on the electrodes and discusses their implications on *in vivo* applications. Analysis using Pourbaix diagrams provides information on possible electrochemical reactions. The Pourbaix diagram shows the potential at which chemical and electrochemical reactions may occur on an electrode surface in a specific electrolyte as a function of pH [155]. The thermodynamic stability

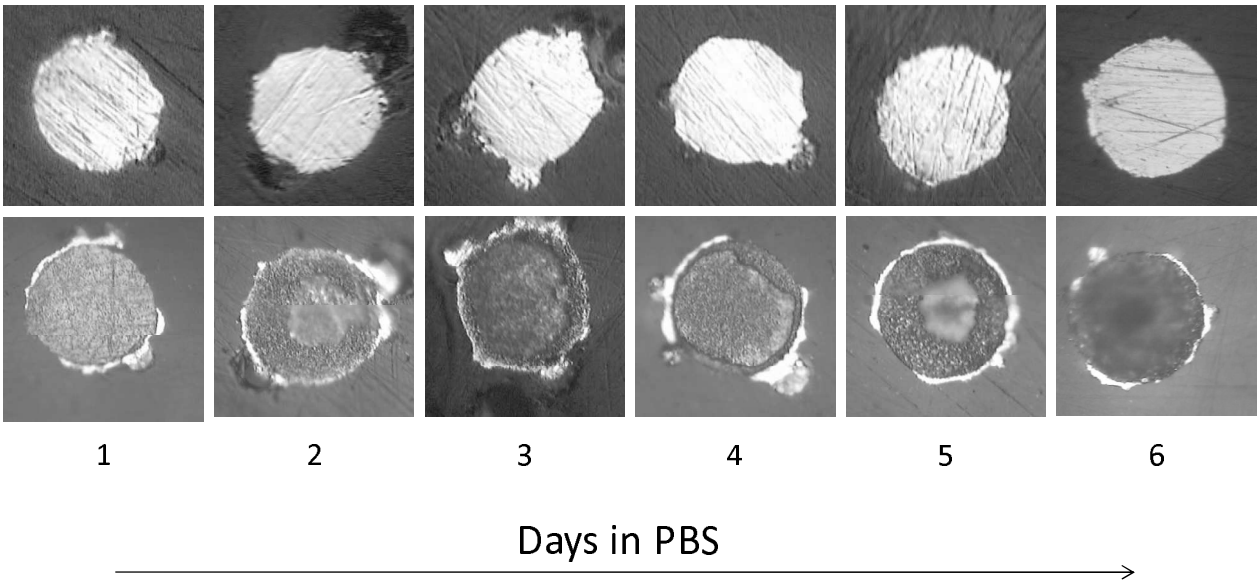

Figure 7-9. Photographs of gold-plated tungsten electrodes before (top) and after (bottom) immersion in PBS for the specified period of time.

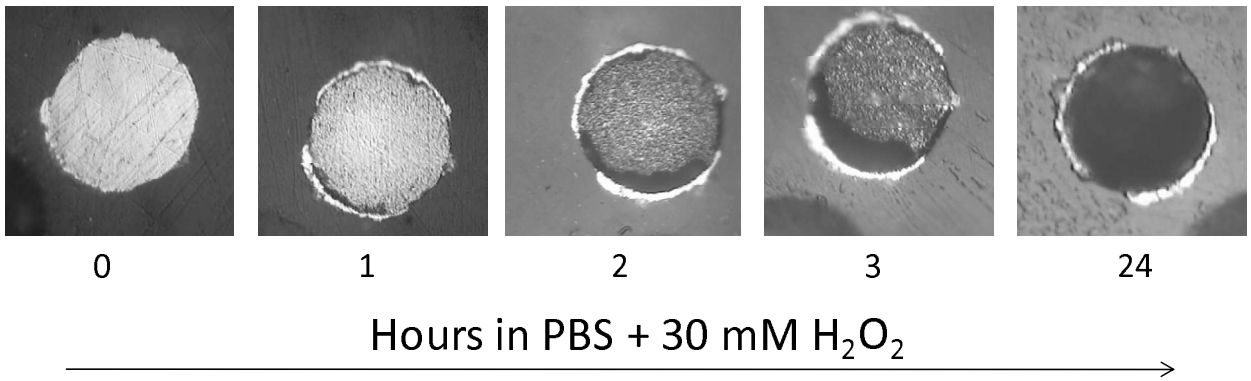

Figure 7-10. Photographs of a gold-plated tungsten electrodes before and after immersion in an electrolyte containing PBS and H_2O_2 for the specified period of time.

of chemical species at various potential and pH ranges may be ascertained from the diagram. Also, the voltages for hydrogen and oxygen evolution reactions are commonly shown on the diagrams. In the Pourbaix diagrams created for this study, all potentials are referenced to the standard hydrogen electrode (SHE). Thus, a calculation must be performed to convert the potentials measured in this study to be with respect to the SHE. The Pourbaix diagrams shown in this study are generated by a computer program (CorrosionAnalyzer 1.3 Revision 1.3.33 by OLI Systems Inc).

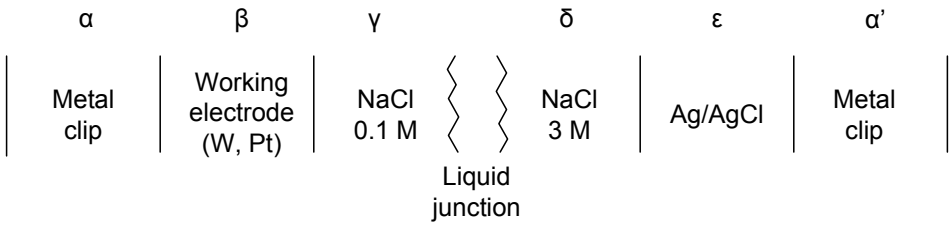

Figure 7-11. Schematic representation of electrochemical cell.

7.3.1 Calculation of Open Circuit Potential Referred to SHE

The open circuit potential (OPC) is the potential measured by the potentiostat of the electrochemical cell established by the working and the reference electrodes under zero bias or electrical equilibrium conditions. The Pourbaix diagrams show voltages with respect to the standard hydrogen electrode (SHE), but a silver/silver chloride reference electrode is used in the OCP measurements. Thus, the OCP data must be converted to reference the SHE. A schematic of the electrochemical cell is depicted in Figure 7-11.

A liquid-junction potential exists between the electrolyte in the reference electrode and the electrolyte of the working electrode. The liquid-junction potential $\Phi^{\delta} - \Phi^{\gamma}$ must be accounted for in the conversion. As an approximate solution, the Henderson formula (Equation 7–2) may be used even though the correct concentration profile is not defined.

$$\Phi^{\delta} - \Phi^{\gamma} = -\frac{RT}{F} A \frac{\ln(B^{\delta}/B^{\gamma})}{B^{\delta} - B^{\gamma}}, \tag{7–2}$$

where

$$A = \sum_i z_i u_i (c_i^{\delta} - c_i^{\gamma}), \; B^{\delta} = \sum_i z_i^2 u_i c_i^{\delta}, \; B^{\gamma} = \sum_i z_i^2 u_i c_i^{\gamma}, \tag{7–3}$$

and z_i, u_i, and c_i are the charge number, mobility, and molar concentration of ionic species i, respectively [36]. The potential of a silver/silver chloride electrode with reference to the SHE assuming the concentration can be considered the same as the activity is given as

$$U' = U^{\ominus} - \frac{RT}{F} \ln c_{Cl^-}^{\delta}, \tag{7–4}$$

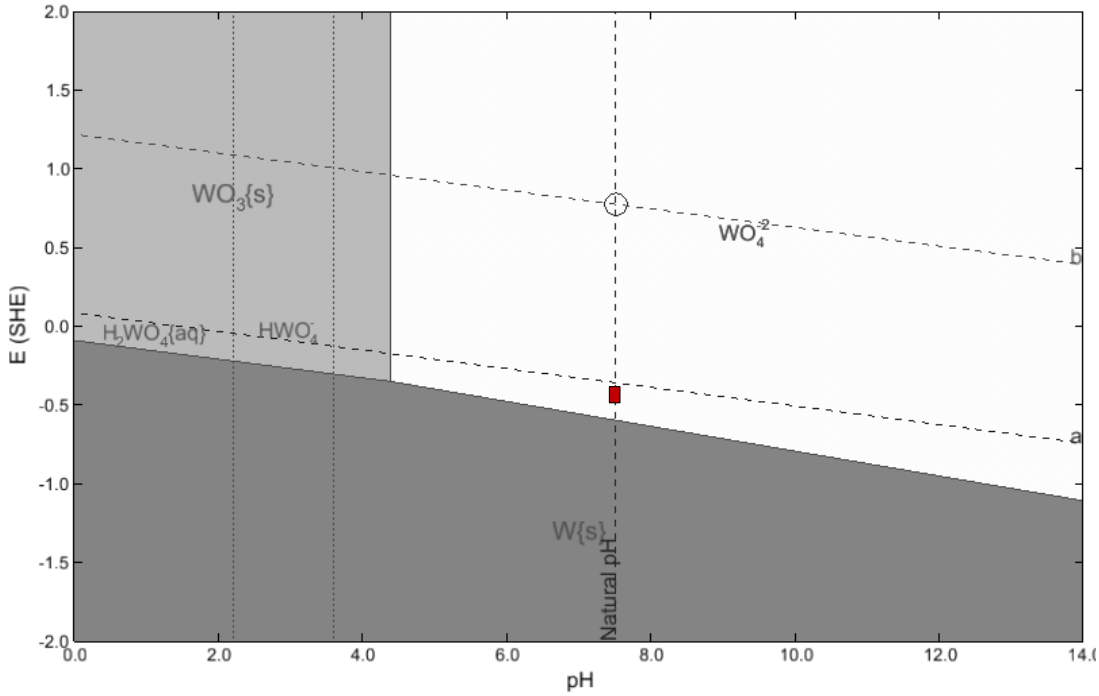

Figure 7-12. Pourbaix diagram of tungsten in phosphate buffered saline. The box shows range of open circuit potential over 15 days. The diagrams are generated by CorrosionAnalyzer 1.3 Revision 1.3.33 by OLI Systems Inc.

where $U^{\ominus} = 0.222$ V is the standard electrode potential at 25°C. The electrode potential corrected for the liquid-junction potential can be expressed as

$$U'' = U - U' - (\Phi^{\delta} - \Phi^{\gamma}), \tag{7–5}$$

where U is the measured open circuit potential. For the concentrations used in this study $U' = 0.194$ V and $\Phi^{\delta} - \Phi^{\gamma} = -0.016$ V.

7.3.2 Possible Electrochemical Reactions on Tungsten

Pourbaix diagrams are used to predict possible reactions on tungsten at the open circuit potential. The Pourbaix diagram given in Figure 7-12 shows the thermodynamic stability of tungsten in PBS. The diagonal lines labeled a and b correspond to the limits of the stability of water. Above line a, oxidation of water (i.e. oxygen evolution), is possible and below line b, reduction of water (i.e. hydrogen evolution), is possible. Between those lines, water is stable. The vertical dashed line designates the natural pH

Table 7-2. Species considered in calculation of the Pourbaix diagram presented as Figure 7-12.

Aqueous Phase	Solid Phase	Vapor Phase
Water	Pentasodium triphosphorous decaoxide	Water
Chloride ion(-1)	Pentasodium triphosphorous decaoxide hexahydrate	Hydrogen
Dihydrogen orthophosphate(V) ion(-1)	Phosphorus pentoxide (dimer)	Hydrogen chloride
Dihydrogen pyrophosphate(V) ion(-2)	Potassium chloride	Oxygen
Hydrogen	Potassium dihydrogen orthophosphate(V)	
Hydrogen chloride	Potassium hydrogen orthophosphate(V) hexahydrate	
Hydrogen ion(+1)	Potassium hydrogen orthophosphate(V) trihydrate	
Hydrogen orthophosphate(V) ion (-2)	Potassium hydrogen phosphate(V)	
Hydrogen pyrophosphate(V) ion(-3)	Potassium hydroxide	
Hydrogen tungstate(VI) ion(-1)	Potassium hydroxide dihydrate	
Hydroxide ion(-1)	Potassium hydroxide monohydrate	
Orthophosphoric acid	Potassium orthophosphate(V)	
Oxygen	Potassium orthophosphate(V) heptahydrate	
Phosphate ion(-3)	Potassium orthophosphate(V) trihydrate	
Potassium chloride	Potassium tungstate(VI)	
Potassium ion(+1)	Sodium chloride	
Pyrophosphate ion(-4)	Sodium dihydrogen orthophosphate dihydrate	
Pyrophosphoric(V) acid	Sodium dihydrogen orthophosphate monohydrate	
Sodium ion(+1)	Sodium dihydrogen orthoporthohosphate	
Trihydrogen pyrophosphate(V) ion(-1)	Sodium hydrogen orthophosphate	
Tungsten(VI) tetraoxide ion(-2)	Sodium hydrogen orthophosphate dihydrate	
Tungstic(VI) acid	Sodium hydrogen orthophosphate dodecahydrate	
	Sodium hydrogen orthophosphate heptahydrate	
	Sodium hydroxide	
	Sodium hydroxide monohydrate	
	Sodium orthohosphate	
	Sodium orthophosphate hexahydrate	
	Sodium orthophosphate hydroxide dodecahydrate	
	Sodium orthophosphate monohydrate	
	Sodium orthophosphate octahydrate	
	Sodium pyrophosphate decahydrate	
	Sodium tungstate(VI)	
	Sodium tungstate(VI) dihydrate	
	Tungsten	
	Tungsten(VI) oxide	

of the electrolyte at 7.4. The box shows the range of the measured values of the open circuit potential for a gold-plated tungsten electrode over 15 days in solution. A list of all chemical species considered in the formation of the Pourbaix diagram for tungsten in PBS are given in Table 7-2. The diagram shows that the tungstic ion WO_4^{2-} is stable at the OCP and that corrosion reactions are possible in this system since the box is in the white (WO_4^{2-}) area. The overall anodic electrochemical reaction producing the tungstic ion is given by Equation 7–6 [101, 155]. Possible cathodic reactions are reduction of water and oxygen given by Equation 7–8 and Equation 7–7.

$$W + 4H_2O \rightarrow WO_4^{2-} + 8H^+ + 6e^- \tag{7–6}$$

$$O_2 + 2H_2O + 4e^- \rightarrow 4OH^- \tag{7–7}$$

$$2H_2O + 2e^- \rightarrow H_2 + 2OH^- \quad (7\text{–}8)$$

However, the rate-limiting effect of oxygen seen in Figure 7-6 suggests that the reduction of oxygen is the dominant cathodic reaction given by Equation 7–7.

Another possible chemical reaction is the dissolution of a tungsten oxide. Lillard et al. showed that tungsten exposed to air has a native oxide WO_3 via surface-enhanced-Raman spectroscopy [97]. The Pourbaix diagram suggests that WO_3 dissolves at the cell equilibrium potential (0.4 V vs. SHE) and 7.4 pH as given by Equation 7–9.

$$WO_3 + H_2O \rightarrow WO_4^{2-} + 2H^+ \quad (7\text{–}9)$$

Therefore, even if an oxide layer exists on the tungsten surface that could inhibit the dissolution of the tungsten, eventually the oxide will be dissolved and expose the tungsten surface.

The addition of hydrogen peroxide to the PBS allows another cathodic reaction, the reduction of H_2O_2, to occur on the tungsten electrode surfaces. A Pourbaix diagram showing the OCP range for a gold-plated tungsten electrode in an electrolyte containing PBS and 30 mM of H_2O_2 is given in Figure 7-13. The chemical species considered for the Pourbaix diagram are the same as listed in Table 7-2 with the addition of H_2O_2. The regions of stability of H_2O_2 given by Pourbaix [155] are overlayed on the diagram. Below the line labeled 1, reduction of H_2O_2 is possible and above line 2, oxidation of H_2O_2 is possible. Thus, for an electrochemical system containing a tungsten electrode in PBS and H_2O_2, the possible anodic reaction is given by Equation 7–6 and possible cathodic reactions are given by Equation 7–7 and Equation 7–10.

$$H_2O_2 + 2H^+ + 2e^- \rightarrow 2H_2O \quad (7\text{–}10)$$

Gold-tungsten galvanic couple: The gold-plated tungsten electrode constitutes a galvanic couple. Hence the gold has a significant role in the reactivity of the system. Gold is stable at the equilibrium potential and pH of the system [155] and thus will

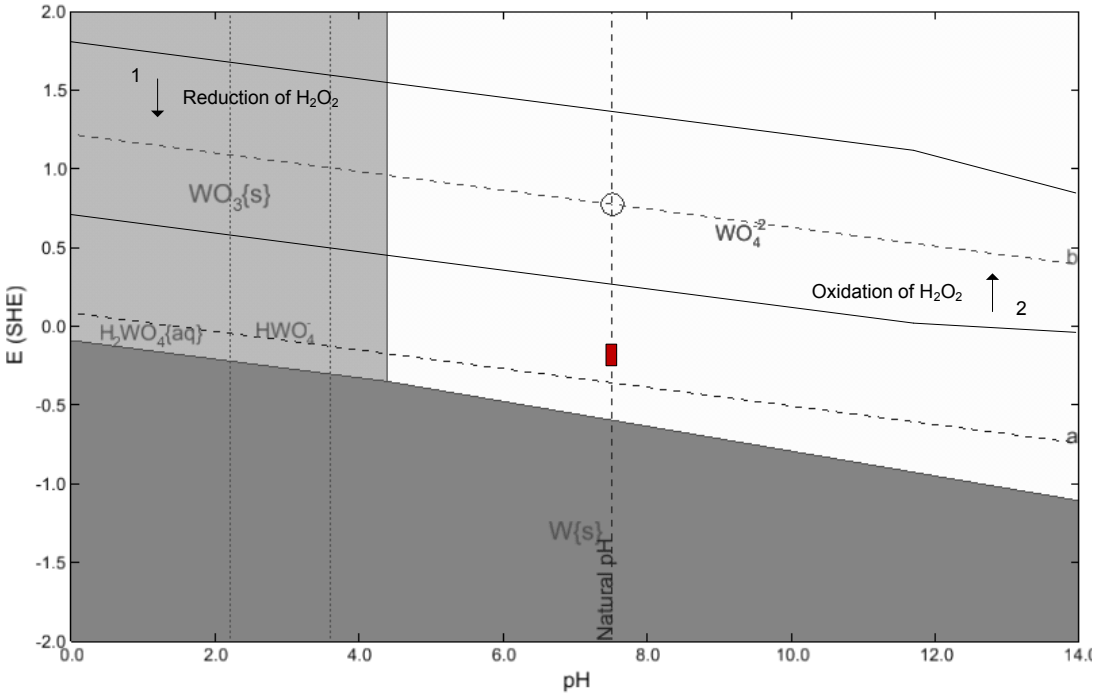

Figure 7-13. Pourbaix diagram of tungsten in an electrolyte containing phosphate buffered saline and 30 mM H_2O_2. The box shows range of open circuit potential over two days. The diagrams are generated by CorrosionAnalyzer 1.3 Revision 1.3.33 by OLI Systems Inc.

not corrode; however, it provides an exclusive surface for the cathodic reaction and increases the corrosion rate of the tungsten[51]. As the tungsten corrodes, gold that was plated on the outer surface of the tungsten becomes further exposed. The surface area of the gold increases, thereby increasing the exchange current for the cathodic reaction, and consequently the anodic reaction rate must increase to compensate, since the net current at equilibrium must be zero. This process may be modeled using mixed potential theory. A diagram showing a proposed mixed potential theory is given in Figure 7-14. For simplicity, only the dominant reactions (Equation 7–6 and Equation 7–7) are included. It is assumed that the oxidation reaction occurs only on the tungsten (anode), and the reduction reaction occurs only on the gold (cathode). Figure 7-14 shows a hypothetical Evan's diagram consisting of the logarithm of current as a function of potential. As the exchange current increases for the increasing cathode surface area for the reduction of oxygen, a new corrosion current is established as

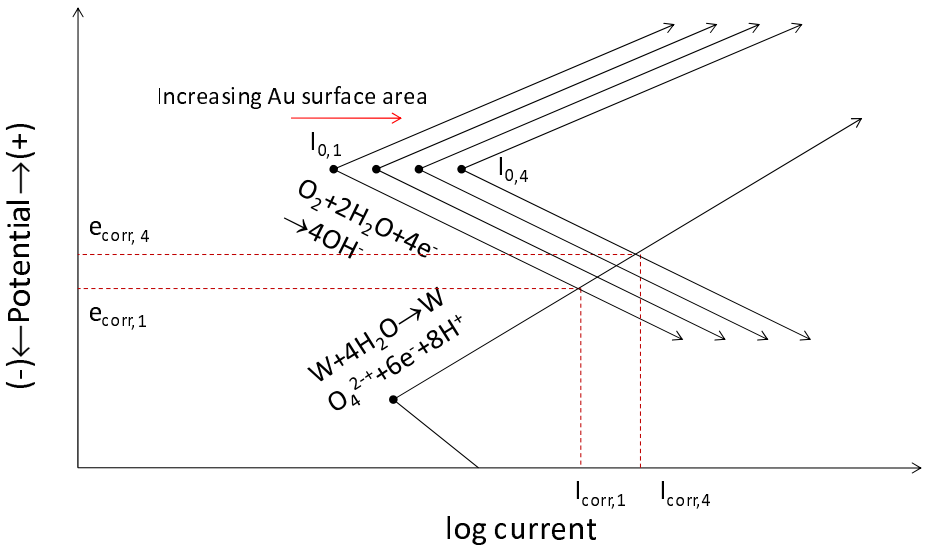

Figure 7-14. Effect of increased cathode surface area on galvanic interaction of tungsten and gold.

shown by the shift from $I_{corr,1}$ to $I_{corr,4}$. Assuming the tungsten area stays constant, the resulting corrosion rate for the tungsten is thereby increased. Also, the potential of the system increases to more noble values.

Measurements of OCP over time verify the proposed effect of the galvanic couple. Figure 7-15 displays the measured OCP over time for the gold-plated-tungsten electrodes and tungsten electrodes in PBS. The gold-plated-tungsten system shows a nonlinear trend toward more positive potentials compared to the tungsten system, which shows a more stable OCP.

In summary, two factors control the corrosion rate of tungsten in biological saline solutions. It was shown via the dependence on the concentration of oxygen that the corrosion of tungsten is rate-limited by the cathodic reaction. Moreover, the corrosion rate of the tungsten is increased by the gold-tungsten galvanic couple existing in microelectrodes used for intracortical applications. The rates of tungsten corrosion in three different systems are quantified next.

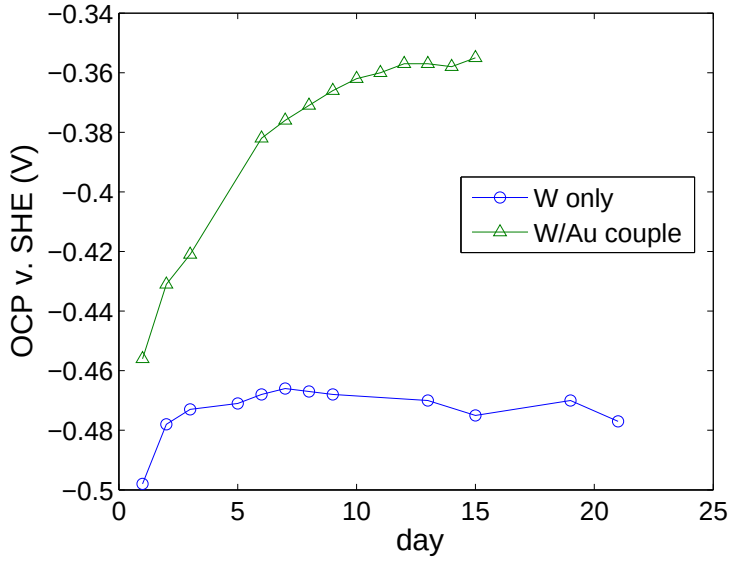

Figure 7-15. OCP over time for gold-plated tungsten and tungsten electrodes in PBS.

7.3.3 Rate of Tungsten Corrosion

Various methods exist to estimate the corrosion rate of a metal. Typical methods include exposure testing where weight loss is measured, Tafel extrapolation, and estimation of the polarization resistance via polarization methods or electrochemical impedance spectroscopy.[51] The small size of our sample electrode does not lend itself to weight loss measurements and Tafel extrapolation is easily confounded by the presence of multiple reactions [51]. Extrapolation of the polarization resistance from EIS data rather than data from polarization measurements is preferred in the system under study since relatively shorter times are required for the impedance measurements.

7.3.3.1 Calculation of Corrosion Rate

When using EIS, the polarization resistance may be estimated by subtracting the low frequency asymptotic value from the high frequency asymptotic value on a Nyquist plot. The corrosion rate is calculated from the polarization resistance via the Stern-Geary equation, Equation 7–11[51]. The polarization resistance is inversely

related to the corrosion current density via

$$R_p = \frac{\beta_a \beta_c}{2.3 i_{corr}(\beta_a + \beta_c)}; \tag{7–11}$$

where β_a and β_c are the anodic and cathodic Tafel constants, respectively, and i_{corr} is the corrosion current density [51]. The corrosion current density is related to the corrosion rate as follows.

$$r_{corr} = \frac{i_{corr} a}{nF}, \tag{7–12}$$

where a is the atomic weight, n is the oxidation number, and F is Faraday's constant. Equation 7–12 gives a corrosion rate in terms of mass loss per unit area per time. To obtain a rate in terms of units of penetration per time, Equation 7–12 is divided by the density of the metal to achieve millimeters per year (mm/yr), for example.

If the Tafel constants are not known, the corrosion rate may still be approximated. The Tafel constants range between 0.06 V and 0.12 V for β_a and between 0.12 and infinity for β_c [51]. If the most extreme values are used, the corrosion rate varies by only a factor of two.

7.3.3.2 Comparison of Corrosion Rates

The corrosion rates of the three tungsten systems (tungsten in PBS, gold-plated tungsten in PBS, and gold-plated tungsten in PBS and 30 mM H_2O_2) were quantified by extrapolating the polarization resistance from EIS data. Complex nonlinear least squares regression was used to fit the experimental data to the measurement model given in Equation 7–13.[135]

$$Z = R_0 + \sum_{k=1}^{k} \frac{R_k}{1 + j\omega\tau_k} \tag{7–13}$$

The measurement model consists of a resistor, R_0, modeling the electrolyte resistance, in series with k Voigt elements, where a Voigt element is a capacitor in parallel with a resistor that has a characteristic time constant $\tau_k = 2\pi RC$. Figure 7-16 shows the Nyquist plots of the impedance response of the three systems. All electrodes were

polished immediately prior to submersion in the electrolyte and allowed to achieve a steady state via a settling period of five minutes. Assuming there is no oxide on the the surface of the electrodes due to adequate polishing, the corresponding corrosion rate for each system is calculated and given in Table 7-3. A range of values for the corrosion rates is given because of the uncertainty of the Tafel constants. The impedance results

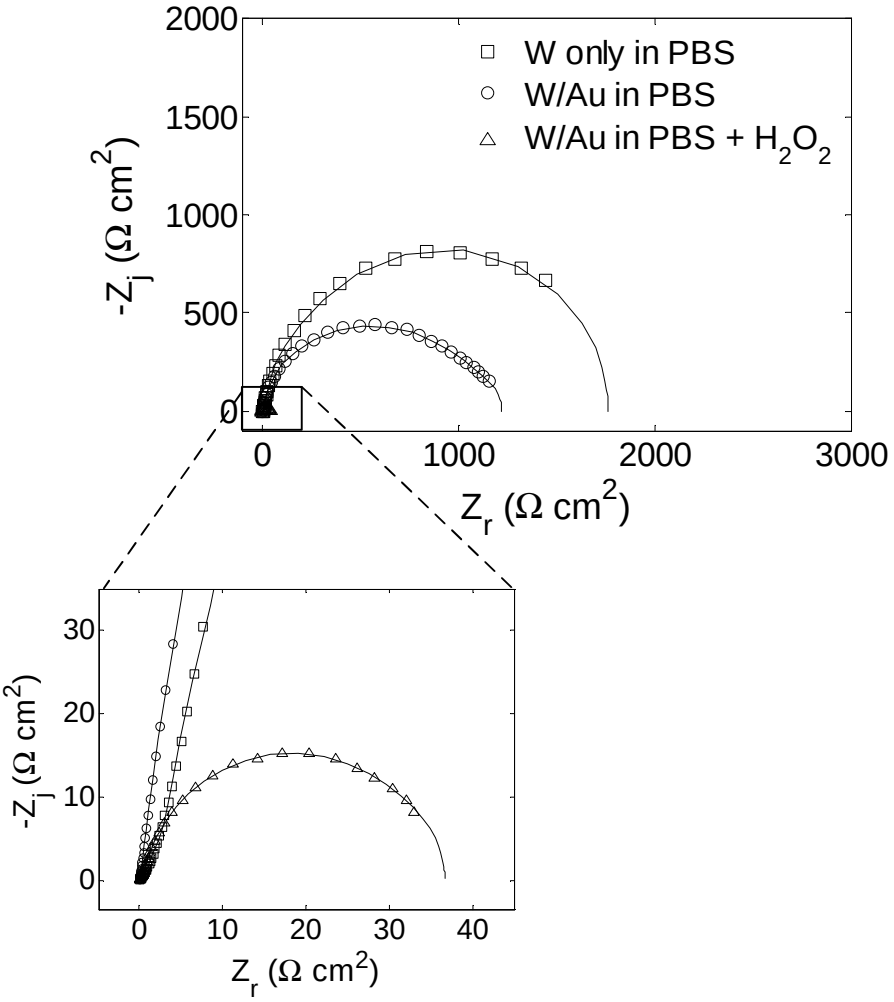

Figure 7-16. Nyquist plots used for calculation of the polarization resistance, R_p, for three tungsten systems. The solid lines show the regression results using Equation 7–13.

predict that the corrosion of tungsten in aerated PBS will corrode at a rate of 200-500 μm/yr. The galvanic couple of the gold-plated tungsten microwire acts to increase the corrosion rate of the system in PBS alone to 300-700 μm/yr. However, the corrosion

Table 7-3. Corrosion rates for tungsten

System	R_p (MΩ cm^2)	r$_{corr}$ (mm/yr)
W in PBS	1700	$0.2 \leq r_{corr} \geq 0.5$
W/Au in PBS	1200	$0.3 \leq r_{corr} \geq 0.7$
W/Au in PBS + H_2O_2	40	$10 \leq r_{corr} \geq 20$

rates predicted for the gold-plated tungsten systems are for the initial electrode area; the rates could increase as more of the gold surface becomes exposed as described previously. The addition of 30 mM of hydrogen peroxide to the PBS significantly increases the corrosion rate of a gold-plated tungsten electrode to 10,000-20,000 μm/yr. Previous EIS results showed that the corrosion mechanisms are rate limited by the cathodic reaction. Thus, the corrosion rates for each system are dependent on the concentrations of oxygen or hydrogen peroxide, respectively, and may also be controlled by diffusion of the species.

7.3.4 Possible Electrochemical Reactions on Platinum

As shown in Figure 7-7, a faradaic reaction occurs on platinum electrodes in saline solutions containing hydrogen peroxide. It is important to know what electrochemical reactions could be occurring on the platinum electrode when implanted. A Pourbaix diagram considering the chemical species in Table 7-4 was generated for platinum in an electrolyte of PBS and 30 mM H_2O_2 and is shown in Figure 7-17. Curves representing the stability of H_2O_2 are superimposed on the Pourbaix diagram. At potentials below curve 1, the reduction of H_2O_2 is possible and above curve 2, the oxidation of H_2O_2 is possible [155]. In the region where the two reactions overlap, hydrogen peroxide may dissociate into water on a platinum surface. The box shows the range of measured OCP for three platinum electrodes. Thus, the Pourbaix diagram shows that reduction of H_2O_2 is possible as a cathodic reaction in this system. The Pourbaix diagram does not, however, suggest possible corresponding anodic reactions. Brummer et al. propose hydrogen adsorption as possible charge transfer pathways [156]. The assumed anodic

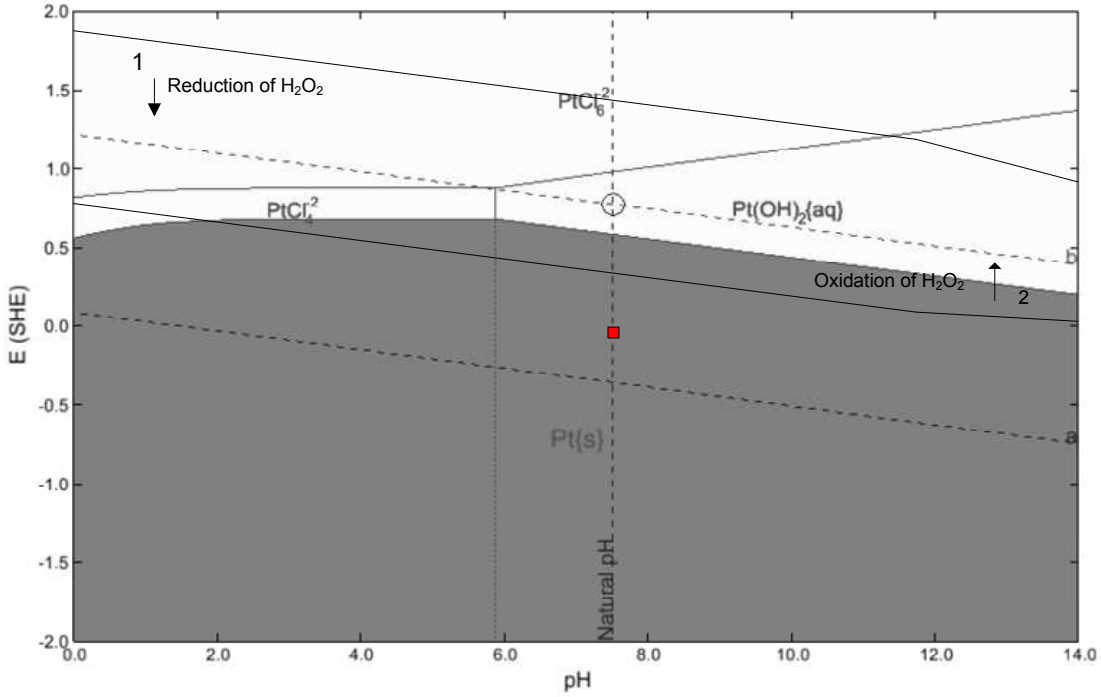

Figure 7-17. Pourbaix diagram of platinum in phosphate buffered saline and 30 mM hydrogen peroxide. The red box shows range of open circuit potential. The diagrams are generated by CorrosionAnalyzer 1.3 Revision 1.3.33 by OLI Systems Inc.

and cathodic reactions are given respectively by Equation 7–14 and Equation 7–10

$$\text{Pt - H} \rightarrow \text{Pt} + \text{H}^+ + e^-. \tag{7–14}$$

Cyclic voltammetry was used to further analyze the electrochemical reactions at the platinum surface. Cyclic voltammograms of the platinum electrodes are shown for scan rates of 50 and 100 mV/s. By comparing these results with literature [157, 158], the two peaks labeled H_w and H_s are inferred to be the weak and strong hydrogen adsorption peaks. Thus, hydrogen adsorption is further substantiated by Figure 7-18, as the hydrogen adsorption peaks occur near the open circuit potential (0.045 V versus SHE) of the cell.

Hydrogen adsorption and hydrogen peroxide reduction, Equation 7–14 and Equation 7–10, have no adverse effect on the platinum surface, hence it is expected to

Table 7-4. Species considered in calculation of the Pourbaix diagram presented as Figure 7-17.

Aqueous Phase	**Solid Phase**	**Vapor Phase**
Water	Pentasodium triphosphorous decaoxide	Water
Chloride ion(-1)	Pentasodium triphosphorous decaoxide hexahydrate	Hydrogen
Dihydrogen orthophosphate(V) ion(-1)	Phosphorus pentoxide (dimer)	Hydrogen chloride
Dihydrogen pyrophosphate(V) ion(-2)	Platinum	Hydrogen peroxide
Hydrogen	Platinum(II) chloride	Oxygen
Hydrogen chloride	Platinum(II) hydroxide	
Hydrogen ion(+1)	Platinum(IV) chloride	
Hydrogen orthophosphate(V) ion (-2)	Potassium chloride	
Hydrogen peroxide	Potassium dihydrogen orthophosphate(V)	
Hydrogen peroxide ion(-1)	Potassium hydrogen orthophosphate(V) hexahydrate	
Hydrogen pyrophosphate(V) ion(-3)	Potassium hydrogen orthophosphate(V) trihydrate	
Hydroxide ion(-1)	Potassium hydrogen phosphate(V)	
Orthophosphoric acid	Potassium hydroxide	
Oxygen	Potassium hydroxide dihydrate	
Phosphate ion(-3)	Potassium hydroxide monohydrate	
Platinum ion(+2)	Potassium orthophosphate(V)	
Platinum ion(+4)	Potassium orthophosphate(V) heptahydrate	
Platinum(II) chloride	Potassium orthophosphate(V) trihydrate	
Platinum(II) hydroxide	Sodium chloride	
Platinum(II) monochloride ion(+1)	Sodium dihydrogen orthophosphate dihydrate	
Platinum(II) monohydroxide ion(+1)	Sodium dihydrogen orthophosphate monohydrate	
Platinum(II) tetrachloride ion(-2)	Sodium dihydrogen orthoporthohosphate	
Platinum(II) trichloride ion(-1)	Sodium hexachloroplatinate(IV) hexahydrate	
Platinum(IV) chloride	Sodium hydrogen orthophosphate	
Platinum(IV) dichloride ion(+2)	Sodium hydrogen orthophosphate dihydrate	
Platinum(IV) hexachloride ion(-2)	Sodium hydrogen orthophosphate dodecahydrate	
Platinum(IV) monochloride ion(+3)	Sodium hydrogen orthophosphate heptahydrate	
Platinum(IV) pentachloride ion(-1)	Sodium hydroxide	
Platinum(IV) trichloride ion(+1)	Sodium hydroxide monohydrate	
Potassium chloride	Sodium orthohosphate	
Potassium ion(+1)	Sodium orthophosphate hexahydrate	
Pyrophosphate ion(-4)	Sodium orthophosphate hydroxide dodecahydrate	
Pyrophosphoric(V) acid	Sodium orthophosphate monohydrate	
Sodium ion(+1)	Sodium orthophosphate octahydrate	
Trihydrogen pyrophosphate(V) ion(-1)	Sodium pyrophosphate decahydrate	

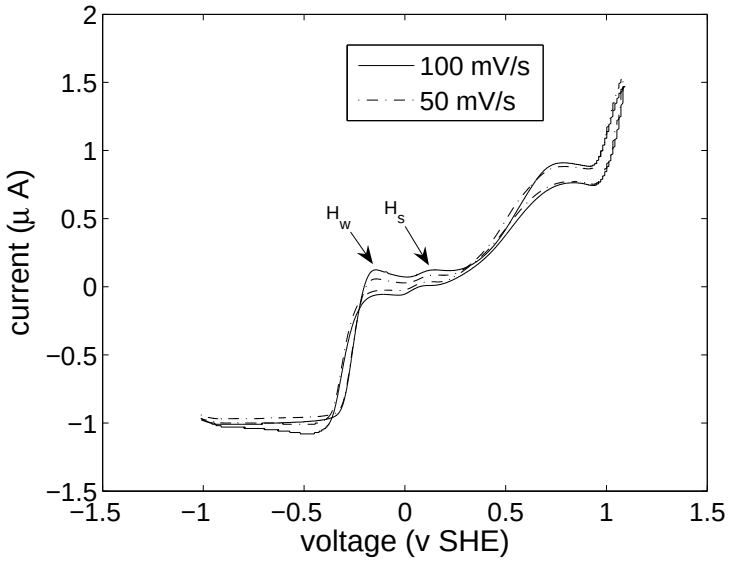

Figure 7-18. Cyclic voltammogram of a platinum electrode in an electrolyte containing PBS and 30 mM H_2O_2

be stable. Effects on the brain tissue are most likely benign. The reduction of hydrogen peroxide to water may even lessen degradation to nearby cells or other parts of the implanted microelectrode (e.g. the polymer insulation). Therefore, these results confirm that platinum as a recording site is a good choice in biological solutions.

7.4 Conclusions

A strategy for ascertaining the nature of charge transfer including which faradaic reactions are occurring on tungsten and platinum microelectrodes in physiologic environments has been established. Graphical analysis of EIS data was used to ascertain the presence of faradaic reactions and extrapolation of the polarization resistance from the impedance data was used to estimate the corrosion rate of tungsten microwires. Analysis of Pourbaix diagrams for each system at experimentally measured open-circuit potentials corroborated the presence of tungsten corrosion and platinum stability and provided possible electrochemical reactions for each system.

Tungsten was shown to corrode in physiological saline environments. The dominant electrochemical reactions on tungsten in PBS are oxidation of tungsten to the tungstic ion and reduction of oxygen, and the dominant reactions in PBS with H_2O_2 are oxidation of tungsten to the tungstic ion and reduction of H_2O_2 to water. The estimated corrosion rates for a bare-tungsten microelectrode and a gold-plated tungsten microelectrode in physiological PBS are 300-700 μm/yr. The corrosion rate of a gold-plated tungsten microelectrode in an electrolyte containing PBS and 30 mM H_2O_2 is 10,000-20,000 μm/yr. Thus, depending on the concentration of H_2O_2 encountered by the microelectrode *in vivo*, the corrosion rate could vary by two orders of magnitude. These results most likely convey the worst-case scenario. Since it was found that the corrosion rate was limited by the rate of the dominant cathodic reaction, the concentration of the reactive species, O_2 or H_2O_2, play a major role. The concentration of dissolved oxygen in the PBS used in the *in vitro* experiments is determined by the partial pressure of oxygen in the air (150 mmHg). In comparison,

the partial pressure of oxygen in the extracellular fluid of the cortex is between 20 and 35 mmHg [159, 160]. Also, as evidenced in the SEM images of the implanted tungsten microwire, the biological film that forms on the electrode surface may act to impede diffusion of chemical species and effectively control the corrosion rate. The corrosion rate for *in vivo* situations may be estimated by the measurement of the recess depth of the tungsten microwires on the UF microelectrode array used in the *in vivo* study. As stated in Section 5.6.2, the average depth that the tungsten surface was recessed from the original surface after an 87 day implant period was 24 μm. The corrosion rate in an *in vivo* setting is then estimated to be approximately 100 μm/yr, which is of the same order of magnitude as the *in vitro* estimation of tungsten corrosion rate of 300-700 μm/yr. The corrosion rate in the *in vivo* setting is less than in the *in vitro* setting because of decreased diffusion due to the presence of a biological film and lower concentration of available oxygen in the brain as compared to the air. Nonetheless, these results suggest that tungsten should not be used in long-term implants.

Besides the possibility of local toxicity due to diffusion of tungstic ions into the cortex, the corrosion of the tungsten electrodes may impede successful long-term recording. It has been shown that a microelectrode must be placed less than 200 μm from the cell body to record the action potential of a neuron [19]. Over time, corrosion could distance the recording surface from the neuron such that the action potential could not be measured. Also, as the tungsten microwire corrodes, a hollow tube made of the insulation and possibly gold plating is formed. This tube could provide a reservoir for cellular build-up that would hinder the diffusion of ionic species and effectively increase the impedance at the electrode/electrolyte interface, which would ultimately decrease the magnitude of the measured action potential. Thus, based on the results, after only one year, the magnitude of the action potential on a tungsten electrode should be greatly attenuated.

Platinum was shown to be a much better choice for intracortical microelectrodes. Platinum is effectively unreactive in phosphate buffered saline solutions and although a faradic response was seen in solution containing hydrogen peroxide, the electrochemical reactions, reduction of H_2O_2 and hydrogen-atom plating, should have less adverse effects on long-term recording. However, the effect of local changes in the pH due to irreversible electrochemical reactions has not been considered in this study.

CHAPTER 8
SUMMARY AND CONCLUSION

Engineering efforts have the potential to make rehabilitation for people suffering from severe motor impairment possible. Neuroprostheses that incorporate brain-machine interfaces are technologies being developed for such problems. One integral component in a brain-machine interface is a reliable and effective recording system. The research presented in this document is part of a larger project (Florida Wireless Integrated Recording Electrode (FWIRE)) that addresses the engineering challenge of an implantable recording system. This work provides an electrode and packaging foundation for future generations of the FWIRE device for cortical recording applications. The specific contributions of this work include the design and fabrication of an implantable polyimide-based microelectrode platform integrated with an amplifier IC and full characterization of the device including analysis of *in vivo* recording performance and *in vitro* corrosion assessment of the tungsten microelectrodes. This chapter summarizes the knowledge gained from the studies and provides suggestions for future research.

8.1 Summary of the UF-Microelectrode Array

The work presented in Chapters 4 and 5 was the first step in building a fully-implantable wireless microelectrode array. Based on the review of existing intracortical microelectrode array designs, a design including a micromachined polymer platform and hybrid-packaging of microwire electrodes and ICs was chosen. The flexible polyimide platform connects the electrode array to the electronics and external connector and allows out-of-plane bending such that the electrode array may be implanted into the cortex while the electronics reside on the top of the skull. The placement of interface electronics on the skull, away from the implanted electrodes, makes power constraints on the interface electronics less restrictive because tissue heating is less of a concern. The flexible connection also reduces the transfer of strain to the implanted electrodes from

movement of the electronics platform. Hybrid-packaging of the microwire electrodes allows for a relatively simple process flow and adaptability of other microwire materials or microelectrode array constructs. The flexibility of the UF microelectrode array design, both in form and function, provides advantages over existing microelectrode array designs.

Bench-top results of the UF microelectrode array showed performance suitable for *in vivo* recording. An average impedance of 50 kΩ at 1 kHz was measured for the tungsten microwire electrodes. The noise floor of the microelectrode array, only, was less than 1 μV_{rms}, and the noise floor of the microelectrode-amplifier system was approximately 3.5 μV_{rms} for a frequency range of 500 Hz to 6 kHz. The noise floor of the microelectrode-amplifier system was statistically similar to the noise floor of a commercial microwire array system (Tucker Davis Technologies). The electrode-amplifier system was able to record and amplify accurately and as expected; its transfer function and impulse response showed a linear system able to accurately measure small signal waveforms representative of action potentials.

The *in vivo* testing of the UF microelectrode array also showed adequate recording performance. The acute recording results of the microelectrode array without the hybrid-packaged amplifier gave high signal to noise ratios ($\sim$7 or 17 dB). The acute results of the microelectrode-amplifier system also showed high signal to noise ratios ($\sim$12 or 21 dB) and relatively low noise ($\sim$4.5 μV_{rms}). The recording results of the microelectrode-amplifier system over a 42 day implant period did not have high signal to noise ratios (on average the SNR was 4 or 12 dB); however, the percentage of active electrodes over the implant duration stayed constant at 88% and 1 to 3 independent neurons were measured on each active channel. Moreover, the same neurons were able to be consistently measured over the implant duration. Termination of the implanted system was due to inconsistent recordings after the 42 day period and inspection after explantation showed that delamination of the polyimide had occurred on one side of the

device. Provisions that will encapsulate the device in a biocompatible silicone elastomer will prevent delamination in future generations.

8.2 Summary of the Electrochemical Analysis

Charge transfer via electrochemical reactions must not be overlooked in chronic recording devices. Most of the literature that considers electrochemical interactions on electrodes used *in vivo* is for stimulation applications. Little emphasis is given on the presence of electrochemical reactions in electrodes used for non-stimulating applications (i.e. recording). Since no current is being injected into the system, it is true that no electrochemical reactions are forced, however; even under electrical equilibrium conditions faradaic charge transfer may exist. If electrochemical reactions are thermodynamically stable at the steady-state potential and pH, then they will persist and corrosion could occur.

A method to ascertain not only the presence of electrochemical reactions at equilibrium, but which reactions are occurring on the electrodes was presented. The method entailed analysis of Pourbaix diagrams, which requires measurement of the open circuit potential, and EIS on ideal samples of the recording-site material. The corrosion of tungsten-microwire electrodes used for intracortical recording applications was analyzed and compared to results for platinum electrodes. Two electrolytes modeling the chemistry of extracellular fluid in the brain in the absence and presence of an inflammatory reaction were investigated for the *in vitro* electrochemical analysis: 0.9% phosphate buffered saline (PBS) and 0.9% PBS containing 30 mM hydrogen peroxide. The oxidation and reduction reactions responsible for corrosion were found by measurement of the open-circuit potential and analysis of Pourbaix diagrams. The corrosion rate was estimated from the polarization resistance, which was extrapolated from the electrochemical impedance spectroscopy data. The results showed that tungsten microwires with or without gold plating in an electrolyte of PBS have a corrosion rates of 300-700 μm/yr. The corrosion rate for gold-plated tungsten

microwires in an electrolyte containing PBS and 30 mM H_2O_2 was accelerated to 10,000-20,000 μm/yr. In comparison, the extent of corrosion of the gold-plated tungsten microwires used in the *in vivo* characterization of the UF microelectrode array was 24 μm, on average, after 87 days implanted. This result corresponds to a corrosion rate of 100 μm/yr, which is in agreement with the results of the *in vitro* study since they over-predict the corrosion rate because neither inhibited diffusion due to the biological film nor the decreased value of oxygen concentration in the brain are accounted for. Moreover, the magnitude of the measured extracellular potential is highly dependent on the position of the electrode [33]. The corrosion rate of tungsten is of concern for a long-term implant, since the active tungsten electrode surface will most likely recede out of range of recording from a neuron after a few years due to corrosion. Platinum was unreactive in solutions of PBS and reactive in solutions of PBS and hydrogen peroxide. The reactivity in solutions containing hydrogen peroxide consisted of hydrogen-atom plating and reduction of H_2O_2, which did not adversely affect the platinum surface nor introduce unwanted species into the electrolyte.

Also, it was found that impedance spectra of the microelectrodes are dependent on the quality of the seal of the insulator to the electrode. Artifacts due to an imperfect insulator seal obscured the impedance response and made characterization of the interface difficult. This work presented a quality control method via graphical analysis of electrochemical impedance spectroscopy data. By comparing the impedance to ideal electrode behavior, the quality of the microelectrode-to-insulation was assessed.

8.3 Suggestions for Future Work

Due to the cumbersome method of hybrid-packaging the ICs to the existing substrate and subsequent poor yield, an altered fabrication process is needed that will allow sequential testing of the packaging steps. It is suggested that the microelectrodes be integrated to a polyimide-based cable as before, but the platform for the electronics be made separately on top of a silicon or pyrex wafer for mechanical support. Similar

fabrication steps using ploymide micromachining and thin film deposition may still be used for the platform for the electronics. Then, the cable integrated with the electrodes can be bonded to the electronics platform. This method allows easier testing of the electronics before the electrodes are secured. Also, the quality of the flip-chip bonds have the potential to be assessed if the platform for the electronics is separated from the electrodes.

Tungsten should not be used in future designs because of its susceptibility to corrosion. The advantages of using tungsten wire for intracortical microelectrodes are because it is rigid enough to be implanted without buckling and it can be manually positioned easily without bending, making fabrication of the arrays possible. However, other metals could have similar characteristics. To insure probe insertion into the brain tissue without buckling or bending, the insertion force must be less than the critical loading force for a given electrode. The critical loading force may be derived using Euler-Bernoulli beam theory. The critical loading force is expressed in Equation 8–1 for a cylindrical column that is clamped on one side and pinned at the other.

$$F_{cr} = \frac{20.19EI}{L^2}, \tag{8–1}$$

where E is Young's modulus and I is the area moment of inertia, and L is the length of the column [161]. Table 8-1 shows the Young's modulus and critical loading force for 50 μm diameter tungsten, platinum, iridium, and platinum-iridium (80% Pt, 20% Ir) microwires that are 3 mm long. Literature prescribes an insertion force on the order of

Table 8-1. Critical Loading Force for Metal Microwires

Microwire Material	E (GPa)	F_{cr} (mN)
Tungsten	411	283
Platinum	168	116
Iridium	528	363
Platinum-Iridium (80%/20%)	198	136

1 mN into the sub-dural cortex for electrodes comparable to the size of the electrodes in

this study [162, 163]. The results in Table 8-1 suggest that all metals listed would have sufficient material strength for insertion into the cortex as their critical loading force is two orders of magnitude higher than what is needed for insertion. Thus, a metal other than tungsten should be used for the next generation of devices.

Platinum-iridium is more rigid than platinum and may be a better choice for the UF microelectrode array in terms of mechanical assembly. Its electrochemical characteristics were not formally explored in this study; however, preliminary experiments suggest that it will behave much like platinum. The Pourbaix diagrams for Ir and Pt show no reactions at open circuit potentials measured for the Pt-Ir electrode [155].

The electrochemical assessment of microelectrodes is not easily performed *in vivo*, thus electrolytes that mimic what is seen *in vivo* are needed. Future electrochemical assessment of other recording-site materials should include hydrogen peroxide since it was shown to make appreciable differences in the cases of tungsten and platinum. The corrosion rate of the tungsten increased by two orders of magnitude in the presence of H_2O_2 and elicited faradaic reactions on the platinum electrode. In the platinum case, the faradaic reaction did not corrode the electrode nor introduce unwanted electrochemical by-products in the solution. Instead, reduction of hydrogen peroxide to water resulted. The choice of metals that are electrochemically active but not corrosive could be chosen to lessen cellular damage by reactive oxygen species. It is also advised to perform an *in vivo* study of the electrochemistry at metal microelectrodes to confirm that small amounts of hydrogen peroxide added to PBS is a good model for the extracellular chemistry during an immune response.

REFERENCES

[1] M. E. Orazem and B. Tribollet, *Electrochemical Impedance Spectroscopy*. Hoboken, NJ: John Wiley and Sons, Inc., 2008.

[2] "Paralysis resource center," World Wide Web, http://www.paralysis.org/site/c.erJMJUOxFmH/b.1169107/k.BE3A/Home.htm, 2008.

[3] "Epilepsy foundation," World Wide Web, http://www.epilepsyfoundation.org/about/statistics.cfm, 2009.

[4] E. C. Leuthardt, S. Gerwin, D. Moran, and J. Ojemann, "The emerging world of motor neuroprosthetics: A neurosurgical perspective," *Neurosurgery*, vol. 59, no. 1, 2006.

[5] F. Mussa-Ivaldi and L. Miller, "Brain-macine interfaces: commputational demands and clinical needs meet basic neuroscience," *Trends in Neuroscience*, vol. 26, no. 6, pp. 329–334, 2003.

[6] M. Hodaie, R. Wennberg, J. Dostrovsky, and A. Lozano, "Chronic anterior thalamus stimulation for intractable epilepsy," *Epilepsia*, vol. 43, no. 6, pp. 603–608, 2002.

[7] E. Hauerman, "The deadly five," *Popular Science*, vol. October, pp. 47–49, 2007.

[8] G. Mone, "Happiness is a warm electrode," *Popular Science*, vol. October, pp. 57–61, 2007.

[9] D. Tweney, "Dean kamen's robot arm grabs more publicity," World Wide Web, http://blog.wired.com/gadgets/2008/05/dean-kamens-rob.html, 2008.

[10] A. Schwartz, X. T. Cui, D. Weber, and D. Moran, "Brain-controlled interfaces: Movement restoration with neural prosthetics," *Neuron*, vol. 52, pp. 205–220, 2006.

[11] J. K. Chapin, K. A. Moxon, R. S. Markowitz, and M. A. L. Nicolelis, "Real-time control of a robot arm using simultaneously recorded neurons in the motor cortex," vol. 2, no. 7, pp. 664–670, 1999.

[12] J. Wessberg, C. Stambaugh, J. Krallk, P. Beck, M. Laubach, J. Chapin, J. Kim, S. Biggs, M. Srinlvasan, and M. Nicolelis, "Real-time prediction of hand trajectory by ensenbles of cortical neurons in primates," *Nature*, vol. 408, no. 16, pp. 361–365, 2000.

[13] D. M. Taylor, S. I. H. Tillery, and A. B. Schwartz, "Direct cortical control of 3d neuroprosthetic devices," *Science*, vol. 296, no. 5574, pp. 1829–1832, June 7, 2002 2002.

[14] S. Musallam, B. D. Corneil, B. Greger, H. Scherberger, and R. A. Andersen, “Cognitive control signals for neural prosthetics,” *Science*, vol. 305, pp. 258–262, July 9, 2004 2004.

[15] J. M. Carmena, M. A. Lebedev, R. E. Crist, J. E. O’Doherty, D. M. Santucci, D. F. Dimitrov, P. G. Patil, C. S. Henriquez, and M. A. L. Nicolelis, “Learning to control a brain-machine interface for reaching and grasping by primates,” *PLoS Biol*, vol. 1, no. 2, p. e42, 2003.

[16] M. Velliste, S. Perel, M. C. Spalding, A. S. Whitford, and A. B. Schwartz, “Cortical control of a prosthetic arm for self-feeding,” *Nature*, vol. 453, no. 7198, pp. 1098–1101, 2008.

[17] L. R. Hochberg, M. D. Serruya, G. M. Friehs, J. A. Mukand, M. Saleh, A. H. Caplan, A. Branner, D. Chen, R. D. Penn, and J. P. Donoghue, “Neuronal ensemble control of prosthetic devices by a human with tetraplegia,” *Nature*, vol. 442, no. 7099, pp. 164–171, 2006.

[18] A. Gunduz, M. C. Ozturk, J. C. Sanchez, and J. C. Principe, “Echo state networks for motor control of human ecog neuroprosthetics,” ser. Proceedings of the 3rd International IEEE EMBS Conference on Neural Engineering, Kohala Coast, HI, United States, 1999, pp. 514–517.

[19] D. Henze, Z. Borhegyi, J. Sciscvari, A. Mamiya, K. Harris, and G. Buzaki, “Intracellular features predicted by extracellular recordings in the hippocampus in vivo,” *The Journal of Neurophysiology*, vol. 84, pp. 390–400, 2000.

[20] V. Polikov, P. Tresco, and W. Reichert, “Response of brain tissue to chronically implanted neural electrodes,” *Journal of Neuroscience Methods*, vol. 148, pp. 1–18, 2005.

[21] R. Vetter, J. Williams, J. Hetke, E. Nunamaker, and D. R. Kipke, “Chronic neural recording using silicon-substrate microelectrode arrays implanted in cerebral cortex,” *IEEE Trans. Biomed. Eng.*, vol. 51, no. 6, pp. 896–904, 2004.

[22] P. J. Rousche and R. A. Normann, “Chronic recording capability of the utah intracortical electrode array in cat sensory cortex,” *Journal of Neuroscience Methods*, vol. 82, no. 1, pp. 1–15, 1998.

[23] J. C. Williams, R. L. Rennaker, and D. R. Kipke, “Long-term neural recording characteristics of wire microelectrode arrays implanted in cerebral cortex,” *Brain Research Protocols*, vol. 4, no. 3, pp. 303–313, 1999, tY - JOUR.

[24] X. D. Liu, D. B. McCreery, L. A. Bullara, and W. F. Agnew, “Evaluation of the stability of intracortical microelectrode arrays,” *Ieee Transactions on Neural Systems and Rehabilitation Engineering*, vol. 14, no. 1, pp. 91–100, 2006.

[25] R. Bashirullah, J. Harris, J. Sanchez, T. Nishida, and P. Jose, “Florida wireless implantable recording electrodes (fwire) for brain machine interfaces,” 2007.

[26] E. Patrick, M. Ordonez, N. Alba, J. C. Sanchez, and T. Nishida, “Design and fabrication of a flexible substrate microelectrode array for brain machine interfaces,” in *Engineering in Medicine and Biology Society, 2006. EMBS ’06. 28th Annual International Conference of the IEEE*, 2006, pp. 2966–2969.

[27] E. Patrick, V. Sankar, W. Rowe, S.-F. Yen, J. C. Sanchez, and T. Nishida, “Flexible polymer substrate and tungsten microelectrode array for an implantable neural recording system,” in *Engineering in Medicine and Biology Society, 2008. EMBS ’08. 30th Annual International Conference of the IEEE*, 2008, pp. 3158–3161.

[28] E. Patrick, V. Sankar, W. Rowe, J. C. Sanchez, and T. Nishida, “Design of an implantable intracortical microelectrode system for brain-machine interfaces,” in *Neural Engineering, 2009. Conference Proceedings. 4th International IEEE EMBS Conference on*, 2009.

[29] E. Patrick, V. Sankar, W. Rowe, J. C. Sanchez, and T. Nishida, “An implantable integrated low-power amplifier-microelectrode array for brain-machine interfaces,” in *Engineering in Medicine and Biology Society, 2010. EMBS ’10. 32nd Annual International Conference of the IEEE*, 2010.

[30] E. Patrick, M. Orazem, J. C. Sanchez, and T. Nishida, “Corrosion of tungsten microelectrodes used in neural recording applications,” *J. of Neuroscience Methods*, to be submitted.

[31] E. Patrick, M. Orazem, T. Nishida, and V. Vivier, “Use of impedance spectroscopy to assess the quality of microelectrode fabrication,” *Journal of the Electrochemical Society*, to be submitted.

[32] T. Trappenberg, *Fundamentals of Computational Neuroscience*. New York, NY: Oxford University Press, 2002.

[33] G. R. Holt and C. Koch, “Electrical interactions via the extracellular potential near cell bodies,” *Journal of Computational Neuroscience*, vol. 6, no. 2, pp. 169–184, 1999.

[34] K. Drake, K. D. Wise, J. Farraye, D. J. Anderson, and S. Bement, “Performance of planar multisite microprobes in recording extracellular single-unit intracortical activity,” *IEEE Trans. Biomed. Eng.*, vol. 35, no. 9, pp. 719–732, 1988.

[35] C. L. Lopreore, T. M. Bartol, J. S. Coggan, D. X. Keller, G. E. Sosinsky, M. H. Ellisman, and T. J. Sejnowski, “Computational modeling of three-dimensional electrodiffusion in biological systems: Application to the node of ranvier,” vol. 95, no. 6, pp. 2624–2635, 2008, 0006-3495.

[36] J. Newman, *Electrochemical Systems*. Hoboken, NJ: John Wiley and Sons, Inc., 2004.

[37] M. Salcman and M. Bak, "Design, fabrication and in-vivo behavior of chronic recording intracortical microelectrodes," *IEEE Trans. Biomed. Eng.*, vol. 20, pp. 253–260, 1973.

[38] M. Salcman and M. Bak, "A new chronic recording intracortical microelectrode," *Med. Biol. Eng.*, vol. January, pp. 42–50, 1976.

[39] "Tucker davis technologies," World Wide Web, http://www.tdt.com/products/MW16.htm, 2008.

[40] "Microprobe, inc." World Wide Web, http://www.microprobes.com/, 2008.

[41] K. Wise and J. Starr, "An integrated-circuit approach to extracellular micro-electrodes," *IEEE Trans. Biomed. Eng.*, vol. 17, pp. 238–247, 1970.

[42] K. Najafi, K. Wise, and T. Mochizuki, "A high-yield ic-compatible multichannel recording array," *IEEE Trans. Electron Devices*, vol. ED-22, pp. 230–241, 1985.

[43] K. Najafi and K. D. Wise, "An implantable multielectrode array with on-chip signal processing," *IEEE Journal of Solid State Circuits*, vol. sc-21, pp. 1035–1044, 1986.

[44] J. Ji and K. D. Wise, "An implantable cmos circuit interface for multiplexed microelectrode recording arrays," *IEEE Journal of Solid State Circuits*, vol. 27, no. 3, pp. 433–443, 1992.

[45] J. Heteke, J. Lund, K. Najafi, K. Wise, and D. Anderson, "Silicon ribbon cables for chronically implantable microelectrode arrays," *IEEE Trans. Biomed. Eng.*, vol. 41, pp. 314–321, 1994.

[46] A. Hoogerwerf and K. Wise, "A three-dimensional microelectrode array for chronic neural recording," *IEEE Trans. Biomed. Eng.*, vol. 41, pp. 1136–1146, 1994.

[47] K. D. Wise, D. J. Anderson, J. F. Hetke, D. R. Kipke, and K. Nijafi, "Wireless implantable microsystems: High density electronic interfaces to the nervous system," *Proceedings of the IEEE*, vol. 92, no. 76-97, 2004.

[48] Y. Yao, M. Gulari, B. Casey, J. A. Wiler, and K. D. Wise, "Silicon microelectrodes with flexible integrated cables for neural implant applications," May 2-5 2007.

[49] K. Wise, A. Sodagar, Y. Yao, M. Gulari, and K. Najafi, "Microelectrodes, microelectronics, and implantable neural microsystems," *Proceedings of the IEEE*, vol. 96, pp. 1184–1202, 2008.

[50] P. K. Campbell, K. E. Jones, R. J. Huber, K. W. Horch, and R. A. Norman, “A silicon-based three- dimensional neural interface: Manufacturing processes for a intracortical electrode array,” *IEEE Trans. Biomed. Eng.*, vol. 38, pp. 758–768, 1991.

[51] D. A. Jones, *Principles and Prevention of Corrosion*. New York, NY: Maxmilliam Publishing Co., 1992.

[52] A. Branner, R. B. Stein, and R. A. Normann, “Selective stimulation and recording using a slanted multielectrode array,” *Annual International Conference of the IEEE Engineering in Medicine and Biology - Proceedings*, vol. 1, p. 377, 1999.

[53] R. Bhandari, S. Negi, L. Rieth, M. Toepper, S. Kim, M. Klein, H. Oppermann, R. A. Normann, and F. Solzbacher, “System integration of the utah electrode array using a biocompatible flip chip under bump metallization scheme,” ser. Proceedings of SPIE - The International Society for Optical Engineering, vol. 6525. San Diego, CA, United States: SPIE, Bellingham WA, WA 98227-0010, United States, 2007, p. 65251.

[54] S. Kim, P. Tathireddy, R. A. Normann, and F. Solzbacher, “Thermal impact of an active 3-d microelectrode array implanted in the brain,” *IEEE Transactions on Neural Systems and Rehabilitation Engineering*, vol. 15, no. 4, pp. 493–501, 2007.

[55] P. Norlin, M. Kindlundh, A. Mouroux, K. Yoshida, and U. G. Hofmann, “A 32-site neural recording probe fabricated by drie of soi substrates,” *Journal of Micromechanics and Microengineering*, vol. 12, no. 4, pp. 414–419, 2002.

[56] M. Kindlundh, P. Norlin, and U. G. Hofmann, “A neural probe process enabling variable electrode configurations,” *Sensors and Actuators B: Chemical*, vol. 102, no. 1, pp. 51–58, 2004.

[57] J. Muthuswamy, M. Okandan, and N. Jackson, “Single neuronal recordings using surface micromachined polysilicon microelectrodes,” *Journal of Neuroscience Methods*, vol. 142, no. 1, pp. 45–54, 2005.

[58] P. Rousche, D. Pellinen, D. Pivin, J. Williams, R. Vetter, and D. Kipke, “Flexible polyimide-based intracortical electrode arrays with bioactive capability,” *IEEE Trans. Biomed. Eng.*, vol. 48, no. 3, pp. 361–371, 2001.

[59] D. O’Brien, T. Nichols, and M. Allen, “Flexible microelectrode arrays with integrated insertion devices,” *IEEE MEMS*, pp. 216–219, 2001.

[60] D. S. Pellinen, T. Moon, R. J. Vetter, R. Miriani, and D. R. Kipke, “Multifunctional flexible parylene-based intracortical microelectrodes,” ser. Annual International Conference of the IEEE Engineering in Medicine and Biology - Proceedings, vol. 7 S, Shanghai, China, 2005, pp. 5272–5275.

[61] J. Seymour and D. Kipke, “Neural probe design for reduced tissue encapsulation in cns,” *Biomaterials*, vol. 28, pp. 3594–3607, 2007.

[62] K. Lee, J. He, R. Clement, S. Massia, and B. Kim, “Biocompatible benzocyclobutene (bcb)-based neural implants with micro-fluidic channel,” *Biosensors and Bioelectronics*, vol. 20, no. 2, pp. 404–407, 2004.

[63] T. Stieglitz and M. Gross, “Flexible biomems with electrode arrangements on front and back side as key component in neural prostheses and biohybrid systems,” *Sensors and Actuators B-Chemical*, vol. 83, no. 1-3, pp. 8–14, 2002.

[64] T. Stieglitz, M. Schuettler, and K. P. Koch, “Implantable biomedical microsystems for neural prostheses,” *IEEE Engineering in Medicine and Biology Magazine*, vol. 24, no. 5, pp. 58–65, 2005.

[65] S. Takeuchi, T. Suzuki, K. Mabuchi, and H. Fujita, “3d flexible multichannel neural probe array,” *Journal of Micromechanics and Microengineering*, vol. 14, pp. 104–107, 2004.

[66] T. Suzuki, D. Ziegler, K. Mabuchi, and S. Takeuchi, “Flexible neural probes with micro-fluidic channels for stable interface with the nervous system,” ser. 26th Annual Internationals Conference of the IEEE EMBS, San Franscico, CA, USA, September 1-5 2004, pp. 4057–4058.

[67] Y. Kato, M. Nishino, I. Saito, T. Suzuki, and K. Mabuchi, “Flexible intracortical neural probe with biodegradable polymer for delivering bioactive components,” ser. Proceedings of 2006 International Conference on Microtechnologies in Medicine and Biology, Okinawa, Japan, 2006, pp. 143–146.

[68] Y. Kato, I. Saito, T. Hoshino, T. Suzuki, and K. Mabuchi, “Preliminary study of multichannel flexible neural probes coated with hybrid biodegradable polymer,” ser. Annual International Conference of the IEEE Engineering in Medicine and Biology - Proceedings, New York, NY, United States, 2006, pp. 660–663.

[69] K. C. Cheung, P. Renaud, H. Tanila, and K. Djupsund, “Flexible polyimide microelectrode array for in vivo recordings and current source density analysis,” *Biosensors and Bioelectronics*, vol. 22, no. 8, pp. 1783–1790, 2007.

[70] G. A. G. D. J. M. J. C. P. W. V. S. D. M. T. P. A. T. Theodore W. Berger (Chair), John K. Chapin, “Wtec panel report on international assessment of research and development in brain-computer interfaces,” WORLD TECHNOLOGY EVALUATION CENTER INC, BALTIMORE MD, Tech. Rep., 2007.

[71] R. Carter and J. Houk, “Multiple single-unit recordings for the cns using thin-film electrode arrays,” *IEEE Trans Rehab Eng*, vol. 1, no. 3, pp. 175–184, 1993.

[72] R. A. Normann, P. K. Campbell, and K. E. Jones, “Silicon based electrode array for intracortical stimulation: Structural and electrical properties,” ser. Proceedings of the Annual Conference on Engineering in Medicine and Biology, vol. 11 pt 3. Seattle, WA, USA: Publ by Alliance for Engineering in Medicine and Biology, Washington, DC, USA, 1989, pp. 939–940.

[73] D. Szarowski, M. Andersen, S. Retterer, A. Spence, M. Isaacson, H. Craighead, J. Turner, and W. Smith, “Brain responses to micro-machined silicon devices,” *Brain Research*, vol. 983, pp. 23–35, 2003.

[74] R. Biran, D. C. Martin, and P. Tresco, “Neuronal cell loss accompanies the brain tissue response to chronically implanted silicon microelectrode arrays,” *Experimental Neurology*, vol. 195, pp. 115–126, 2005.

[75] B. Burke and C. Lewis, *The Macrophage*. Oxford: Oxford Medical Publications, 2002.

[76] J. Turner, W. Shain, D. Szarowski, M. Andersen, S. Martins, M. Isaacson, and H. Craighead, “Cerebral astrocyte response to micromachined silicon implants,” *Experimental Neurology*, vol. 156, pp. 33–49, 1999.

[77] D. Merrill and P. Tresco, “Impedance characterization of microarray recording electrodes in vitro,” *IEEE Tran. Biomed Eng.*, vol. 52, pp. 1960–1965, 2005.

[78] A. Reynolds, C. Laurie, R. Mosley, and H. Gendelman, “Oxidative stress and the pathogenesis of neurodegenerative disorders,” *International Review of Neurobiology*, vol. 82, pp. 297–321, 2007.

[79] R. Biran, D. C. Martin, and P. Tresco, “The brain tissue response to implanted silicon microelectrode arrays is increased when the device is tethered to the skull,” *Journal of Biomedical Materials Research Part A*, vol. 82, no. 1, pp. 169–178, 2007.

[80] Y. Kim, R. Hitchcock, M. Bridge, and P. Tresco, “Chronic response of adult rat brain tissue to implants anchored to the skull,” *Biomaterials*, vol. 25, pp. 2229–2237, 2004.

[81] S. Ranson, *The Anatomy of the Nervous System*. Philadelphia, PA: W. B. Saunder Company, 1945.

[82] H. Lee, R. Bellamkonda, W. Sun, and M. Levenston, “Biomechanical analysis of silicon microelectrode-induced strain in the brain,” *J. Neural Eng*, vol. 2, pp. 81–89, 2005.

[83] J. Subbaroyan, D. Martin, and D. Kipke, “A finite-element model of the mechanical effects of implantable microelectrodes in the cerbral cortex,” *J. Neural Eng*, vol. 2, pp. 103–113, 2005.

[84] M. P. Hughes, K. Bustamante, D. Banks, and D. J. Ewins, “Effects of electrode size on the preformance of neural recording microelectrodes,” in *1st Annual International IEEE-EMBE*, Lyon, France, 2000.

[85] S. F. Lempka, M. D. Johnson, D. W. Barnett, M. A. Moffitt, K. J. Otto, D. R. Kipke, and C. C. McIntyre, “Optimization of microelectrode design for cortical recording based on thermal noise considerations,” in *Engineering in Medicine and Biology Society, 2006. EMBS ’06. 28th Annual International Conference of the IEEE*, 2006, pp. 3361 – 3364.

[86] J. J. Jacobs, J. L. Gilbert, and R. M. Urban, “Current concepts review - corrosion of metal orthopaedic implants,” pp. 268–82, February 1, 1998 1998.

[87] A. Norlin, J. Pan, and C. Leygral, “Investigation of electrochemical behavior for stimulating/sensing materials for pacemaker electrode applications,” *J of the ELectrochemical Society*, vol. 152, no. 2, pp. J7–J15, 2005.

[88] A. Norlin, J. Pan, and C. Leygral, “Investigation of interfacial capacitance of Pt, Ti, and TiN coated electrodes by electrochemical impedance spectroscopy,” *Biomolecular Engineering*, vol. 19, pp. 67–71, 2002.

[89] S. B. Brummer and M. J. Turner, “Electrochemical considerations for safe electrical stimulation of the nervous system with platinum electrodes,” *IEEE Transactions on Biomedical Engineering*, vol. BME-24, no. 1, pp. 59–63, 1977.

[90] D. R. Merrill, M. Bikson, and J. G. R. Jefferys, “Electrical stimulation of excitable tissue: Design of efficacious and safe protocols,” *Journal of Neuroscience Methods*, vol. 141, no. 2, pp. 171–198, 2005, 0165-0270 doi: DOI: 10.1016/j.jneumeth.2004.10.020.

[91] J. Bockris and A. Reddy, *Modern Electrochemistry*. New York, NY: Plenum Press, 1970.

[92] A. Hassibi, R. Navid, R. Dutton, and T. Lee, “Comprehensive study of noise processes in electrode electrolyte interfaces,” *Jornal of Applied Physics*, vol. 15, pp. 1074–1082, 2004.

[93] C. Gabrielli, “Identification of electrochemical processes by frequency response,” Schlumberger Technologies, Tech. Rep. Technical report Number 004/83, 1984.

[94] S. Bothra, H. Sur, and V. Liang, “A new failure mechanism by corrosion of tungsten in a tungsten plug process,” *Microelectronics and Reliability*, vol. 39, no. 1, pp. 59–68, 1999.

[95] M. Peuster, C. Fink, and C. von Schnakenburg, “Biocompatibility of corroding tungsten coils: in vitro assessment of degradation kinetics and cytotoxicity on human cells,” *Biomaterials*, vol. 24, pp. 4057–4061, 2003.

[96] J. Sanchez, N. Alba, T. Nishida, C. Batich, and P. Carney, "Structural modifications in chronic microwire electrodes for cortical neuroprosthetics: A case study," *IEEE Trans. on Neural Syst. Rehab. Eng.*, pp. 217–221, 2006.

[97] R. S. Lillard, G. S. Kanner, and D. P. Butt, "The nature of oxide films on tungsten in acidic and alkaline solutions," *Journal of The Electrochemical Society*, vol. 145, no. 8, pp. 2718–2725, 1998.

[98] M. Anik, "ph-dependent anodic reaction behavior of tungsten in acidic phosphate solutions," *Electrochimica Acta*, vol. 54, no. 15, pp. 3943–3951, 2009.

[99] M. Anik and K. Osseo-Asare, "Effect of ph on the anodic behavior of tungsten," *Journal of The Electrochemical Society*, vol. 149, no. 6, pp. B224–B233, 2002.

[100] J. W. Johnson and C. L. Wu, "The anodic dissolution of tungsten," *Journal of The Electrochemical Society*, vol. 118, no. 12, pp. 1909–1912, 1971.

[101] G. S. Kelsey, "The anodic oxidation of tungsten in aqueous base," *Journal of The Electrochemical Society*, vol. 124, no. 6, pp. 814–819, 1977.

[102] C. de Haro, R. Mas, G. Abadal, J. Munoz, F. Perez-Murano, and C. Dominguez, "Electrochemical platinum coatings for improving performance of implantable microelectrode arrays," *Biomaterials*, vol. 23, no. 23, pp. 4515–4521, 2002.

[103] D. R. Kipke, "Silicon-substrate intracortical microelectrode arrays for long-term recording of neuronal spike activity in cerebral cortex," *IEEE Trans. Rehab. Eng.*, vol. 11, pp. 151–155, 2003.

[104] E. Maynard, C. Nordhausen, and R. A. Normann, "The Utah intracortical electrode array: A recording structure for potential brain-computer interfaces," *Electroencephalography and Clinical Neurophysiology*, vol. 102, pp. 228–239, 1997.

[105] J. Pan, D. Theirry, and C. Leygraf, "Electrochemical impedance spectroscopy study of the passive oxide film on titanium for implant application," *Electrochemica Acta*, vol. 41, pp. 1143–1153, 1996.

[106] C. Fonesca and M. Barbosa, "Corrosion behavior of titanium in biofluids containing h_2o_2 studied by electrochemical impedance spectroscopy," *Corrosion Science*, vol. 43, pp. 547–559, 2001.

[107] S. B. Hall, E. A. Khudaish, and A. L. Hart, "Electrochemical oxidation of hydrogen peroxide at platinum electrodes. part iii: Effect of temperature," *Electrochimica Acta*, vol. 44, no. 14, pp. 2455–2462, 1999.

[108] S. B. Hall, E. A. Khudaish, and A. L. Hart, "Electrochemical oxidation of hydrogen peroxide at platinum electrodes. part i: An adsorption-controlled mechanism," *Electrochimica Acta*, vol. 43, no. 5-6, pp. 579–588, 1998.

[109] S. B. Hall, E. A. Khudaish, and A. L. Hart, “Electrochemical oxidation of hydrogen peroxide at platinum electrodes. part ii: effect of potential,” *Electrochimica Acta*, vol. 43, no. 14-15, pp. 2015–2024, 1998.

[110] S. B. Hall, E. A. Khudaish, and A. L. Hart, “Electrochemical oxidation of hydrogen peroxide at platinum electrodes. part iv: phosphate buffer dependence,” *Electrochimica Acta*, vol. 44, pp. 4573–4582, 1999.

[111] S. Boppart, B. Wheeler, and C. Wallace, “A flexible perforated microelectrode array for extended neural recordings,” *IEEE Trans. Biomed. Eng.*, vol. 39, no. 1, pp. 37–42, 1992.

[112] A. Owens and et al, “Multi-electrode aray for measuring evoked potentials for surface of ferret primary auditory cortex,” *J. Neurosci. Meth.*, vol. 58, pp. 209–220, 1995.

[113] G. E. Loeb, M. J. Bak, and E. M. Schmidt, “Parylene as a chronically stable, reproducible microelectrode insulator,” *IEEE Trans. on Biomed. Eng.*, vol. 24, no. 2, pp. 121–128, 1977.

[114] E. M. Schmidt, M. J. Bak, and J. S. McIntosh, “Long-term chronic recording from cortical neurons,” *Experimental Neurology*, vol. 52, no. 3, pp. 496–506, 1976.

[115] E. M. Schmidt and J. S. McIntosh, “Long-term implants of parylene-c coated microelectrodes,” *Med. Biol. Eng. Comput.*, vol. 26, pp. 96–101, 1988.

[116] L. Geddes and R. Roeder, “Criteria for the selection of materials for implanted electrodes,” *Annals of Biomedical Engineering*, vol. 31, pp. 879–890, 2003.

[117] M. Orazem, “A systematic approach toward error structure identification for impedance spectroscopy,” *J. Electroanalytical Chemistry*, vol. 572, pp. 317–327, 2004.

[118] M. Stecker and T. Patterson, “Electrode impedance in neurophysiologic recordings: 1. theroy and intrinsic contributions to noise,” *Am. J. END Technol.*, vol. 38, pp. 174–198, 1998.

[119] G. Paxinos, *The rat brain in stereotaxic coordinates*. Sydney: Academic Press, 1997.

[120] S. Kim, R. Bhandari, M. Klein, S. Negi, L. Rieth, P. Tathireddy, M. Toepper, H. Oppermann, and F. Solzbacher, “Integrated wireless neural interface based on the Utah electrode array,” *Biomedical Microdevices*, vol. 11, no. 2, pp. 453–466, 2009.

[121] Y. K. Song, D. A. Borton, S. Park, W. R. Patterson, C. W. Bull, F. Laiwalla, J. Mislow, J. D. Simeral, J. P. Donoghue, and A. V. Nurmikko, "Active microelectronic neurosensor arrays for implantable brain communication interfaces," *IEEE Transactions on Neural Systems and Rehabilitation Engineering*, vol. 17, no. 4, pp. 339–345, 2009.

[122] R. Bashirullah, J. Harris, J. Sanchez, T. Nishida, and P. Jose, "Florida wireless implantable recording electrodes (fwire) for brain machine interfaces," in *IEEE International Symposium on Circuits and Systems*, 2007.

[123] A. Sodagar, G. Perlin, Y. Yao, K. Wise, and K. Najafi, "An implantable microsystem for wireless multi-channel cortical recording," in *Transducers 2007*, 2007, pp. 69–72.

[124] J. Harris, J. Principe, J. Sanchez, D. Chen, and C. She, "Pulse-based signal compression for implanted neural recording systems," in *IEEE ISCAS*, 2008, pp. 344–347.

[125] A. Legatt, "Imparment of common mode rejection by mismatched electrode impedances: quantitative analysis," *Am. J. EEG Tech.*, vol. 35, pp. 296–302, 1995.

[126] B. Hirschorn, B. Tribollet, and M. E. Orazem, "On the selection of the perturbation amplitude required to avoid nonlinear effects in impedance measurements," *Israel Journal of Chemistry*, vol. 48, pp. 133–142, 2008.

[127] R. Meyer, S. Cogan, T.Nguyen, and R. Rauh, "Electrodeposited iridium oxide for neural stimulation and recording electrodes," *IEEE Trans. Neural Syst. Rehab. Eng.*, vol. 9, no. 1, pp. 2–10, 2001.

[128] J. Yang and D. C. Martin, "Microporous conduction polymers on neural microelectrode arrays ii. physical characterization," *Sensors and Actuators A*, vol. 113, pp. 204–211, 2004.

[129] X. Cui and D. C. Martin, "Electrochemical deposition and characterization of ploy(3,4-ethylenedioxythiophene) on neural microelectrode arrays," *Sensors and Actuators B*, vol. 89, pp. 92–102, 2003.

[130] M. Ates and A. S. Sarac, "Electrochemical impedance spectroscopy of poly[carbazole-co-n-p-tolylsulfonyl pyrrole] on carbon fiber microelectrodes, equivalent circuits for modelling," *Progress in Organic Coatings*, vol. 65, pp. 281–287, 2009.

[131] D. T. Price, A. R. A. Rahman, and S. Bhansali, "Design rule for optimization of microelectrodes used in electric cell-substrate impedance sensing (ecis)," *Biosensors and Bioelectronics*, vol. 24, pp. 2071–2076, 2009.

[132] Y. Zhang, H. Wang, J. Nie, Y. Zhang, G. Shen, and R. Yu, “Individually addressable microelectrode arrays fabricated with gold-coated pencil graphite for multiplexed and high sensitive impedance immunoassays,” *Biosensors and Bioelectronics*, vol. 25, pp. 34–40, 2009.

[133] M. E. Orazem, N. Pébère, and B. Tribollet, “Enhanced graphical representation of electrochemical impedance data,” *J. Electrochem. Soc.*, vol. 153, pp. B129–B136, 2006.

[134] G. Brug, A. V. den Eeden, M. Sluyters-Rehbach, and J. Sluyters, “The analysis of electrode impedances complicated by the presence of a constant phase element,” *Electroanal. Chem.*, vol. 176, pp. 275–295, 1984.

[135] M. Orazem, “A systematic approach toward error structure identification for impedance spectroscopy,,” *J. Electroanalytical Chemistry*, vol. 572, pp. 318–327, 2004.

[136] S. Carson, M. Orazem, O. Crisalle, and L. Garcia-Rubio, “On the error structure of impedance measurements,” *Jornal of Electrochemistry Society*, vol. 150, no. 10, pp. 477–490, 2003.

[137] R. Jurczakowski, C. Hitz, and A. Lasia, “Impedance of porous au based electrodes,” *Journal of Electroanalytical Chemistry*, vol. 572, no. 2, pp. 355–366, 2004.

[138] R. Jurczakowski, C. Hitz, and A. Lasia, “Impedance of porous gold electrodes in the presence of electroactive species,” *Journal of Electroanalytical Chemistry*, vol. 582, no. 1-2, pp. 85–96, 2005.

[139] H.-K. Song, Y.-H. Jung, K.-H. Lee, and L. H. Dao, “Electrochemical impedance spectroscopy of porous electrodes: the effect of pore size distribution,” *Electrochimica Acta*, vol. 44, no. 20, pp. 3513–3519, 1999.

[140] R. J. Forster, “Microelectrodes: New dimensions in electrochemistry,” *Chemical Society Reviews*, vol. 23, pp. 289–297, 1994.

[141] M. Fleischmann and S. Pons, “The behavior of microelectrodes,” *Analytical Chemistry*, vol. 59, no. 24, pp. 1391A–1399A, 1987, doi: 10.1021/ac00151a001 0003-2700 doi: 10.1021/ac00151a001.

[142] A. G. Ewing, M. A. Dayton, and R. M. Wightman, “Pulse voltammetry with microvoltammetric electrodes,” *Analytical Chemistry*, vol. 53, no. 12, pp. 1842–1847, 1981, compilation and indexing terms, Copyright 2009 Elsevier Inc. 1982020006804 00032700 MICROVOLTAMMETRIC ELECTRODES.

[143] K. P. Troyer, M. L. A. V. Heien, B. J. Venton, and R. M. Wightman, “Neurochemistry and electroanalytical probes,” *Current Opinion in Chemical Biology*, vol. 6, no. 5, pp. 696–703, 2002, 1367-5931 doi: DOI: 10.1016/S1367-5931(02)00374-5.

[144] W. Pernkopf, M. Sagl, G. Fafilek, J. O. Besenhard, H. Kronberger, and G. E. Nauer, "Applications of microelectrodes in impedance spectroscopy," *Solid State Ionics*, vol. 176, no. 25-28, pp. 2031–2036, 2005.

[145] C. Gabrielli, S. Joiret, M. Keddam, N. Portail, P. Rousseau, and V. Vivier, "Single pit on iron generated by SECM: An electrochemical impedance spectroscopy investigation," *Electrochimica Acta*, vol. 53, no. 25, pp. 7539–7548, 2008, 0013-4686 doi: DOI: 10.1016/j.electacta.2008.01.013.

[146] D. Rolison, "Fabrication of ultramicroelectrodes," in *Ultramicroelectrodes*, M. Fleischmann, S. Pons, D. Rolison, and P. Schmidt, Eds. Datatech Systems, Inc. (Edt.), Scientific Publishing Division, 1987, ch. 3, pp. 65–106.

[147] W. Thormann and A. M. Bond, "Application of transient electrochemical techniques to inlaid ultra-microelectrodes: Assessment of fabrication quality," *Journal of Electroanalytical Chemistry*, vol. 218, no. 1-2, pp. 187 – 196, 1987.

[148] O. Koster, W. Schuhmann, H. Vogt, and W. Mokwa, "Quality control of ultra-microelectrode arrays using cyclic voltammetry, electrochemical impedance spectroscopy and scanning electrochemical microscopy," *Sensors and Actuators, B: Chemical*, vol. 76, pp. 573–581, 2001.

[149] V. M.-W. Huang, V. Vivier, M. E. Orazem, P. Nadine, and B. Tribollet, "The apparent CPE behavior of an ideally polarized disk electrode: A global and local impedance analysis," *J. Electrochem. Soc.*, vol. 154, pp. C81–C88, 2007.

[150] V. M.-W. Huang, V. Vivier, I. Frateur, M. E. Orazem, and B. Tribollet, "The global and local impedance response of a blocking disk electrode with local CPE behavior," *J. Electrochem. Soc.*, vol. 154, pp. C89–C98, 2007.

[151] V. M.-W. Huang, V. Vivier, M. E. Orazem, P. Nadine, and B. Tribollet, "The apparent CPE behavior of a disk electrode with faradaic reactions," *J. Electrochem. Soc.*, vol. 154, pp. C99–C107, 2007.

[152] M. E. Orazem, "A systematic approach toward error structure identification for impedance spectroscopy," *J. Electroanal. Chem.*, vol. 572, pp. 317–327, 2004.

[153] G. J. Brug, A. L. G. van den Eeden, M. Sluyters-Rehbach, and J. H. Sluyters, "The analysis of electrode impedances complicated by the presence of a constant phase element," *J. Electroanal. Chem.*, vol. 176, pp. 275–295, 1984.

[154] M. E. Orazem and B. Tribollet, *Electrochemical Impedance Spectroscopy*. Hoboken, NJ: John Wiley & Sons, 2008.

[155] M. Pourbaix, *Atlas of electrochemical equilibria*. Oxford: Pergamon Press Ltd., 1966.

[156] S. B. Brummer and M. J. Turner, “Electrochemical considerations for safe electrical stimulation of the nervous system with platinum electrodes,” *IEEE Transactions on Biomedical Engineering*, vol. BME-24, no. 1, pp. 59–63, 1977.

[157] B. Ren, X. Xu, X. Q. Li, W. B. Cai, and Z. Q. Tian, “Extending surface raman spectroscopic studies to transition metals for practical applications: Ii. hydrogen adsorption at platinum electrodes,” *Surface Science*, vol. 427-428, pp. 157–161, 1999.

[158] H. D. Yoo, J. H. Jang, B. H. Ka, C. K. Rhee, and S. M. Oh, “Impedance analysis for hydrogen adsorption pseudocapacitance and electrochemically active surface area of pt electrode,” *Langmuir*, vol. 25, no. 19, pp. 11 947–11 954, 2009.

[159] A. Maas, W. Fleckenstein, D. de Jong, and H. van Santbrink, “Monitoring cerebral oxygenation: experimental studies and preliminary clinical results of continuous monitoring of cerebrospinal fluid and brain tissue oxygen tension,” *Acta Neurochir Suppl (Wien)*, vol. 59, p. 5057, 1993.

[160] A. Sarrafzadeh, K. Kiening, T. Bardt, G. Schneider, A. Unterberg, and W. Lanksch, “Cerebral oxygenation in contusioned vs nonlesioned brain tissue: monitoring of ptio2 with licox and paratrend,” *Acta Neurochir Suppl (Wien)*, vol. 71, pp. 186–189, 1998.

[161] F. Beer and E. Johnston, *Mechanics of Materials*. New York: McGraw Hill, 1981.

[162] C. Tian and J. He, “Monitoring insertion force and electrode impedance during implantation of microwire electrodes,” in *IEEE Engineering in Medicine and Biology 27th Annual Conference*, Shanghai, China, 2005.

[163] W. Jensen, U. Hofmann, and K. Yoshida, “Assessment of subdural insertion force of single-tine microelectrodes in rat cerebral cortex,” in *25th Annual International Conference of the IEEE Engineering in Medicine and Biology Society*, Cancun, Mexico, 2003.

BIOGRAPHICAL SKETCH

Erin Elizabeth Patrick was born in Elkins, West Virginia. She graduated from Vero Beach High School in Vero Beach, Florida in the spring of 1997 and started her bachelor's degree at the University of Florida that next fall. In December of 2002 she earned a Bachelor of Science in Electrical Engineering with high honors. During Erin's undergraduate studies she did an internship at Dominion Semiconductor, a DRAM and Flash memory manufacturing facility in Manassas, Virginia, and started working as an undergraduate research assistant for her current advisor in the Interdisciplinary Microsystems Group (IMG) at UF. She then joined IMG as a doctoral candidate in August of 2003. Erin earned a Doctor of Philosophy in Electrical Engineering at UF in August of 2010. Her technical expertise is in microelectromechanical system (MEMS) processing techniques and electrochemical impedance spectroscopy. Her research interests include biological and chemical MEMS sensors.